**Tactile Sensing of Shape: Biomechanics of Contact investigated
using Imaging and Modeling**

by

Wan-Chen Wu

B.S., Mechanical Engineering
National Taiwan University, Taipei, Taiwan, 1996

M.S., Mechanical Engineering
Massachusetts Institute of Technology, 1999

Submitted to the Department of Mechanical Engineering
in Partial Fulfillment of the Requirements for the Degree of

Doctor of Philosophy in Mechanical Engineering

at the

Massachusetts Institute of Technology
February 2006

Signature of Author...
Department of Mechanical Engineering
September 22, 2005

Certified by..
Dr. Mandayam A. Srinivasan
Senior Research Scientist, Department of Mechanical Engineering
Thesis Supervisor

Accepted by...
Prof. Lallit Anand
Chairman, Committee on Graduate Students
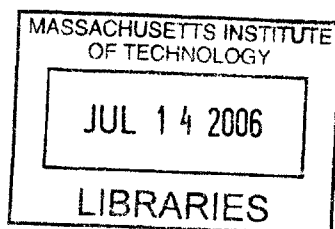
Tactile Sensing of Shape: Biomechanics of Contact investigated
using Imaging and Modeling
by
Wan-Chen Wu
submitted to the Department of Mechanical Engineering
on September 22, 2005, in Partial Fulfillment of the
requirements for the Degree of
Doctor of Philosophy in Mechanical Engineering

Abstract

The overall goal of this research effort is to improve the understanding of the biomechanics of skin as it pertains to human tactile sense. During touch, mechanoreceptors beneath the skin surface are mechanically loaded due to physical contact of the skin with an object and respond with a series of neural impulses. This neural population response is decoded by the central nervous system to result in tactile perception of properties such as the shape, surface texture and softness of the object. The particular approach taken in this research is to develop a realistic model of the human fingertip based on empirical measurements of *in vivo* geometric and material properties of skin layers, so that the mechanical response of the fingertip skin to different shapes of objects in contact can be investigated, to help identify the relevant mechanism that triggers the mechanoreceptors in tactile encoding of object shape.

To obtain geometric data on the ridged skin surface and the layers underneath together with their deformation patterns, optical coherence tomography (OCT) was used to image human fingertips *in vivo,* free of load as well as when loaded with rigid indenters of different shapes. The images of undeformed and deformed finger pads were obtained, processed, and used for biomechanically validating the fingertip model. To obtain material properties of skin layers, axial strain imaging using high frequency ultrasound backscatter microscopy (UBM) was utilized in experiments on human fingertips *in vivo* to estimate the ratio of stiffnesses of the epidermis and dermis.

By utilizing the data from OCT and UBM experiments, a multilayered three dimensional finite element model of the human fingertip composed of the ridged fingerpad skin surface as well as the papillary interface between the epidermis and dermis was developed. The model was used to simulate static indentation of the fingertip by rigid objects of different shapes and to compute stress and strain measures, such as strain energy density (SED), and maximum compressive or tensile strain (MCS, MTS), which have been previously proposed as the relevant stimuli that trigger mechanoreceptor response. The results showed that the intricate geometry of skin layers and inhomogeneous material properties around the locations of the SA-I and RA mechanoreceptors caused significant differences in the spatial distribution of candidate relevant stimuli, compared with other locations at the same depths or the predictions from previous homogeneous models of the fingertip. The distribution of the SED at the locations of SA-I mechanoreceptors and the distribution of MCS/MTS at the locations of RA mechanoreceptors under indentation of different object shapes were obtained to serve as predictions to be tested in future biomechanical and neurophysiological experiments.

Thesis committee: Dr. Mandayam A. Srinivasan (advisor)
Prof. Ioannis V. Yannas
Prof. James DiCarlo

Acknowledgements

I would like to

Thank my advisor Dr. Mandayam Srinivasan's instruction and support for the past years;

Thank NINDS for funding the research;

Thank Prof. Johannes de Boer and Dr. Mark Pierce at MGH for introducing me to OCT field;

Thank Prof. Ioannis Yannas and Prof. James DiCarlo for valuable suggestion on my research;

Thank Dr. Balasundar Raju, Dr. David Schloerb, Dr. Gang Liu, Dr. S. James Biggs, Dr. Lihua Zhou, Dr. Suiren Wan, and Dr. Xiaohan Sun for experience sharing and encouragement;

Thank Mr. Seth Hall for helping me a lot with computer problems;

Thank my family for their love and support;

Thank Chen-Wei Wu;

And most importantly, thank God for everything.

Contents

List of Figures

7

9

List of Tables

Chapter 1
Introduction

1.1 Overview

The tactual sensory information from the hand in contact with an object can be divided into two classes: tactile information and kinesthetic information. The former is derived from the sensors embedded in the skin within and around the contact region, while the latter refers to the sense of position and motion of limbs along with associated forces conveyed by sensory receptors in the skin around the joints, the joint capsules, the tendons, and the muscles, together with the neural signals derived from the motor commands (Srinivasan, 1994). Information from several mechano-sensitive receptors in the skin, the muscle spindles and the joints, can be used by the central nervous system (CNS) to detect the contact with an object as well as the geometrical and material properties of the object. Although the mechano-sensitive receptors are present in every region of the skin, the fingertips have the highest innervation density. The glabrous and readily deformable palmar side of the fingertips aids in both exploration and grasping of the objects.

Humans can detect and discriminate a wide range of physical features of objects using their tactile sensing system. Even though the details of the functioning of this system remain largely unknown at the present time, the sequence of events resulting in human tactile sense can be divided into four: First, the object contacts the skin and this leads to a distribution of forces on the skin surface. Second, these surface force distributions lead to sub-surface distributions of mechanical stresses and strains, depending on the mechanical filtering properties of the skin. Third, these stresses and strains are transduced into neural impulses by the mechanorecptors in the skin. Finally, these neural impulses reach the brain where the object is perceived. The primary neural event in the human tactile recognition of objects is the transduction of the mechanical signals imposed on the skin into trains of nerve impulses by the mechanorecepters embedded in the skin. Philips and Johnson hypothesized that certain relevant stimuli (i.e. different combinations of stress/strain) trigger particular responses in mechanoreceptors (Philips and Johnson, 1981). To gain insight into neural coding of tactile information, the biomechanical behavior of the fingertip tissues needs to be studied.

A deeper understanding of the human tactile system is essential to the design and development of artificial tactile sensing systems and human-machine haptic interfaces used in teleoperation and virtual environments (Srinivasan, 1994).

1.2 Motivation

Mechanistic basis of the geometry and material property of the fingertip and its constituents needs to be studied to understand its relevance to the exquisite functioning of the human tactile system. As the finger comes into contact with an object, skin deformation occurs and a contact pressure distribution presents itself on the skin surface. This pressure profile filters through the skin and places stresses and strains upon the mechanoreceptors. Because no current experimental techniques can measure the stress and strain field under the skin during touch, a mechanistic model of the finger must be created in order to reliably predict the mechanical behavior. The calculation of stresses and strains within the skin requires knowledge of the spatial distribution of tissues that make up the skin, along with their mechanical properties. Very few methods for the direct measurement of *in vivo* tissue properties exist. One approach to examine the biomechanical behavior and to determine the mechanical properties is to measure the deflection of tissues under different loads. This measurement can be achieved through imaging of the internal tissues in the fingertip at resolutions sufficient to reveal the underlying structures. Such information can then be used to develop a mechanistic model to compute the stresses and strains in the fingertip during tactile sensing and the stress and strain state at typical receptor locations can then be calculated under various mechanical stimuli. A model proposed by Philips and Johnson (1981b) to calculate the stress and strain values at typical receptor sites within the skin is mechanically equivalent to a homogeneous, isotropic, incompressible and linearly elastic half-space in a state of plane stress or strain with infinitesimal deformations. Using this model, maximum compressive strain profiles calculated were in good agreement with the recorded SAI response under a range of periodic and aperiodic gratings. In Srinivasan's study (1989), a "waterbed" model was developed for the primate fingerpad skin in which the incompressible fluid is enclosed in a membrane which is assumed to have negligible thickness. The model can accurately predict the skin surface deflection measured *in vivo* under line loads. The mechanistic behavior of the fingertip can be computed using a model that mimics the exterior and interior geometry of the finger pad tissue layers, the material properties of each of the constituents of the

finger pad, and boundary conditions used in the experiments. One way to develop a mechanical model is to use the finite element method, which can calculate the stress and strain state at all points in the fingertip for any set of mechanical stimuli imposed on the fingertip. The finite element method offers the required flexibility and accuracy in modeling the geometry and material properties of the constituents, and simulating the response to real life stimuli necessary for realistic modeling of the finger pad. Previous research on finite element models of the finger pad has proven the finite element method to be a useful tool in investigating the mechanics of touch with its encouraging results (Dandekar and Srinivasan, 1996; Raju and Srinivasan, 1998; Cysyk and Srinivasan, 1999). Dandekar and Srinivasan constructed 3D models of primate finger pads for finite element analysis and also measured surface deformation of the human fingertip *in vivo* by indenting it with various sizes and shapes (Dandekar and Srinivasan, 1995). They used a videomicroscopy system to obtain the external geometry information and to determine surface deformation under loads (Dandekar et al., 1995). Approximate internal geometry information was used to construct the interior of the models. These continuum-mechanics mathematical models were implemented based on the theory of elasticity. They found that strain energy density at the receptor location is directly related to the static discharge rate of the slowly adapting afferents. Additionally, they showed that the model geometry significantly influences the performance of the model. It would be helpful if a model can be developed that further improved the existing ones, with finer mesh to take care of the fine structures, which was not considered previously, so that the location of the mechanoreceptors can be specified more precisely and the distribution of material properties can be closer to more realistic values. Imaging could provide details of the structures and layers in the skin, which can then be used to develop the finite element models.

For skin surface imaging, videomicroscopy has been used (Srinivasan, 1989; Dandekar and Srinivasan, 1995). Non-invasive imaging of skin has several applications in dermatology. These include determination of tumor margins prior to surgery, tumor staging, evaluation of non-tumorous skin lesions, determination of the depth of thermal burn injuries, studying the effects of photoaging, studying the effects of nuclear radiation on skin, and evaluation of the effects of cosmetics on skin. Imaging the internal structures of the finger pad would help to refine its model by incorporating internal tissue geometry. Voss and Srinivasan (1997) used MRI to image the full cross section of the deformed and undeformed human fingertip *in vivo* and could

generally differentiate the epidermis, the dermis, the subcutaneous layer, and the bone within it. These structural and biomechanical information were included in Cysyk and Srinivasan's 2D model (1999). To further look into the ridged top surface and the papillary structure around the RA and SA-I mechanoreceptors within the fingerpad, an imaging modality with even higher resolution should be used. Raju and Srinivasan used ultrasonic backscatter microscopy (UBM) to investigate the human skin both for geometry and material properties (1999, 2002). Using a transducer with central frequency of 44 MHz, their equipment displayed a resolution as high as 15 μm axially and 68 μm laterally. Optical coherence tomography (OCT), an imaging technique which can exhibit a resolution up to several microns in skin imaging, could be a candidate to fulfill this goal. By comparing the images taken before and after the application of a known load to the finger, the displacements of the skin tissues and consequently the internal strain distribution could be obtained. Ultrasound elastography has been first introduced in 1991 (Ophir et al.) and developed for the past years. For one method, RF signals were taken before and after tiny axial compression, then cross-correlation was calculated on pairs of A-lines to find the time delay at which the cross correlation function reaches the maximum, thus the displacement and strain, the differential of displacement, of tissue structure were found. These mechanical strains then could be related to the stiffness distribution in the skin.

The model created should be able to simulate the biomechanical experiments done and needs to be validated by the empirical results. It could be used to numerically compute the stress and strain fields near the nerve endings due to prescribed mechanical loads on the skin surface, thus obviating the need for extensive experiments.

1.2.1 Problem

Figure 1.1 shows the sequence of events in the process of tactile sensing. As described previously, during the process of contact of the fingertip skin with the environment, loads are imposed on the skin causing it to deform. They define a unique state of stress and strain inside the fingertip skin. The receptors encode information both spatially and temporarily from the stress and strain fields created by the stimulus on the skin surface. The interesting aspect of this phenomenon intended to be investigated in this thesis is how the stress and/or strain distribution within the fingertip tissue can be affected by the shapes of the objects in contact, so that the mechanoreceptors encode the neural signals differently for the CNS to decode them.

The challenge lies in the fact that at present, non-invasive research methods limit what can be studied on *in vivo* subjects. One step towards examining these is to build and test mechanical models of the finger pad for stress and strain fields. Mechanistic models have the advantage of testing hypothesized relevant mechanism for each specific class of receptors and provide a method to predict the results of biomechanical experiments. The idealized model needs to be as realistic as possible, which in turn, requires data on geometry and mechanical behavior of soft tissues beneath the skin.
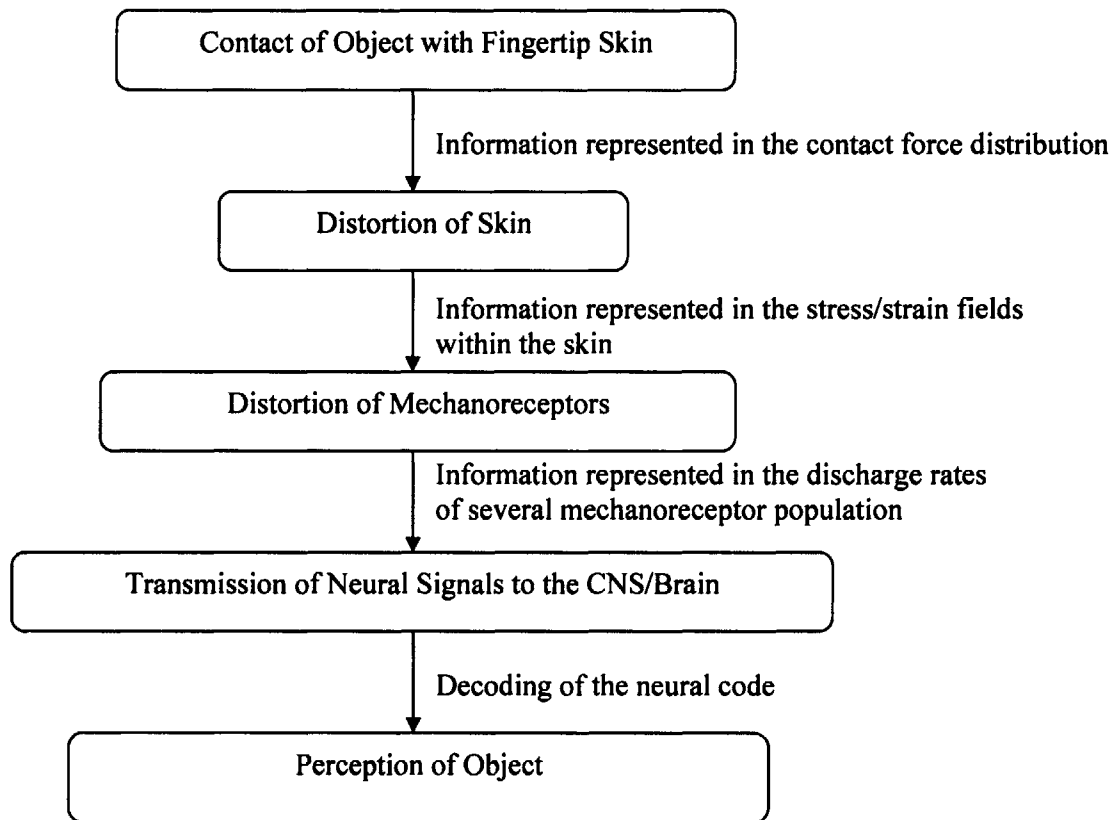
Figure 1-1. The series of events in the process of tactile sensing.

1.2.2 Approach

To investigate the mechanics of touch, models of the skin and subcutaneous tissues are needed partly due to the lack of experimental techniques to measure the stress and strain field under the skin during touch. The fingertip geometry and material properties would be modeled using the finite element method. The 3D finite element model previously developed in the MIT Touch Lab

16

(Raju and Srinivasan, 1999; Zhou and Srinivasan, 2002) would be used as the basis for the development of the new model. In order to refine the model, the geometrical and material properties, and the biomechanical behavior of the human fingertip have to be obtained from *in vivo* experiments. The refinement of the geometry of the fingertip model would be based on high resolution imaging of the human finger, while the material properties of the epidermis and the dermis would be determined using strain imaging techniques. In order to model the contact between sharp curvatures such as the edges of bars and the finger pad, the finite element model would be refined to decrease the minimum spacing between the nodes to 0.1 mm, five times the spatial reduction of Dandekar and Srinivasan's model (1997). The loads (or displacement) specified over the surface of the skin, which can be controlled, are the mechanical stimulation to the skin. The boundary conditions would be specified, the formulated equations would be solved using a computer based iterative algorithm, and the resulting mechanical state of the finger evaluated. A commercial finite element software ABAQUS (HKS Inc., Pawtucket, RI) would be used in all the simulations. The mechanistic problem of contact between the stimulus shape and the finger pad is nonlinear because the contact region is governed by the deformation of the fingertip, which depends on the pressure distribution that, in turn, depends on the unknown extent of the contact region. This problem needs to be solved iteratively with small increments in indentation until the prescribed force or depth of indentation was reached by the rigid stimulus shapes.

For biomechanical behavior, the human fingertip would be indented with various shapes and the surface deformation of the human fingertip under indentation would be monitored *in vivo* using high resolution imaging technology. With the given set of mechanical stimuli, the surface deformation of the fingertip could be measured. Image processing techniques would be used to enhance the images, capture the tissue boundaries, and locate the structures of interest. By varying the indentation depths or the total load applied to the fingertip, the static tissue behavior during loading would be examined by recording the evolution of the top surface profile. The surface deformation predicted by the finite element models can be compared with the experimentally observed data to verify performance of the computational model. Agreement in the experimental and predicted deformations will be used as the biomechanical check of the model.

Once confidence in the model is attained, simulations can be performed for a wide of variety of input conditions to predict the surface deformation. Complex contact mechanics between the finger and a rigid object can be evaluated. With the use of the finite element model of the finger, the OCT experiments can be simulated using the same prescribed conditions and the mechanics of touch can be studied and understood. The relation between the shapes of the objects in contact and the stress and strain distribution within the skin tissue would be investigated. Figure 1-2 shows the general approach described.
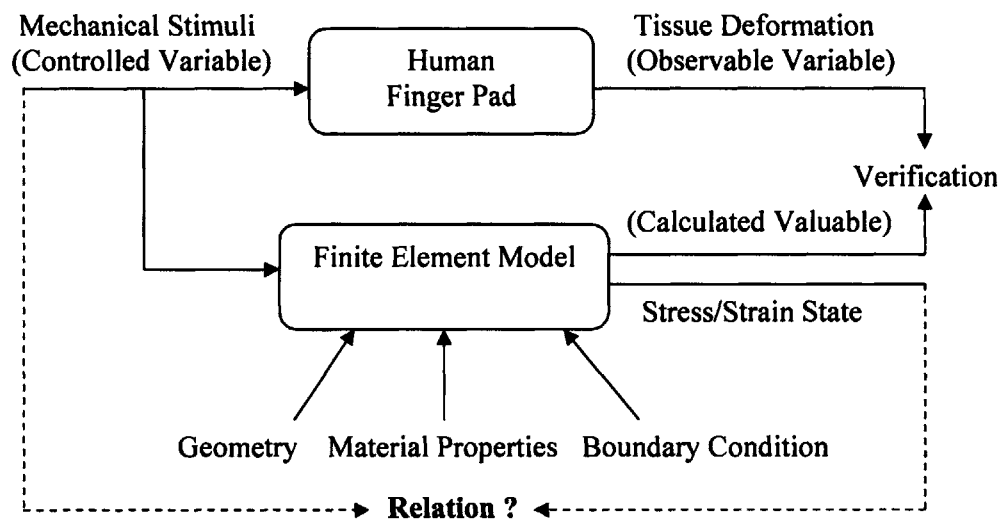
Figure 1-2. The general approach to developing and simulating a fingertip finite element model.

1.3 Thesis Overview

This thesis focuses on understanding the biomechanics of touch. It is to investigate the functioning of the tactile sensing of the finger pad in contact with different shapes of objects through simulation of a three dimensional finite element fingertip model built based on the general exterior geometry of human finger, UBM strain imaging data and OCT imaging results. Various biomechanical experiments are simulated using this model.

Chapter 2 provides background information necessary in the study of human tactile sense, the anatomy of the human finger, the role of different mechanoreceptor types, and imaging techniques, and summarizes previous work on the human fingertip, OCT, UBM, primate fingertip models, and human tactile sensing.

18

In Chapter 3, the experimental methods and procedures used to obtain OCT images of the finger pad with and without static loads will be discussed. The experimental setup, the protocols of the experiments, the image processing methods used, and the experimental results are presented.

Chapter 4 describes the UBM experiments on human subjects to get the stiffness information of the human finger pad. The experimental setup, the protocol of the experiments, the data analysis, and the experimental results are presented.

Based on the empirical data, a 3D high mesh density finite element model was built and validated, as described in Chapter 5.

Further discussion on the simulation of the model is in Chapter 6. The relationship between the strain and stress distribution and the geometry of the contacted object and the possible implication to tactile neural coding is described.

Chapter 7 summarizes the work and its significance, and discusses future research directions.

Chapter 2
Background

2.1 The Anatomy of Human Fingertip

The human skin, consisting of an approximate area of 1.5-2 m^2 in adults, is sensitive to touch at all locations in varying degrees of sensitivity and spatial acuity. Several types of mechanoreceptors embedded in the skin, joints, the muscle spindles, and tendons convey haptic information to the central nervous system. But fingertip is the primary tool for tactile sensing and information gathering about the shape, size, and texture of objects because the fingertip has specialized features in terms of geometry, mechanical constitution and highest density of nerve fibers that detect and encode properties of objects indenting in contact with the skin surface.

The structure of the human fingertip is quite complex and the major structural components that make up the fingertip are the skin, subcutaneous tissues mostly composed of fat, the bone, and the nail. A rigid bone through the center of the finger provides the structural support required for effective manipulation and exploration tasks, while the surrounding skin is deformable to allow for shapes and textures to present a spatiotemporal force profile on the skin surface. Typical human fingertips are about 10 to 20 mm in diameter and the length of the distal phalanx varies between 20 to 30 mm. The skin on the palmar side is glabrous, thicker than that of other parts of the body, and is characterized by epidermal ridges, which reflect the underlying papillary ridges. These dermal striations make up the fingerprints on the human fingers, which can act as levers to assist in the detection of movement and vibrational cues. The spacing between the ridges is about 500 µm.

2.1.1 The Skin

The fingertip skin can be divided into two major layers: the epidermis and dermis. The epidermis is the superficial stratified epithelium derived from the ectoderm and further sub-divided into five layers, named from skin surface inwards are the stratum corneum, the stratum lucidum, the stratum granulosum, the malphigian layer, and the stratum basale. It has been found that the epidermis thickness is about 0.5-0.9 mm (Lockhart et al., 1965; Lanier et al.1990, Voss and Srinivasan 1997). The mechanical and barrier functions of the epidermis are primarily due to the horny stratum corneum, the outermost layer, made up of dead keratinocytes with no detectable

20

intercellular spaces. The stratum lucidum contains cells that have apparently lost their nuclei and cell boundaries. It is typically only present in the palmar or plantar skin and is about two or three cells thick. The stratum granulosum is also about two to three cells thick, containing granules produced in chemical changes occurring within the cells as they progress to the horny keratin surface layer. The malphigian layer is a site of cellular multiplication, which plays a vital role in skin regeneration. This layer consists of a thick, multicellular layer of polygonal cells, which get flatter as they approach the surface. The stratum basale is attached by means of protoplasmic prolongations (known as hemidesmosomes) to the basement membrane, a fine cellular structure connected to the dermis by collagen or retinacular fibrils. Epidermis is comparatively stronger than the dermis in spite of its smaller thickness. The dermis is a deep vascular connective tissue layer largely mesodermal in origin (O'Rahilly, 1969; Lockhart et al., 1965) and can be divided into the outer papillary layer, which is a close knit network of fibrous and elastic tissue connected to the epidermis by numerous papillae, and the deeper network of reticular layer which contains thicker collagen fibers than the papillary layer and has numerous elastin fibers that run mostly parallel to the skin's surface. The dermis is made up of networks of collagen fibers, elastin fibers, blood vessels, nerves, and lymphatics embedded in a gelatinous matrix called the ground substance (Lanir, 1987, Gibson and Kenedi, 1968).

2.1.2 Mechanoreceptors

The human skin is innervated over the entire region by a variety of peripheral afferent nerve fibers. The receptors at the end of the afferents can be classified generally into mechanoreceptors, thermal receptors, and nociceptors (pain receptors). Among the mechanoreceptors, which are responsible for tactile sensing, there are also differences in their type, their location in the skin, and the innervation density of the receptors depending upon the part of the body under consideration. The mechanoreceptive fibers innervating the primate fingerpad have been categorized based on the adaptive properties of the fiber in responding to stepwise indentation of the most sensitive part of the fiber's receptive field (Darian-Smith, 1984; Valbo and Johansson, 1984). The most important four mechanoreceptors (Figure 2-1) and their features are listed below:

Meissner's corpuscles: They are located in the dermal papillae protruding upwards into the epidermis and are closest to the surface (depth ~ 0.5-0.7 mm) of the skin among all the

mechanoreceptors. The axial dimensions of these encapsulated ellipsoidal corpuscles are of the order o f 100 × 50 μm and the long axis is perpendicular to the skin surface. The afferent fiber associated with these corpuscles has an irregular discoidal form orientated at right angles to the long axis, and is of the rapidly adapting (RA) type, which is sensitive to skin velocity.

Merkel Discs: One of the most important un-encapsulated epidermal nerve ending in primate glabrous skin is the specialized receptor cell, the Merkel cell and the associated disk like nerve terminal. The cell is usually oval or rounded and is located at depth 0.7-1.0 mm in the basal layer cells of the epithelial glandular ridges in groups of 5-10. The diameter of the Merkel cells is of the order of 10 μm. The afferent fiber associated with the Merkel cells is identified as the slowly adapting fiber of type I (SA-I), which is sensitive to both skin displacement and velocity.

Ruffini Corpuscles: Appearing as 4-5 layers of lamellar cells covered by a membrane, they are found at depth 0.8-1.5 mm in the sub-papillary dermis and are relatively large encapsulated structures from 0.5-1.0 mm long, up to 0.2 mm in diameter in their central zone and about 30-40 μm in diameter near the poles. Their long axis typically runs parallel to the skin surface. The afferent fiber associated with these corpuscles is the slowly adapting type II (SA-II), which is sensitive to both skin displacement and velocity.

Pacinian Corpuscles: They are, historically, the earliest known mechanoreceptors. They are ovoid in shape, encapsulated, and are also the largest in size amongst the mechanoreceptors. The long axis of the digital corpuscles varies from 0.3-1.5 mm and the diameter from 0.2-0.7 mm. The corpuscle consists of a central nerve fiber, a compact inner core and several layers of concentrically packed lamellar cells, with fluid filled in the subcapsular space. These are found at depth 1.5-2.0 mm in deeper layers of the dermis or in the subcutaneous fat. Pacinian fibers have low innervation density but are distinctive because of their exquisite sensitivity to vibratory stimuli.
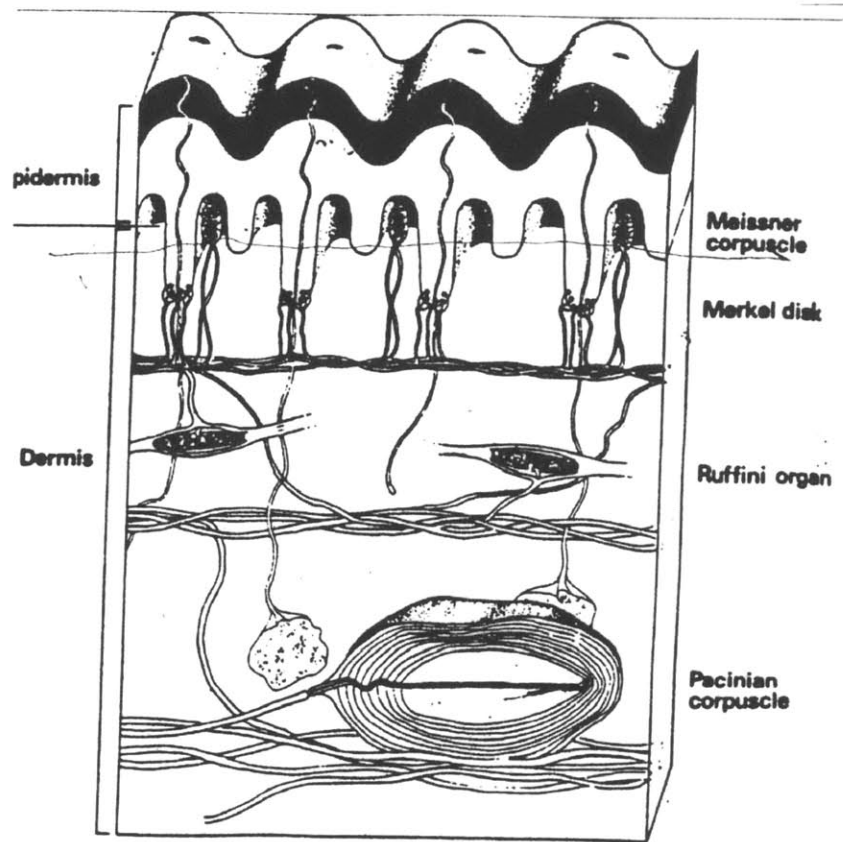
Figure 2-1. The major four mechanoreceptors within the human skin.
(The figure is from Ian Darian-Smith, 1984).

2.2 The Human Tactile Sensing System

The human tactile system is capable of coding and decoding touch information in an efficient and expedient manner. Physical contact of the object with the fingertip is the essential first step in gathering information about the object using the tactile sense. Because of the contact, mechanical loads are imposed on the skin surface causing the fingertip to deform. All the tactile information about the object is contained in the spatio-temporal variations of the contact forces and the region of contact. At any instant of time, these loads give rise to a unique state of stress inside the fingertip in general, and in the vicinity of the mechanoreceptors located below the skin in particular. The information about the object in contact with the skin on the surface is now contained in the stress state in the fingertip. Triggered by the stress-state in the close vicinity of the mechanoreceptors, the population of mechanoreceptors responds with trains of impulses which are conveyed to the central nervous system by peripheral afferent fibers. The information

about the object in contact is coded in the spatio-temporal variation of the discharge rate of the population of receptors. The neural code is processed by the brain, when the object is finally "perceived" through the tactile sense.

Biomechanics of skin and subcutaneous tissues plays a fundamental role in the human tactile sense. It governs the mechanics of contact with the object, the transmission of the mechanical signals through the skin, and finally the stress state at the mechnoreceptor location that is transduced into neural signals by the mechanoreceptors. It has been hypothesized that the differences in the temporal patterns of responses among the different receptor types to the same stimulus at the skin surface are due to differences in the "relevant stimulus", i.e., a particular combination of stresses/strain (and their derivatives) which triggers responses in that class of receptors (Philips and Johnson, 1981a). Further, the frequency of impulses emitted by a receptor is hypothesized to depend only on the local intensity of the relevant stimulus at the receptor site. Since the stress and strain fields are directly dependent on the mechanical stimulus at the skin surface, these hypotheses offer a mechanism for the neural coding of tactile information about the object and the type of contact (Srinivasan and Dandekar, 1996).

Historically, studies on tactile sensing by neuroscientist have been done to learn about the neurophysiological properties of the afferents, as well as the relationship between the stimuli and responses, by utilizing the peripheral neural recordings. These studies involved applying a known object to the fingertip of a monkey or human, recording the peripheral neural responses, and analyzing the data to infer the neural behavior of the mechanoreceptors such as the sensitivity, threshold, size of receptive fields, and mechanical-to-electrical transduction mechanism. Research work since 80s conducted by Srinivasan and LaMotte at Yale has been focused on the relationship between the properties of the object contacting the fingertip such as its shape, compliance etc., and the responses of the afferent nerve fibers. In order to identify the relevant stimulus of Merkel cells, Philips and Johnson (1981a, 1981b) recorded the neural responses of the mechanoreceptors innervating the monkey finger pad to steady indentations by a range of periodic and aperiodic gratings with rectangular bars and found that maximum compressive strain profiles calculated at a depth of 0.75 mm based on a simplified finger model were the best mechanical measure that could be linearly related to SA-I responses. Curved surfaces were pressed across the finger pad in a succession of steps (Srinivasan and LaMotte, 1987c) and stroked across the finger pad (LaMotte and Srinivasan, 1987a, 1987b, 1996), while

recording the neural impulse patterns. Some research done into temporal encoding pattern has been through sinusoidal movement (Goodwin and Morley, 1987) and vibration (Freeman and Johnson, 1982a) studies. Finger skin stretch and relative slip was investigated using glass plates with and without surface texture stroked across the finger (Srinivasan et al, 1990). The encoding of shape, both statically and dynamically, through RA and SA-I type afferent fibers has been studied extensively. Ramp and hold experiments were done by LaMotte and Srinivasan (1993), who proposed the hypothesis that curvature was the geometrical feature of the object encoded by the afferent responses. Goodwin et al (1995) studied the representation of curvature in the impulse frequency of afferent fibers innervating the monkey finger pad.

Some psychophysical research has been aimed at understanding the relationship between physical stimuli applied to the human skin, and the behavioral response of the human subjects, under carefully designed conditions. Specific studies have involved the tactile study of roughness perception (Lederman and Taylor, 1972), spatial resolution (Loomis, 1979), texture discrimination (Lamb, 1983), curvature discrimination (Goodwin et al, 1991; Goodwin and Wheat, 1992), softness discrimination (Srinivasan and LaMotte, 1995), and thickness discrimination (John et al., 1989; Ho and Srinivasan, 1996) during touch.

2.3 Non-invasive Imaging of Skin

Selection of a suitable technique for imaging skin is determined by the physical dimensions of skin tissues focused on and the level of resolution required. Skin consists of a superficial layer of epidermis (~0.15 mm in most parts and ~0.60 mm at palms and soles) and an underlying layer of dermis (1.2 - 1.8 mm thick). The total skin thickness in most parts of the body is typically less than 2 mm except at the palms and soles there it is thicker. The dermis consists of an upper layer called papillary dermis and a deeper layer called reticular dermis. The region beneath the reticular dermis consists of subcutaneous fat, which is sometimes considered to be a third layer of the skin and is also referred to as the hypodermis. When affected by certain condition, e.g., psoriasis or contact dermatitis, the skin thickness could increase significantly. This implies that the maximum skin imaging depth required is about 5 mm. To differentiate sub-layers within the skin, a resolution on the order of tens of microns is required. However, higher resolution than this has potential to identify other finer structures like papillary ridge, sweat ducts, and receptive nerve endings.

Commonly available imaging techniques such as x-ray and conventional ultrasound (operating at frequencies in the range 1-10 MHz) are generally used for imaging either the full thickness of human body or for imaging tissues that lie deep within the body (10 cm). The resolution provided by these modalities is about 1 mm, and hence they are not suitable for imaging fine structures within skin. Confocal microscopy (Rajadhyaksha 1995 & 1999), a technique that uses optical reflections from tissues, enables to visualize details at a cellular level with its high resolution ($\sim$ microns). However this technique is limited to imaging only superficial tissues ($\sim$0.35 mm) and it can only provide horizontal scans of the tissues, which makes impossible the display of vertical sections of skin tissues.

Previously, MRI has been used to image two-dimensional slices of the finger pad *in vivo* with high enough contrast and resolution to differentiate between all the soft tissues of the finger pad, and therefore, gives a precise picture of the tissue boundaries both while the finger is free or is in static contact with an object (Voss and Srinivasan, 1997). But higher resolution and lower imaging time is required to get a clearer look into fine skin structures.

To choose an imaging technique with which we can observe internal tissue deformations during touch, the imaging must be capable of being done under *in vivo* conditions, with resolution high enough to view the fine structure of, say, the outer and inner ridges of the finger pad, reasonable depth to include region of interest, and good contrast which depends on material properties of the tissue. Besides, in order to minimize motion artifacts during imaging, the time of imaging should be minimized. Otherwise any effort to obtain good resolution will be offset by gross motions due to involuntary movements of the subject's finger.

2.3.1 Optical Coherence Tomography (OCT)

A technique called optical coherence tomography (OCT) has been developed for noninvasive cross-sectional imaging in biological systems. It allows the visualization of microstructure within scattering materials (Huang et al., 1991). The main physical system involved in OCT is a simple Michelson interferometer, as shown in Figure 2-2. The light from the near-infrared low coherence source is split: one of the interferometer arms directs the light to the sample and the other to a moving reference mirror, whose position is precisely controlled by the system electronics. Light reflected from the sample is combined with light reflected from the mirror. As the length of the reference arm is scanned, interferometric modulation results at the detectors

26

only when the phase delay of the light collected from the sample is matched, to within the source coherence length, with the phase delay incurred in the reference arm. In this way reflections generated from material heterogeneity are collected as a function of depth. Because of the low coherence, the signal falls off rapidly with delay mismatch and the delay or longitudinal location of sample reflections can be determined with high resolution. The OCT system performs multiple longitudinal scans at a series of lateral locations to provide a two-dimensional or three-dimensional map of reflection sites in the sample.
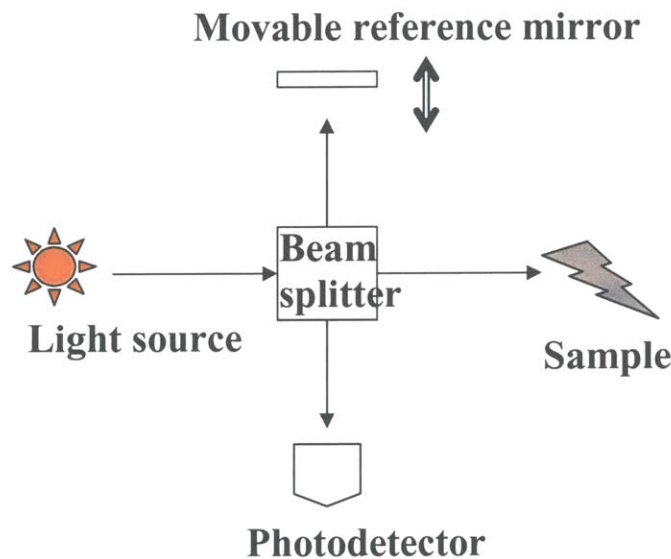
Figure 2-2. The general configuration of an OCT system.

OCT has grown rapidly since its potential for applications in clinical medicine was first demonstrated in 1991 (Huang et al.). The OCT setup proposed in Huang et al.'s paper had a resolution of 17 μm in air. Enhancing the resolution of OCT images continues to be very active field of research. Ultrahigh resolution OCT requires extremely broad bandwidths. A superluminescent diode (SLD), as used in the first OCT system, comes close to being the ideal source for OCT imaging due to the high irradiance and relatively low cost. However, the coherence length of SLD's, which is typically 10-20 μm, is insufficient to image individual cells or subcellular structures such as nuclei in tissue. Advances in solid-state laser have enabled the development of ultrahigh resolution and a longitudinal resolution of 1 μm can be achieved in

transparent tissue like the frog tadpole (Drexler et al. 1999 and Morgner et al. 2000). Vabre et al. (2002) achieved 1 μm axial resolution in imaging tadpole eye by using white-light thermal lamp, and Povazay et al. (2002) achieved ~0.6 μm axial resolution also by using a light source in the visible wavelength region. As for *in vivo* OCT of human skin, which is turbid tissue, to our best knowledge, the best longitudinal resolution achieved till now is 2 μm (Fujimoto et al., 2000).

Although probing depths exceeding 2 cm have been demonstrated in transparent tissues, including the eye and the frog embryo, optical imaging in non-transparent biological tissues is, in general, a difficult problem, primarily due to the scattering of light by the tissue. The attractive spectral region for OCT imaging in non-transparent biological tissues is near 1.3 μm, where light scattering is low relative to scattering of light in the visible region, and the tissue absorption is low. In this wavelength region near 1.3 μm, good penetration depth can be achieved in biological tissues.

Besides the improvement in the resolution and the depth of penetration, high-speed image acquisition is essential for suppressing motion artifacts when imaging living system: Tearney's system in 1996 achieved 4 images/second to image a beating frog heart and Rollins et al. (1998) used a rate of 32 frames per second. It has also been interesting to the investigators to add extra functions such as birefringence property (PS-OCT by de Boer et al. 1997) and Doppler shift to the OCT system to extract extra information from the tissues (Pierce et al., 2002; Park et al., 2003).

The OCT technology has also been applied to the human skin during its development (Schmitt et al. 1994). The human skin is turbid, for which optical attenuation is higher, backscattering is weaker, and reflections are poorly defined; moreover, multiple scattering and speckle complicate the interpretation of the OCT signals. Tearney et al. (1995) obtained refractive indices of both *in vitro* and *in vivo* human tissues using OCT technology; Pan et al. (1996) were the first to show an *in vivo* fingertip OCT image that the stratum corneum and the living epidermis were visible. Rollins et al. (1998) imaged the fingertip at a scan rate of 16 frames/second with good resolution. Pagnoni et al. (1999) used OCT to investigate the difference of the volar forearms between an African American subject and a Caucasian subject, the acne vulgaris, the cutaneous changes induced by exposure to water and dimethyl sulfoxide, and corticosteroid atrophy. And Zhao et al. (2002) used their novel OCT setup to display the Doppler shift, which shows the blood flow in the vessels, as well as structural OCT image of human skin *in vivo*.

28

2.3.2 Ultrasonic Backscatter Microscopy (UBM)

Ultrasound is a well-known medical diagnostic tool, which uses sound waves having frequency higher than 20 kHz, the upper limit of human audible range. When sound waves are propagated through a human tissue, they are reflected and scattered by the tissue. These reflected signals are then analyzed to obtain information about the tissue. In conventional diagnostic imaging, sound waves in the frequency range 1 to 10 MHz are commonly used and anatomical information with a resolution of about 1 mm can be obtained from tissues lying as deep as 10 cm. And since non-ionizing (acoustic) waves are used, the technique is non-invasive.

Ultrasound backscatter microscopy (UBM) is similar to diagnostic ultrasound imaging, but uses shorter pulses with higher center frequencies (20 MHz-150 MHz), and consequently achieves resolutions higher than diagnostic ultrasound systems. Because of increased attenuation of acoustic waves at higher frequencies, UBM sacrifices penetration depth to attain increased resolution. Typically penetration depths up to 1 to 2 mm have been reported with resolutions between 20 and 100 μm, the exact values depending on the transducer characteristics. The bandwidth of the transducer has to be high in order to achieve good axial resolution.

Previous work on ultrasonic imaging of skin has mostly involved 20 MHz systems. Examples of such works include evaluation of tumors (Fornage 1993, Hoffmann 1992, Edwards 1989, Harland, 1993), scleroderma (Ihn 1995), psoriasis (Gupta 1996, Vaillant 1994), burn injuries (Cantrell 1978), contact dermatitis (Seidenari 1998), radiation fibrosis (Gottlober 1997), photoaging (Gniadecka 1998, de Rigal, 1989), and study of the effects of cosmetics (Levy 1994). Systems operating at frequencies greater than 20 MHz have also been demonstrated (Passmann 1996, Foster 1993), with which the B-scan imaging of the skin can visualize fine structures such as veins and hair follicles (Turnbull 1995, El Bammal 1999). High frequency (>20MHz) ultrasound has numerous potential applications in dermatology because of its ability to penetrate several millimeters into the skin and provide information at a spatial resolution of tens of microns. The shorter pulse length leads to an improvement in the axial (along the beam propagation) resolution and the higher frequency leads to better lateral (perpendicular to the beam propagation) resolution. The depth of penetration is about 5mm, which is smaller than that of conventional ultrasound, but is sufficient to image skin tissues.

A UBM system was developed in MIT Touch Lab (Raju and Srinivasan, 1999 and 2003) using

polymer transducers with center frequencies 28, 30, and 44 MHz, a pulser/receiver, high-speed digitizer, 3-axis scanning system, and a PC. This system has been used to develop quantitative methods using the attenuation coefficient, backscatter coefficient, and echo envelope statistics to characterize normal human skin *in vivo* (Raju and Srinivasan, 2001, 2002 & 2003). With resolution around tens microns, this setup can perform fast imaging of wide area of skin (over 1 cm for a few seconds) and can peek into the inner structures under the skin up to 5 mm.

2.3.3. Elastography

Ultrasound elastography has been first introduced in 1991 (Ophir et al.), and this area has shed light on in vivo clinical detection of lesions and tumors, which had very poor accuracy through palpation diagnosis and pure visual inspection of traditional medical images.

The process usually involves external compression. One method to obtain axial deformation of tissue is apply time domain cross-correlation analysis: RF signals were taken before and after tiny axial compression, then cross-correlation was calculated on pairs of A-lines to find the time delay at which the cross correlation function reaches the maximum, thus the displacement and strain, the differential of displacement, of tissue structures were found. Another method (Bohs and Trahey 1991) calculated the sum of absolute difference (SAD) to find the matched pixels before and after tissue compression, thus obtain the displacement. Using the SAD algorithm, the computation time can be greatly reduced. Other methods like Fourier-based speckle phase tracking (O'Donnell et al. 1991), power spectral methods (Konofagou et al. 1999) and optical flow methods (Bertrand et al. 1989) have also been proposed.

Some mechanical limitations on strain imaging have been documented in the literature. For example, accurate strain measurements can only be obtained for large surface displacements, but larger compression can result in decorrelation of signals because many scatterers can move out of the image plane. To overcome this limitation, sometimes a large set of images is recorded with small relative displacements but with significant total displacement from the beginning to the end of the set. Single deformation on the order of micrometers has been generally used. Some other post-processing methods to improve images, temporal stretching and multicompression (Varghese & Ophir, 1996; Varghese et al., 1996; Varghese, 1997; Alam et al 1998), for instance, have also been proposed and show substantial improvement. A metric to evaluate the

performance of strain imaging, strain filter (Varghese & Ophir 1997), has been developed, which can give pre-assessment of the function of the imaging system before running real experiments. With the knowledge of stress distribution and boundary conditions, the strain images can be transformed to an elastogram, which is a relative measure of the distribution of elasticity modulus. Because the stress distribution is not uniform in almost all the real cases, it is not easy to reconstruct a reliable modulus distribution map. This reconstruction, or the inverse problem, has been a key issue which was discussed in many papers (Raghavan and Yagle 1994, Sumi et al. 1995, Skovoroda et al. 1995, Kallel and Bertrand 1996, Soualmi et al. 1997, Doyley et al., 2000, Miga 2003).

Most previous elastogram research used low frequency ultrasound (<~5MHz), except for some systems with frequency higher than 20 MHz (Fortin 2000, 2003; Vogt 2002). And as expected, better resolution in the elastogram can be achieved with higher frequency ultrasound systems. In Vogt et al.'s research (2002) on imaging skin with high frequency (22 MHz) ultrasound, they could see strain difference in epidermis, dermis and subcutaneous fat, and it was concluded that high frequency ultrasound based strain imaging is a potential tool for evaluation of the elasticity of skin structures. In their experimental setup, the deformation of the forearm skin surface was caused by stepwise increase of negative pressure applied to the skin surface.

2.4 Finite Element Method

The finite element method has been widely used to solve physical problems in engineering analysis and design. It is based on the concept of dividing the material continuum into a number of small elements, each of which can have a distinct set of mechanistic properties. These elements are joined together subject to continuity requirements in the process known as assembly and each element contributes to the overall mechanistic properties of the object and the solution of the underlying differential equations of equilibrium. Boundary conditions can be specified at any point in the model and loads can be imposed either to specify the prescribed displacement or the prescribed force experimental paradigm. The physical problem is first idealized by a mathematical model, in which assumptions are made about the geometry, material properties, loading, boundary conditions, etc. of the physical problem. Fluid dynamics, heat transfer, and solid mechanics problems are all examples of types of physical problems that can be modeled,

31

each with its own set of assumptions and governing equations, which in general cannot be solved analytically.

The finite element method is a tool to solve these governing equations numerically. Take a continuum-mechanics mathematical model as an example: the continuum model is first divided into a discrete number of elements and nodes, which encompass the entire volume of the problem. The external forces on the system are lumped into the element nodes. Each element is controlled by the equilibrium equations governing the entire model. These elements are then assembled together so that they satisfy a set of compatibility requirements, and an algebraic set of simultaneous equations is developed. This set of equations can be quite large for a problem of significance, and therefore, usually computer algorithms are used to solve this set of equations efficiently. The final solution satisfies the equilibrium equations only at the nodes and across each individual element, instead of continuously throughout the entire model. The stress-strain fields are continuous across each element, and it is only at the boundaries where discontinuities occur. Therefore, the mesh is refined to a point where the fields are reasonably continuous. If the element mesh is fine enough, then the nodal solution will be in close agreement with the continuum solution. It must be understood, however, that this is a numerical solution to the mathematical model, not the physical problem itself. If the initial assumptions in the model are incorrect, then a finer mesh will still produce erroneous results. Commercial finite element analysis software (ABAQUS, ADINA ..etc) has been developed over several decades and extensively used for the numerical analysis.

2.5 Modeling of the Primate Fingertip

The biomechanical approach to tactile sensing focuses on the mechanical aspects of touch including determination of mechanical properties of skin and other fingertip tissues, mechanical modeling of the finger pad, computation of stress-strain measures in the vicinity of the mechnoreceptors, and a study of the relevant stress-strain parameters which cause the various mechanoreceptors to fire neural impulses.

In Phillips and Johnson's study (1981b) of the relationship between subsurface strain measures and neurophysiological recordings, to calculate the stress and strain values at typical receptor sites within the skin, they assumed the finger as a homogeneous, isotropic, incompressible and linearly elastic half-space in a state of plane stress or strain with infinitesimal deformations. In

1987, Van Doren modeled the fingertip as an infinitely wide flat medium of finite depth to investigate the mechanical response to spatiotemporal sinusoids. The material was modeled as linear, homogeneous, isotropic, viscous and elastic and the results of the analysis suggested that normal strain triggered the mechanoreceptors in the tissue. Although these models approximately predict the neural responses, they used broad assumptions which do not take into account the geometrical shape or mechanical behavior of the finger pad. In addition, they cannot account for changes in area of contact or non-linear behavior.

A "waterbed" model was created (Srinivasan, 1989) in which the fingertip was modeled as an elastic membrane enclosing an incompressible fluid. Even though it accurately predicted the measured *in vivo* skin surface deflection profiles of primate finger pads under line loads, it failed to match the variations in the responses of the receptors at different locations in the skin due to the uniform tension in the membrane and uniform pressure field within the fluid. Gulati and Srinivasan (1995) indented human fingertips with point, flat circular and flat plate indentors and measured the temporal force response. They proposed a lumped parametric model consisting of a nonlinear spring in parallel with a series of piecewise linear spring-dashpot links to explain the temporal force response profiles observed. This Kelvin type model predicted well the nonlinear viscoelastic force response.

Dandekar and Srinivasan (1997) began to model the fingertip using finite element method to investigate the skin mechanics during touch. Besides a two dimensional multilayered model, a three dimensional model of the fingertip was produced with realistic external geometry, incorporating multiple internal layers for the epidermis, dermis, and bone, which accurately predicted the surface deformation during contact and was able to determine the stresses and strains occurring under the skin surface. They found strain energy density and maximum compressive strain at the receptor location were linearly related to the recorded neural discharge rate of SA-I afferents under multiple mechanical stimuli and emerged as the candidates for relevant stimuli for triggering the response of SA-I afferents.

However, this model had limitations in that the size of the elements on the surface of the fingertip was not high enough to simulate indentation by steeply curved surfaces like the edges of a rectangular bar. This means that the edge enhancement effects of SA-I responses cannot be effectively studied using that model. With higher resolution mesh applied to this model, Raju and Srinivasan (1999) determined that the strain energy density was a good candidate as the relevant

stimulus for SA-I afferent fibers. But because the model was based on the raw unsmoothed data from measurement of primate finger and the surface of the finger model is actually polyhedral due to the finite number of nodes, even though it has high spatial resolution, artifacts were introduced in the surface pressure distributions wherever the surface of the finger has local bumps. These artifacts were seen to manifest as spurious peaks and a 4×1 median filter was used to eliminate these peaks in the surface pressure distribution.

With the assumption of plane strain, Cysyk and Srinivasan (1999) created a 2D model which could predict empirical results and saved enormous computational effort. To model the finger pad more accurately, realistic geometric and mechanical properties are very important pieces of information to be incorporated. Gulati and Srinivasan (1996) obtained the force response profiles from ramp and hold indentations into the finger of human subjects. Dandekar and Srinivasan (1997) measured the human fingertip shape using videomicroscopy and included the data to their 3D model. Using a 4.7 Tesla magnetic resonance imaging (MRI) system, Voss and Srinivasan were able to image the whole cross-section of the finger (1998) under both undeformed and deformed conditions. Cylinders, bars, and line loads were indented into the subjects' fingers to various depths and held stationary for imaging. These images provided good contrast between skin, fat, and bone, and have contributed to the geometric parameters of the model of Cysyk and Srinivasan (1999). Surfaces were stroked across the finger of human subjects to determine the friction coefficient of skin (Liao and Srinivasan, 1999), which was found to be a function of the indentation depth. Raju and Srinivasan (1999) imaged the finger pad using customized ultrasound backscatter microscope, intending to get internal geometrical information of finger pad.

2.6 Need for an Improved Model

The current human fingertip model for studying the biomechanics of human touch (Zhou and Srinivasan, 2002) has smooth skin surface on the finger pad and smooth boundary between the dermis and epidermis, which does not mimic well the real situation. And because SA-I and RA mechanoreceptors reside in the vicinity of the papillary interface between the epidermis and dermis, these fine structures can be important and need to be incorporated. As described, OCT imaging could be employed to look into the fine structures of the fingertip skin and UBM could be used in the strain imaging to estimate the stiffness variation within the skin top surface. After

34

adding these extra features to improve the model, the simulation results have to be validated against the OCT images and the force response data of the deformed human fingertip.

Chapter 3
OCT Experiments

When the human fingertip is in contact with an object, the skin and subcutaneous soft tissues deform to resist the load due to contact. As the load increases, the tissues respond with increased displacements, accommodation and resistance. Most of the measurements of mechanical behavior of biological tissues have been obtained from *in vitro* experiments. However, studies show a significant difference between *in vivo* and in *vitro* tests due to loss of fluid, changes in the differential proteins and alterations in boundary conditions (Lanir, 1987). In previous research conducted in the MIT Touch Lab on the human fingertip *in vivo*, videomicroscopy was used to image the external surfaces of the deformed fingertip (Dandekar and Srinivasan, 1995), and MRI was used to image the internal structures of the entire cross section of human fingertip under load (Voss and Srinivasan, 1997). A non-invasive method for observing this deformation process close to top skin surface of the fingertip with higher resolution can be through the use of optical coherence tomography (OCT). An OCT image contains intensity, texture and spatial information which can aid in determining the tissue type, location and boundaries, thus produces structural information on soft tissues and their material behavior.

To study the biomechanical behavior of the tissues *in vivo*, static loading of the human index fingertip using different stimulus shapes indented to different levels was applied and OCT images were taken. Approval for these studies involving human subject was granted by MIT's COUHES. The images were used to obtain information on internal and external geometry of the fingertip skin as well as its mechanical behavior. In order to extract structural information from the images, the external and internal boundaries were outlined to tag their location and monitor their displacement when the fingertip was under load. Since the goal is to enhance the understanding of the somatosensary neural signal transduction, it is important to locate the mechanoreceptors with high resolution OCT, so that in the later work of modeling the transduction process, the strain and/or stress around the mechanoreceptors can be investigated to understand their neural response to external compression and/or shear. The OCT images thus provide a basis for developing a finite element model of the fingertip skin.

3.1 Equipment setup

36

3.1.1 OCT System

Two different OCT setups with different resolutions and fields of view have been used in the experiments:

Setup A:

This fiber-based OCT system was developed by Dr. Johannes de Boer's lab at Massachusetts General Hospital and described in Pierce's paper (2002). The light source had a center wavelength of 1310 nm, a FWHM bandwidth of 70 nm and total output power of 9 mW. Light was coupled through standard single-mode fiber to a polarization-independent optical circulator and then divided by a fiber optic splitter in a 90:10 ratio into the sample and reference arms. 2.5 mW of source light was incident onto the sample surface in a focused spot of 30-μm diameter. The electronic signals from each detector were amplified, filtered, and digitized with a 12-bit 5-Msample/s A/D board. Even though the resolution of this machine (on the order of 10 microns axially) is unable to resolve the mechanoreceptors within the skin, its large field of view (up to 7 mm), fast rate of data acquisition (up to 2Hz) and tunable focus are suitable for obtaining skin deformation from *in vivo* experiments involving multiple indentors with different thicknesses.

Setup B:

SkinDex300 is an OCT equipment developed by ISIS Optronics, Germany. The wavelength of the light source is 1300 nm, and the resolution of the images is as high as 3 μm (lateral) x 5 μm (depth). Even though the image data acquisition rate is pretty low (~ 4 seconds for one frame) and the field of view is fixed as 1 mm (lateral) x 0.9 mm (depth), its high resolution has the potential to visualize mechanoreceptors within the depth of 0.9mm.

3.1.2 Indentation Setup

The indentor, also acting as an objective lens in the OCT setup, was attached to a donut shaped load cell (SENSOTEC Model D/189611), which was fixed on a rigid frame and activated by a single channel signal conditioner-indicator (SENSOTEC Model HM). The finger pad of the subject's right index finger faced the indentor horizontally with the nail glued to the vertical frame of a manually controlled micro-positioning stage (Parker Hannifin Corp., Cleveland, OH), which moved the finger toward the indentor and pressed the finger against it. Index matching gel

was applied between the fingerpad and the indentor to displace the air at this interface so that the back reflections due to the difference in refraction index can be reduced. The vertical position of the finger was adjusted such that the center of the finger pad was well aligned with the center of the indentor. When the fingertip was pressed against the indentor, the total load applied to the fingertip was measured by the load cell and displayed. The experimental setup (setup A) is shown in Figure 3-1.
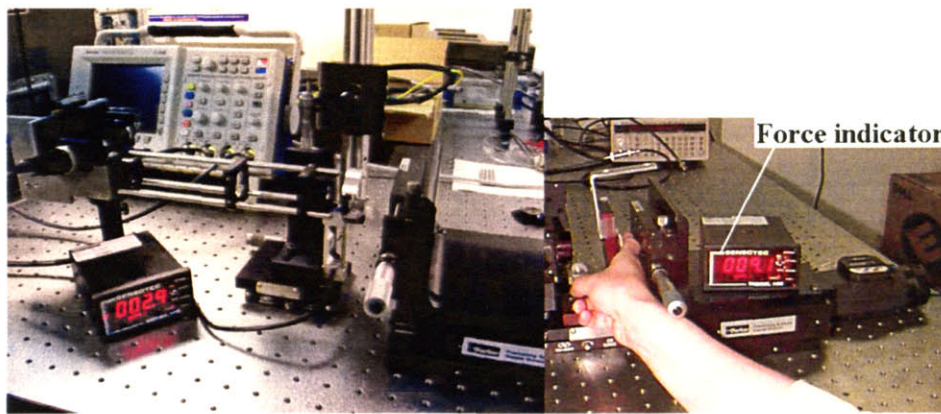
Figure 3-1. The experimental setup (setup A).

3.2 Materials and Methods

3.2.1 Shaped Indentors

Different shapes of indentors were prepared for the experiment:

1. Flat indentor

In the OCT setup, a microscope slide was placed at the position of the objective lens to be used as an indentor with flat surface to indent the human fingertip.

2. Spherical indentor

The plano-convex lenses (COHERNET Inc., Santa Clara, CA) of different focal lengths (15F and 50F) were used as the spherical indentors. Substituting into the lens maker's equation $\frac{1}{f} = (\frac{n_{lens}}{n_{air}} - 1)(\frac{1}{R_1} - \frac{1}{R_2})$ with $n_{air} \sim 1$, $n_{lens} \sim 1.52$ and $R_1 \rightarrow \infty$, the radii of curvature of the lenses can be obtained as 7.8mm and 25.9mm, respectively.

3. Rectangular bar indentor

38

Figure 3-2 shows the dimension of an indentor with a thin rectangular bar protrusion made of glass wafer (Optics, Santa Ana, CA). The glass wafer, made of soda lime glass, was cut using a die saw into a rectangular bar and a squared piece and glued together to form the desired shape. These indentors were transparent and their high stiffness (Young's modulus for glass ~10.6 Mpsi) satisfies the assumption that they are rigid relative to the fingertip skin. They were attached to the load cell at their flat sides and faced the finger pad with their shaped sides during the experiment.
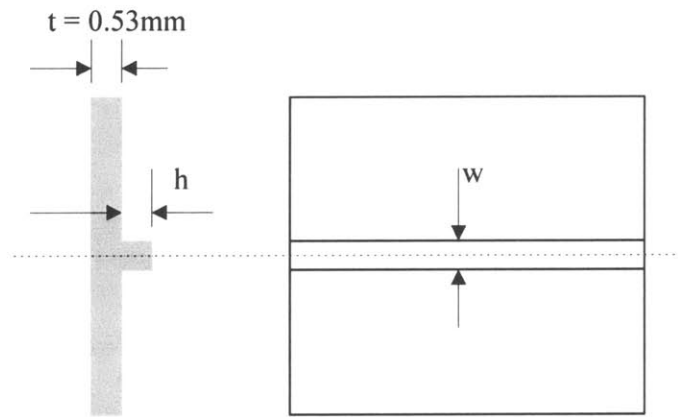
Figure 3-2. The dimension of the indentor made of glass wafer with thickness 0.53 mm. h = 0.53 mm, w = 0.44 mm.

3.2.2 Experimental Procedure

The experiments were conducted on the sample arm of the OCT equipment (Figure 3-3). The indentor acted as the objective lens itself when used. The indentor was rigidly attached to the load cell, so the indentation force could be measured during the indentation. The human subject's finger was immobilized by gluing the fingernail to the micro-positoning stage to reduce as much as possible the unwanted movement during imaging. The displacement of the stage was controlled manually by the experimenter to move the finger by a desired amount to press against the indentor, while the OCT images were taken with approximately top 1mm of the skin surface of the fingertip in focus. To explore the static responses under a variety of conditions, the indentor shape (as described in Section 3.2.1) and the indentation depth were varied. In order to accurately identify the structures within the human skin, images of histological cross sections of both fingertips and skin from literature were used for comparison.
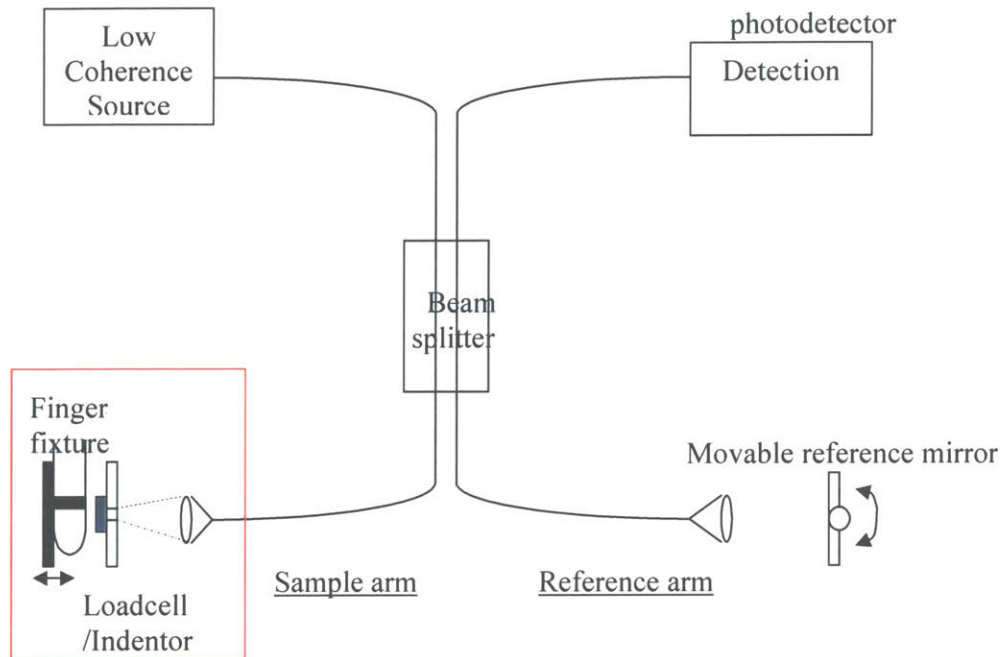
Figure 3-3. The schematic of the OCT system.

3.3 Postprocessing of the Images

The OCT images were taken to assist in creating an idealized model of the fingertip, which would represent the essential geometrical and material characteristics. However, care was needed in processing these images in order to optimize the available information. To analyze and interpret the biomechanical behavior of skin layers, proper segmentation of anatomic structures was accomplished so as to both label the layers and track their displacements.

3.3.1 Enhancement of the Image

Image enhancement refers to the processing of an image to make it more appropriate for either inspection by a human observer or automatic analysis by a digital computer. It allows for specific aspects of the image, such as edges or boundary of layers, to be emphasized. The techniques for image enhancement vary widely depending on the type of images and the nature of the application. For example, a histogram of an image represents the number of pixels at each intensity, which gives information regarding the range of intensity in the image, which can be adjusted to change the distribution of image brightness in order to enhance or minimize features

such as contours or noise. For the OCT images, histogram modification could be used to minimize background noise and quantization errors. Specifically, the histogram, or the distribution of intensity, could be stretched to fully make use of the intensity range (normally 0-255 in gray level). The application of linear filters is another method to enhance images. A low pass filter results in softening of the images, making it appear smooth but also hazy or blurred. A high pass filter emphasizes the contrast of local details (e.g. edges or boundaries), making the image appear sharper. Figure 3-4 shows an example of the postpocessing of the OCT images: Figure3-4(a) is the original OCT image; Figure 3-4(b) shows an image after stretching the intensity distribution to fully make use of the gray level available. In the display of the OCT images in the following, enhancement shown in 3-4(b) will be mainly used.

(a)

(b)
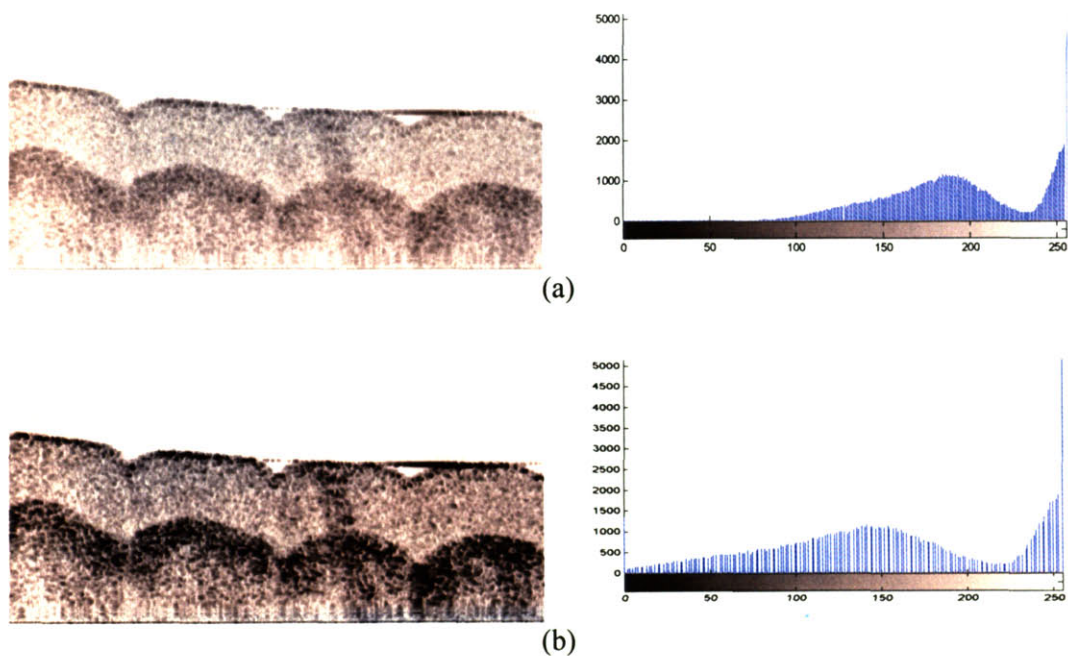
Figure 3-4. Enhancement of the image: (a) The original OCT image and its histogram (b) The OCT image after stretching the histogram and the corresponding histogram.

The OCT images by nature contain significant amounts of speckles, which are due to the noise from random sources and can obscure the real structures. A method that has been widely used to remove the speckles in the OCT images is to take multiple images at the same spot and then overlay, i.e. linearly combine, all the images so the random speckles can be averaged out, leaving only the trace of the true structures. An example is shown in Figure 3-5. The image after

overlaying six individual images is smoother and can get rid of misleading patterns due to random speckles.

1.21mm

5mm

(a)

1.21mm

5mm

(b)
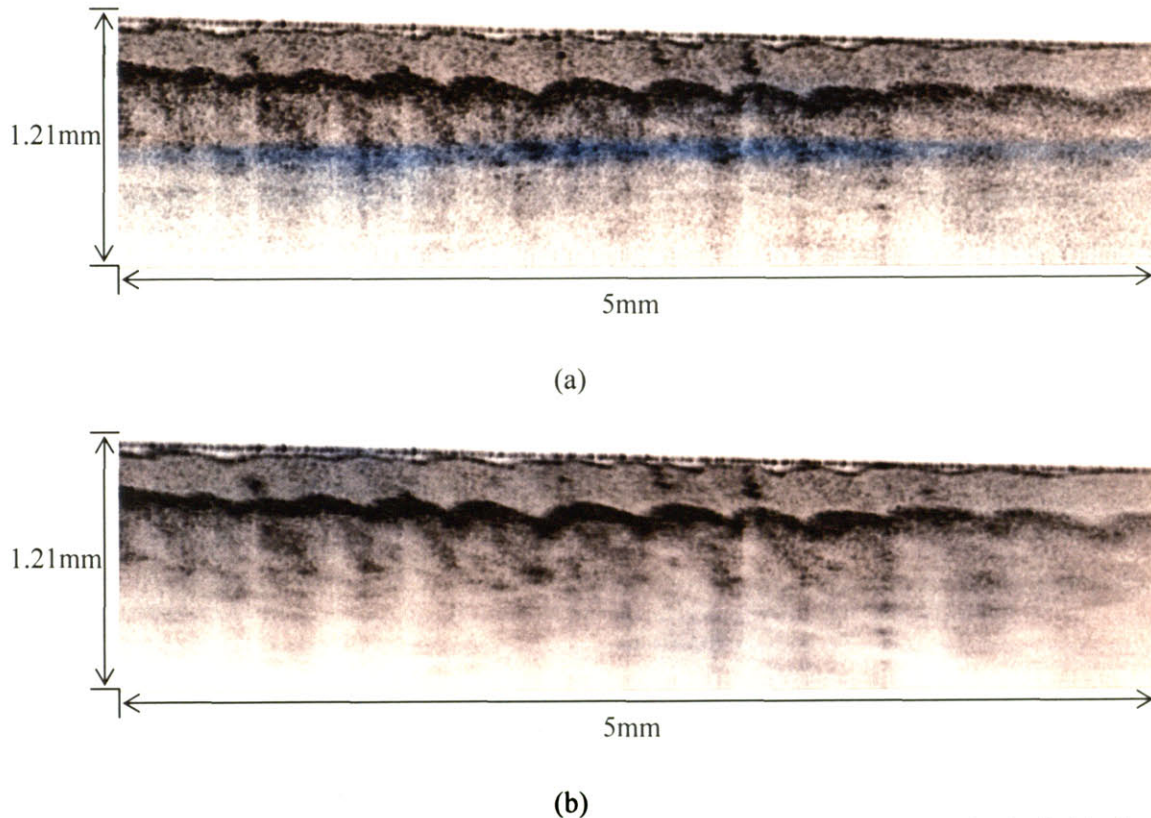
Figure 3-5. An OCT image in a single shot (a) and an image after an overlay of 6 individual images taken at the same location (b). Note the reduction of speckle at the bottom of the image in (b).

3.3.2 Boundary Detection

To extract information from the image, boundary detection is needed to separate the tissue structures so that the location of the structure of interest and/or the displacement at certain location during loading can be recorded. An image can be segmented by several different techniques such as manual method, thresholding, automatic edge finding techniques, connectivity and homomorphic operations. Two types of boundary detection were applied to the OCT images obtained in the experiments and are described below.

a. Profile of the top fingerpad surface and the boundary below the stratum corneum

Figure 3-6 shows an image of the fingerpad when no load was applied and a photomicrograph from a book by Krstic (1991) for comparison. The dark line at the top of 3-6(a) is the trace due to

42

the surface of the objective lens (or flat indentor). The clear region between the lens surface and the ridged surface of the finger pad shows that there is no contact. From this image, it can be seen that the width of each ridge at the center of the finger pad is about 0.4mm and besides the top ridged surface, a boundary between the stratum corneum and the tissue below it (the papillary layer within the epidermis) is quite clear and should be used to mark the basic structure. One way to gain information on deformation of the skin tissue is by analyzing tissue boundary profiles in the OCT images before and after contact with an indentor. Some dark spots under the most left ridge within the stratum corneum was identified to be due to the sweat gland. Because these tiny sweat glands are randomly distributed within the skin without clearly known pattern. They were assumed unable to affect the biomechanical property of the skin tissue and were not included in the general structures tagging.

(a)

(b)
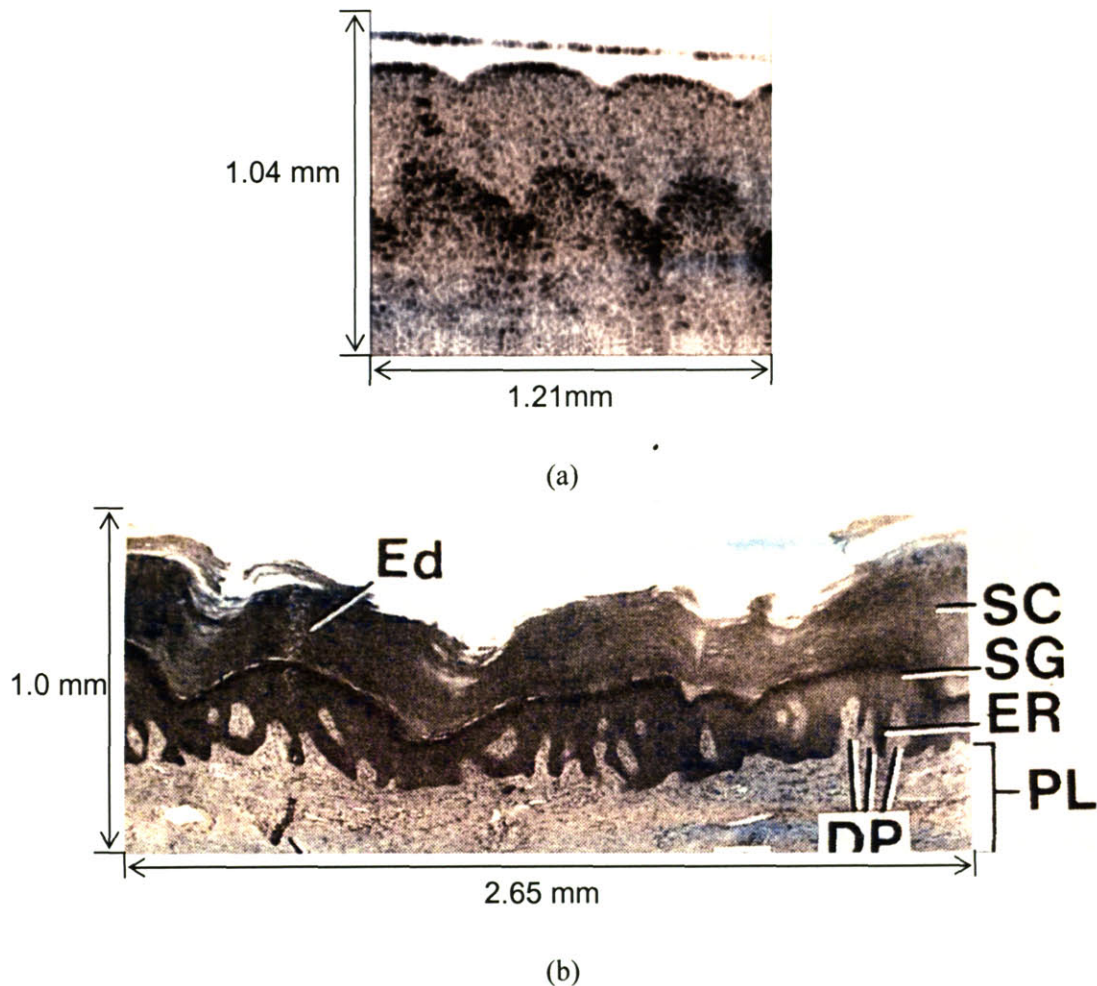
Figure 3-6. (a) OCT image of the human fingertip free of load to show the natural shape of the epidermis ridges. (b) Histology of the tissues of a human fingertip for comparison (Krstic, 1991). SC: stratum corneum, SG: stratum granulosum, ER: horny epidermal ridges, DP: dermal papillae, PL: papillary layer, Ed: excretory ducts.

To obain the profile of the skin surface from the OCT image, the first step was to remove the dark trace on top of the finger pad (as shown in Figure 3-6) due to the reflection of the light wave from the surface of the indentor. It is done by running a MATLAB code which allows the user to manually pick the area with the indentor trace and changes them into bright regions (Figure 3-7(a)). The second step was to search vertically from the top of the image for the spot on each A-line (i.e., each vertical line in the image) where brightness level dropped dramatically. A threshold algorithm was used in this search. Connecting all the spots on the consecutive A-lines forms the top surface profile of the finger pad (Figure 3-7(b)) in the image.

<center>(a)   (b)</center>
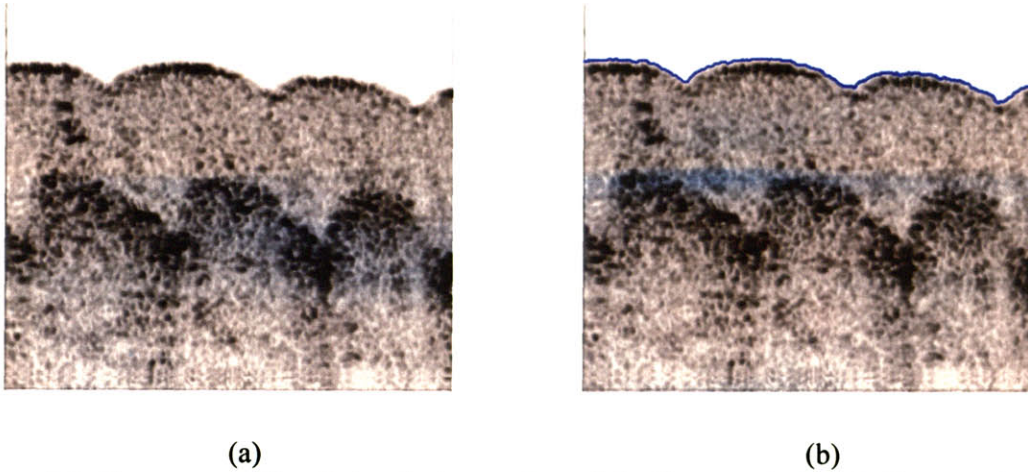
Figure 3-7. The process of outlining the top surface of the finger pad. Step 1: Remove the dark line at the top of the image due to the lens by "whitening" it ((a)). Step 2: Search from the top for the spot where brightness changed to a darker level (here a level below 200 was set) on each A-line and connect all such points on successive A-lines to obtain the profile ((b)).

For the inner boundary of the stratum corneum, an algorithm involving the intensity gradient of the image was used. This algorithm was initiated from an investigation of the map of vertical gradient of the original OCT image. Figure 3-8 is the gradient map calculated along the vertical direction of the OCT image in Figure 3-6. As can be seen, besides the location of the indentor surface and the top surface of the finger pad, a curved dark band, even if a little obscure, appears around the inner boundary of the stratum corneum. This dark band is due to the negative gradient value when high intensity area is above the low intensity area in the image with the pixels indexed from the top of the image to the bottom. This band is not necessarily the darkest area around that region, but it extends certain range to form a band with certain thickness. A code was developed which required the user to first pick any number of points on the boundary to "guide" the search, then the search automatically located the spot along each vertical A-line with the lowest averaged intensity within a "kernal" around the vertical positions of those guiding points. Connecting these spots on the entire consecutive A-lines formed the profile of the inner boundary of the stratum corneum.

<center>45</center>

Region with an
obscure dark band
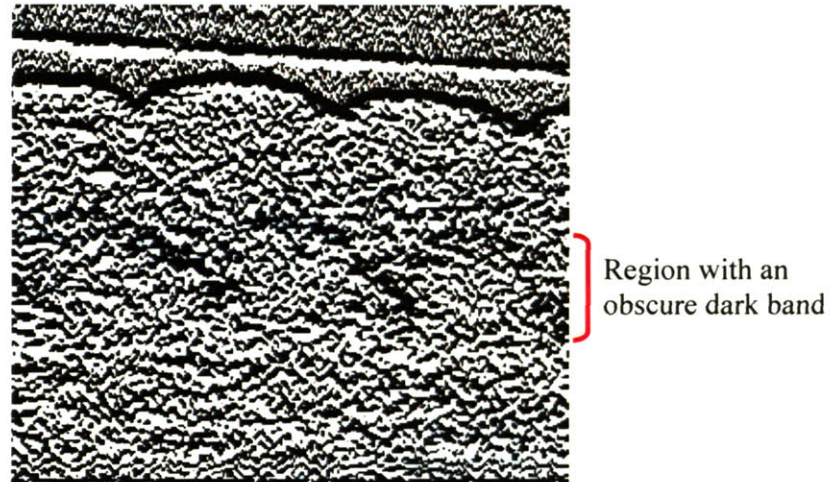
Figure 3-8. The gradient map taken in the vertical direction in the OCT image shown in
Figure 3-6. This map shows that besides the trace due to the indentor and the
top surface of the finger pad, the region below the stratum corneum also shows
a curved dark band.

Figure 3-9 shows the outcome of this search. In this specific case, 10 points were randomly
picked for guidance, with a kernal size of 6 pixels (~0.0244 mm) and a search region of ± 30
pixels (60 pixels ~ 0.244 mm). Because the resulting curve is rather fuzzy, a further step to
smooth it was applied. It was to fit the entire zigzag boundary profile with piecewise parametric
smooth curves. In the specific result shown in Figure 3-10, a cubic curve was fitted for every 33
points on this profile. As shown in the figure, even if the entire boundary is only piecewise
smooth, it appears much smoother than the original result in Figure 3-9.
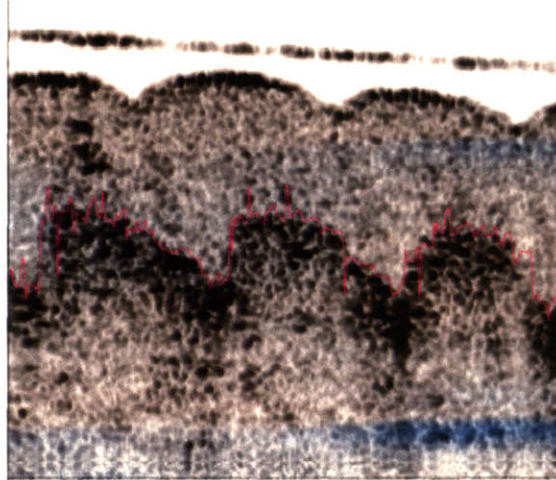
Figure 3-9. The boundary detected using the approach to searching for the thickest dark band along points picked by the user. In this case, 10 points were picked for guiding the search and the search kernal had a size of 6 pixels. The search region is 30 pixels thick vertically on both sides of the selected guiding points.
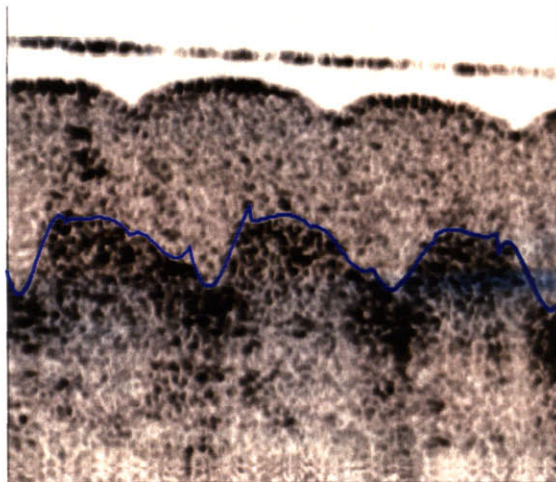
Figure 3-10. Option can be chosen to curve fit this zigzag curve. In this case, cubic curve was used to fit every 33 points along the boundary in Figure 3-9.

b. Boundary other than "layers"

For a boundary not extending over like a layer, the simple search over individual A-lines as described in subsection a above cannot be used. One method using active contour models or "snakes" to segment various edges, lines, or terminations has been made use of previously by

Voss and Srinivasan (1997) to outline the profile of closed contours in the MRI image of the cross section of human fingertip. A snake, originally developed by Kass (1987), is an energy-minimizing and controlled continuity spline which can be attracted and locked into the salient lines and edges due to the influence of internal forces, external image forces and user-provided constraint forces. However, the snakes do not try to solve the entire problem of finding image contours. They depend on other mechanisms to place them somewhere near the desired contour to guarantee good performance. If a user appropriately pushes a snake close to an intended contour, its energy minimization would carry it the rest of the way. Therefore the snake models were designed as interactive models that rely on the initial conditions.

If the position of a snake is parameterized as v(s) = (x(s),y(s)), the energy functional can be written as (Kass, 1987):

$$E_{snake}^{*} = \int_{0}^{1} (E_{int}(\vec{v}(s)) + E_{image}(\vec{v}(s)) + E_{con}(\vec{v}(s)))ds$$

where E_{int} represents the internal energy of the spline due to bending and can be written as $E_{int} = (\alpha(s) | \vec{v}_{s}(s) |^{2} + \beta(s) | \vec{v}_{ss}(s) |^{2})/2$, E_{image} gives rise to the image forces which push the snake toward salient image features like lines, edges, and subjective contours, and E_{con} gives rise to the external constraint forces responsible for putting the snake near the desired local minimum. This minimization procedure can be written numerically into code, which has been illustrated in detail by Kass (1987).

3.4 Experimental Results

a. Finger pad in contact with flat surface

A microscope slide was used as the indentor in this case. Figure 3-11 shows the OCT images of the right index fingerpad of a female subject under indentation depths ranging from 0.20 mm to 2.20 mm at increments of 0.50 mm. And the profiles of the skin top surface and the lower boundary of the stratum corneum were outlined by the method described in Section 3.3.2, as shown in Figure 3-12.

(a)   (b)   (c)

(d)   (e)
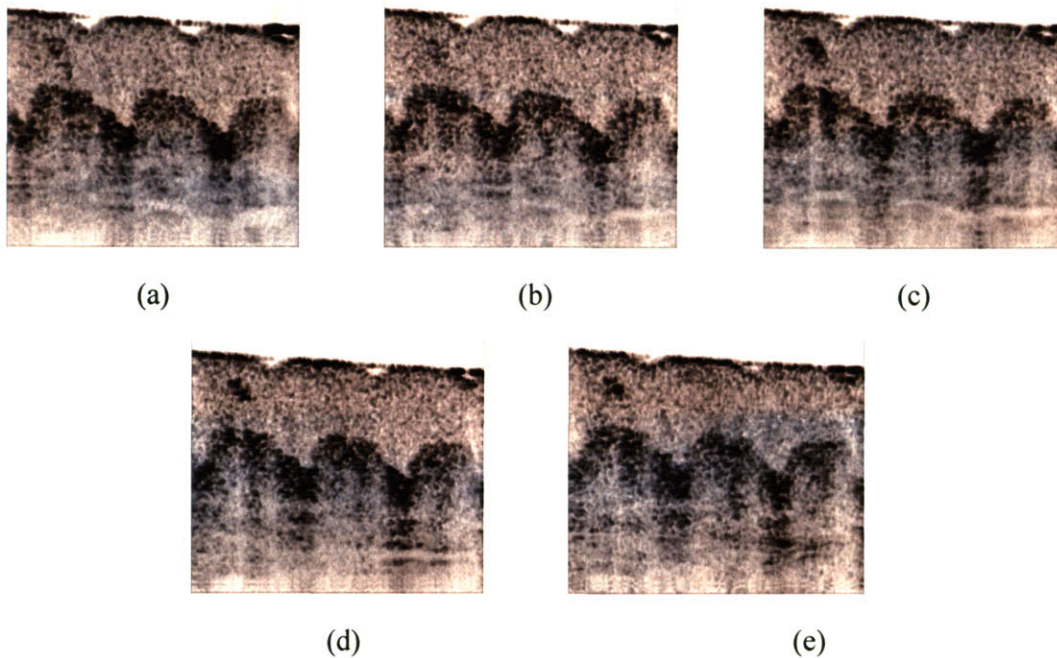
Figure 3-11. OCT images of the right index fingerpad of a female adult subject. The real dimensions of each of the images are 1.04 mm (vertical) × 1.21 mm (horizontal). The finger pad was indented to a depth of (a) 0.20 mm, (b) 0.70 mm, (c) 1.20 mm, (d) 1.70 mm and (e) 2.20 mm.

(a)   (b)   (c)

(d)   (e)
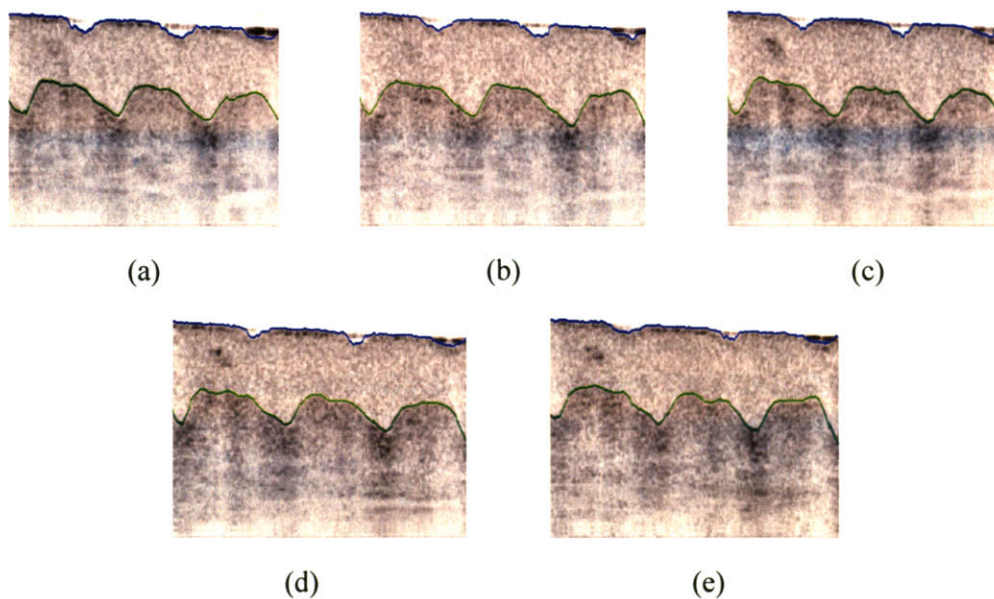
Figure 3-12. The OCT images in Figure 3-11 were processed so that the top surface and inner boundary of the stratum corneum were outlined.

Notice that because in the indentation process, the indentor did not move, but the fingertip was pushed against it, and that the imaging setup focused statically on the fixed spot at the indentor, these images do not show clear movement of either the indentor or the finger. Even though, the finger was actually indented to depths ranging from 0.20 mm to 2.20 mm in the series of images. To compare the deformation of the finger pad, all the profiles of the finger pad indented to more than 0.2 mm were superimposed on the one with an indentation of 0.20 mm. In Figure 3-13, the dotted curve shows the profile of the finger pad when indented to 0.20 mm, and the solid curve shows the profile of 0.70 mm, 1.20 mm, 1.70 mm, and 2.20 mm indentations, respectively.

(a)   (b)

(c)   (d)
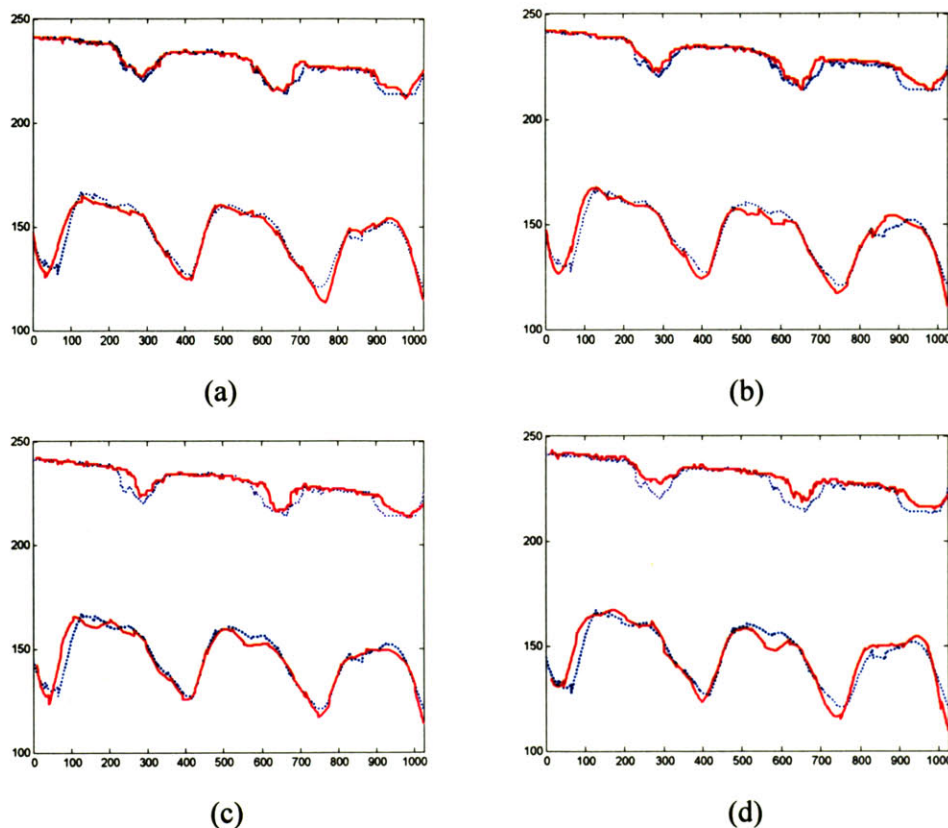
Figure 3-13. (a) 0.70 mm (solid line) v.s. 0.20 mm (dotted line) (b) 1.20 mm (solid line) v.s. 0.20 mm (dotted line) (c) 1.70 mm (solid line) v.s. 0.20 mm (dotted line) (d) 2.20 mm (solid line) v.s. 0.20 mm (dotted line). The values shown on the vertical and horizontal axes are pixel indices.

These figures do not show large differences among them during the indentation process except that the ridged skin surface in contact with the indentor became flatter, that is, the "grooves" on the fingerpad shrank, as indentation depth increased. Even at the indentation of 2.20 mm (load

data showing about 150 grams), the surface papillae still managed to hold the load well without total elimination of the grooves. Also, the thickness of the stratum corneum was not significantly affected, which implies that most of the compressive deformation occurred in tissues below the stratum corneum.

b. Finger pad in contact with a spherical surface

1. Radius of curvature = 25.9 mm

(a)   (b)

(c)   (d)
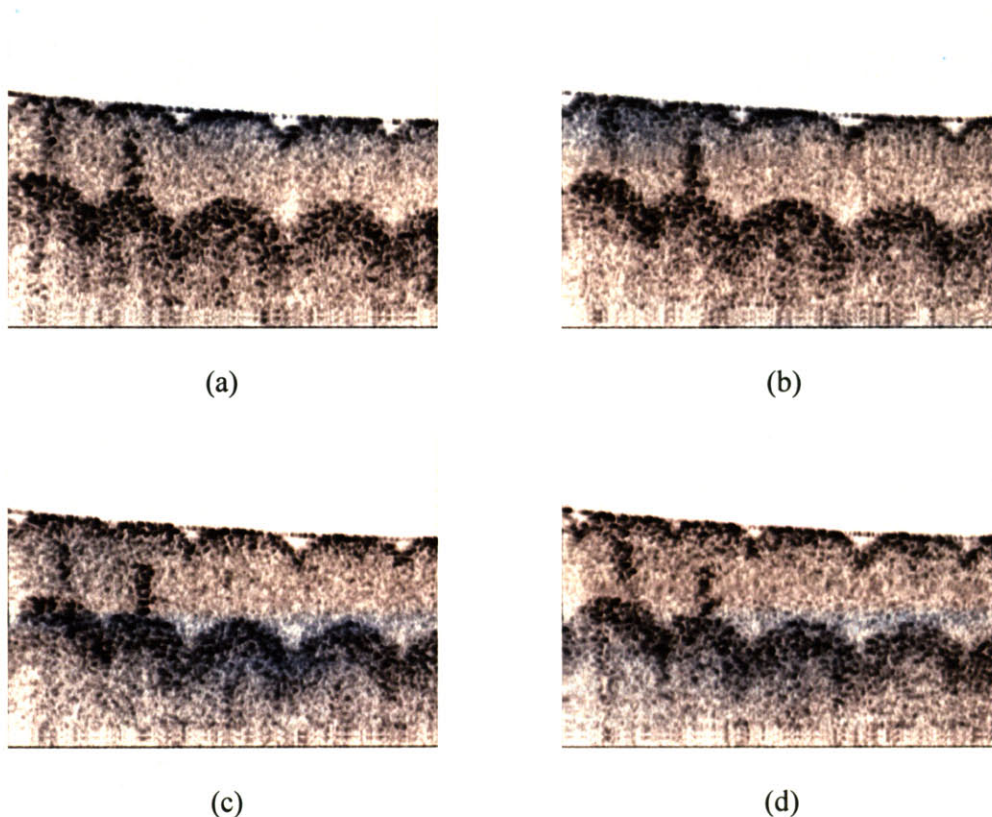
Figure 3-14. OCT images of the right index finger pad of a male adult subject. The real dimensions of each of the images are 1.21 mm (vertical) × 1.68 mm (horizontal). The finger pad was indented by (a) 10 grams load, (b) 20 grams load, (c) 30 grams load, and (d) 50 grams load.

A plano-convex lens (Coherent Inc.) of focal length 50 mm, or a radius of curvature of 25.9 mm, was employed in this experiment as the indentor. The finger pad was initially pressed against the lens, such that a reading of 10 grams was shown on the load cell indicator, and then the finger was moved toward the indentor to increase the load to 20 gram, 30 grams, and finally 50 grams. The OCT images from a male subject's right index finger are shown in Figure 3-14 and the

51

profiles of the skin surface and the inner boundary of the stratum corneum were outlined using the method described in Section 3.3.2 and shown in Figure 3-15.

(a)	(b)
(c)	(d)
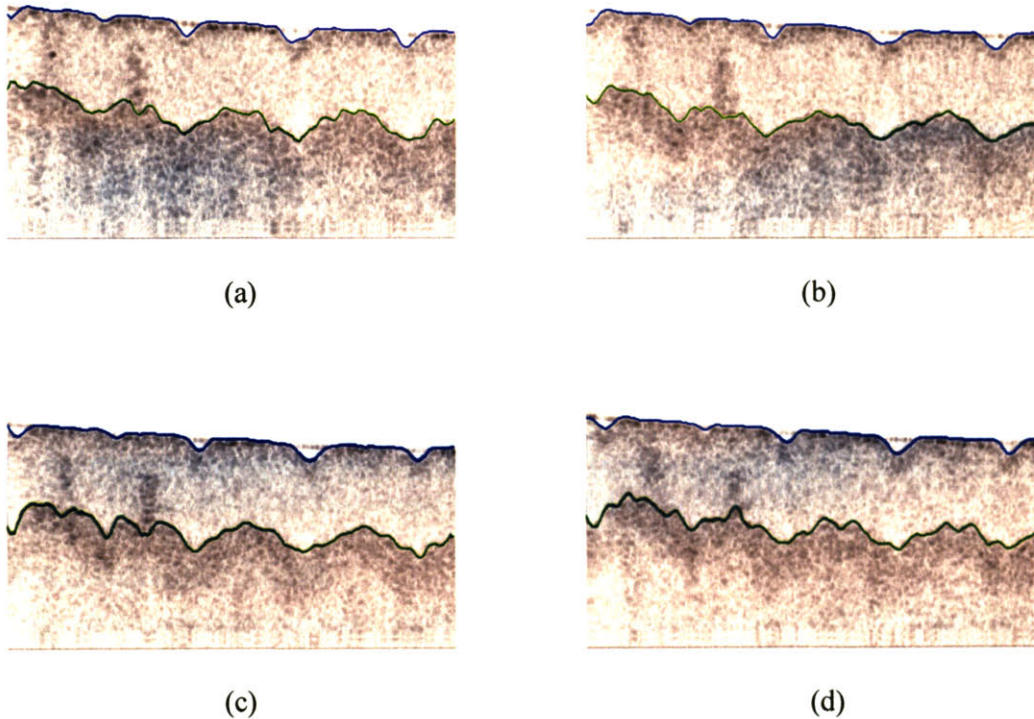
Figure 3-15. The profiles of the top skin surface and the inner boundary of the stratum corneum in the OCT images in Figure 3-14 were outlined. The real dimensions of each of the images are 1.21 mm (vertical) × 1.68 mm (horizontal). The finger pad was indented by (a) 10 grams load, (b) 20 grams load, (c) 30 grams load, and (d) 50 grams load.

To observe the effect of the indentation on the shape of finger pad area close to the indentor, all the profiles of the finger pad indented more than 10 grams were superimposed on the one with indentation of 10 grams. As shown in Figure 3-16, the dotted curve shows the profile of the finger pad when indented by 10 grams, and the solid curve shows the profile at indentation load of 20 grams, 30 grams, and 50 grams, respectively.
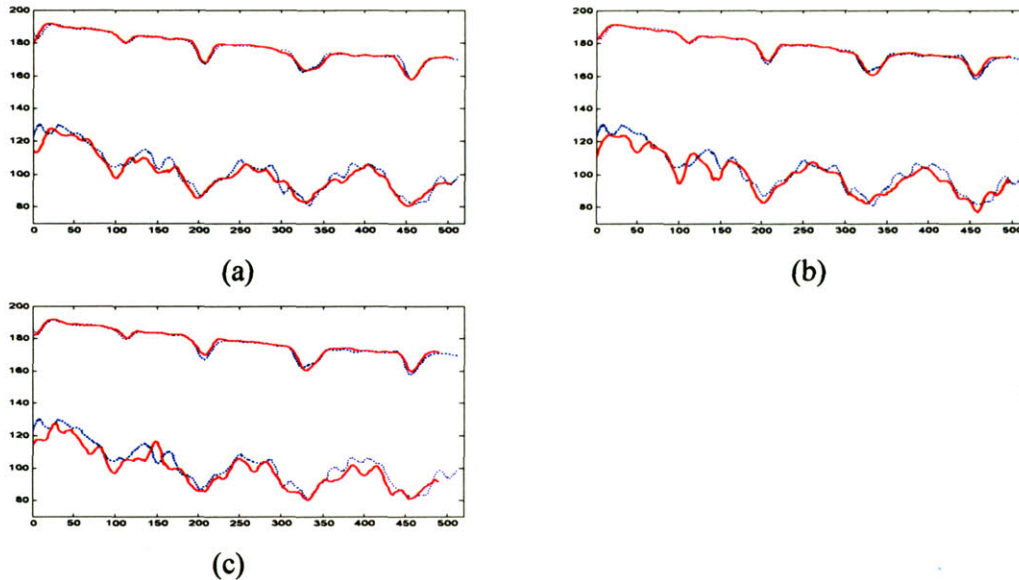
Figure 3-16. The profiles of the top skin surface and the inner boundary of the stratum corneum when the finger pad were indented at different levels: (a) 20 grams load (solid line) v.s. 10 grams load (dotted line) (b) 30 grams load (solid line) v.s. 10 grams load (dotted line) (c) 50 grams load (solid line) v.s. 10 grams load (dotted line). The values shown on the vertical and horizontal axes are pixel indices.

2. Radius of curvature = 7.8 mm

The finger pad was pressed against a plano-convex lens (Coherent Inc.) of focal length of 15mm, which implies a radius of curvature of 7.8 mm with a load 20gram initially, and then the load was increased by moving the finger pad toward the indentor. The OCT images were taken when the load was 20grams, 30grams, 50 grams, and 100 grams (Figure 3-17). The profiles of the skin surface and the inner boundary of the stratum corneum were outlined, smoothed with a fitted piecewise cubic curve, and shown in Figure 3-18.
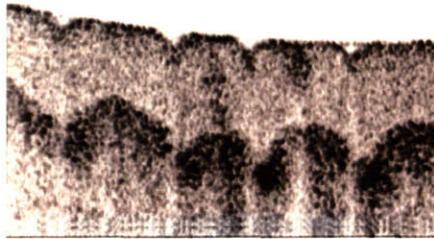
(a)
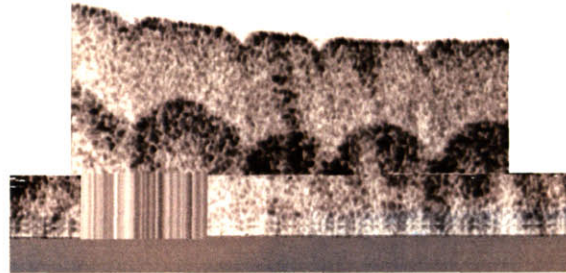
(b)
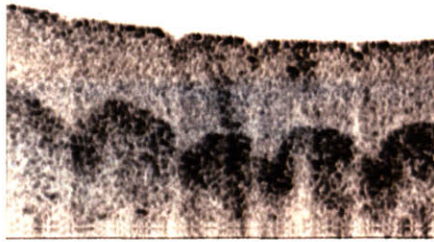
(c)
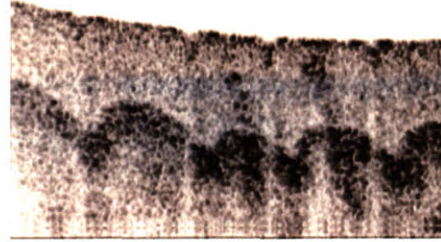
(d)

Figure 3-17. OCT images of the right index finger pad of an adult male subject. The real dimensions of each of the images are 1.21 mm (vertical) × 1.68 mm (horizontal). The finger pad was indented by (a) 20 grams load, (b) 30 grams load, (c) 50 grams load, and (d) 100 grams load.

(a)

(b)

(c)

(d)
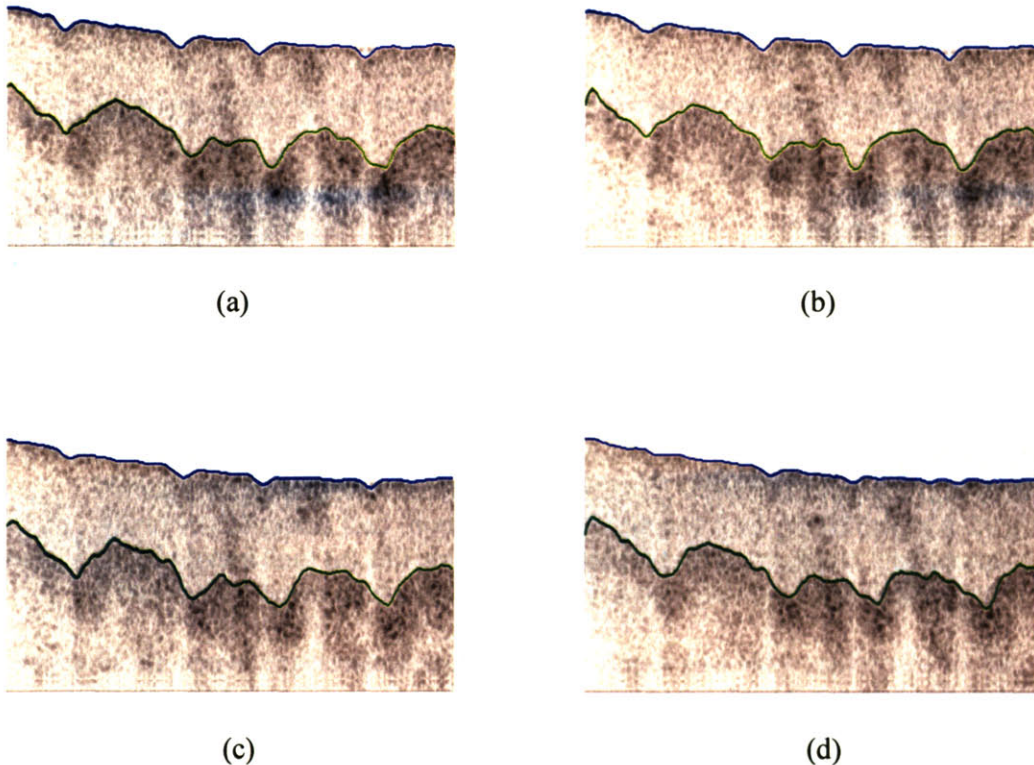
Figure 3-18. The profiles of the top skin surface and the inner boundary of the stratum corneum in the OCT images in Figure 3-17 were outlined. The real dimensions of each of the images are 1.21 mm (vertical) × 1.68 mm (horizontal). The finger pad was indented by (a) 20 grams load, (b) 30 grams load, (c) 50 grams load, and (d) 100 grams load.

To observe the effect of the indentation on the shape of finger pad area close to the indentor, all the profiles of the finger pad under loads higher than 20 grams were superimposed on the one under a load of 20 grams. As shown in Figure 3-19, the dotted curve shows the profile of the finger pad when indented by 20 grams, and the solid curve shows the profile at indentation load of 30 grams, 50grams, and 100 grams, respectively.
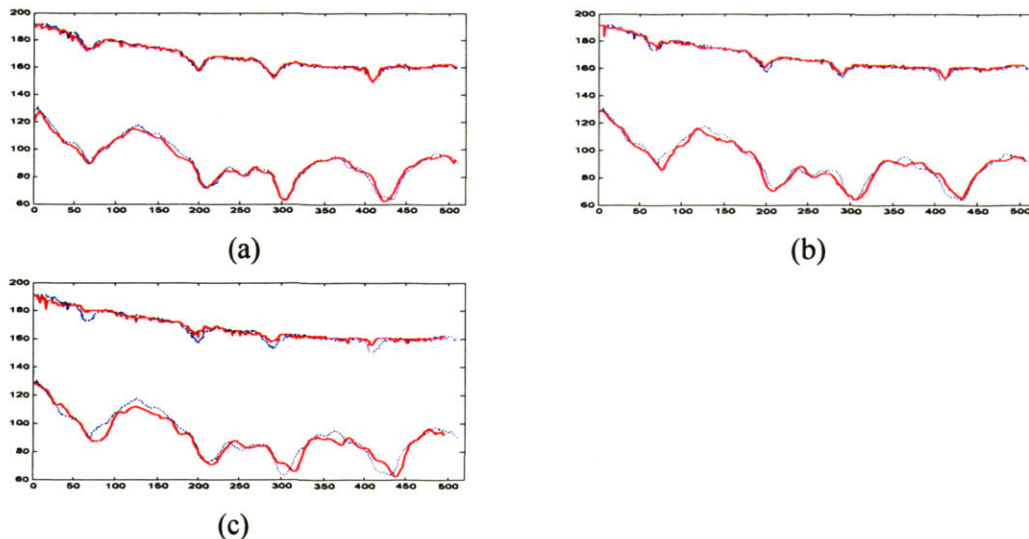
Figure 3-19. The profiles of the top skin surface and the inner boundary of the stratum corneum when a finger pad were indented with different loads: (a) 30 grams load (solid line) v.s. 20 grams load (dotted line) (b) 50 grams load (solid line) v.s. 20 grams load (dotted line) (c) 100 grams load (solid line) v.s. 20 grams load (dotted line). The values shown on the vertical and horizontal axes are pixel indices.

The images in the above experiments show that the finger pad skin conformed to the flat or curved indentor surface, with the ridges in contact with the indentor such that the contact region emerged rapidly even at very low loads, but changed very little as the load increased. The grooves on the skin surface shrank a little bit during the indentation, but no change in the thickness of the tissue layer between the surface and the inner papillae, that is, the stratum corneum, was observed. The likely reason is that the epidermis is much thinner than the dermis under it and the stiffness of the epidermis has been known to be several times higher than the dermis, so that most of the deformation occurs in the dermis region. This high stiffness in epidermis strengthens its function as a protective layer.

d. flat surface with a raised rectangular bar

A rectangular bar was cut from the glass wafer of thickness 0.53 mm to have a width of 0.44 mm. The glass bar was glued to a larger piece of glass wafer to act together as the indentor. The finger pad was moved toward the indentor at 0.50 mm steps. Figure 3-20 shows the images taken when the indentations were 1.0 mm, 1.5 mm, 2.0 mm, and 2.5 mm, Figure 3-21 shows the stratum cornum profiles outlined using the same methods described previously, and Figure 3-22

56

shows the comparison of the outlined profiles of the images at indentations of 1.5 mm, 2.0 mm, and 2.5 mm with the image at an indentation of 1.0 mm.

These images and the comparison of tissue boundaries show quite clearly the movement of the tissue boundaries. The higher the depth of indentation, which at the same time means the higher the load applied on the finger pad, the more the conformation of the finger pad to the shape of the indentor. Compared to the previous experiments, the images from this experiment with larger indentation increments show more clearly the evolution of the indented fingertip skin at this resolution and scale, and hence they are used later as biomechanical data for the validation of the finite element model of the fingertip (See Chapter 5).

(a)

(b)

(c)

(d)
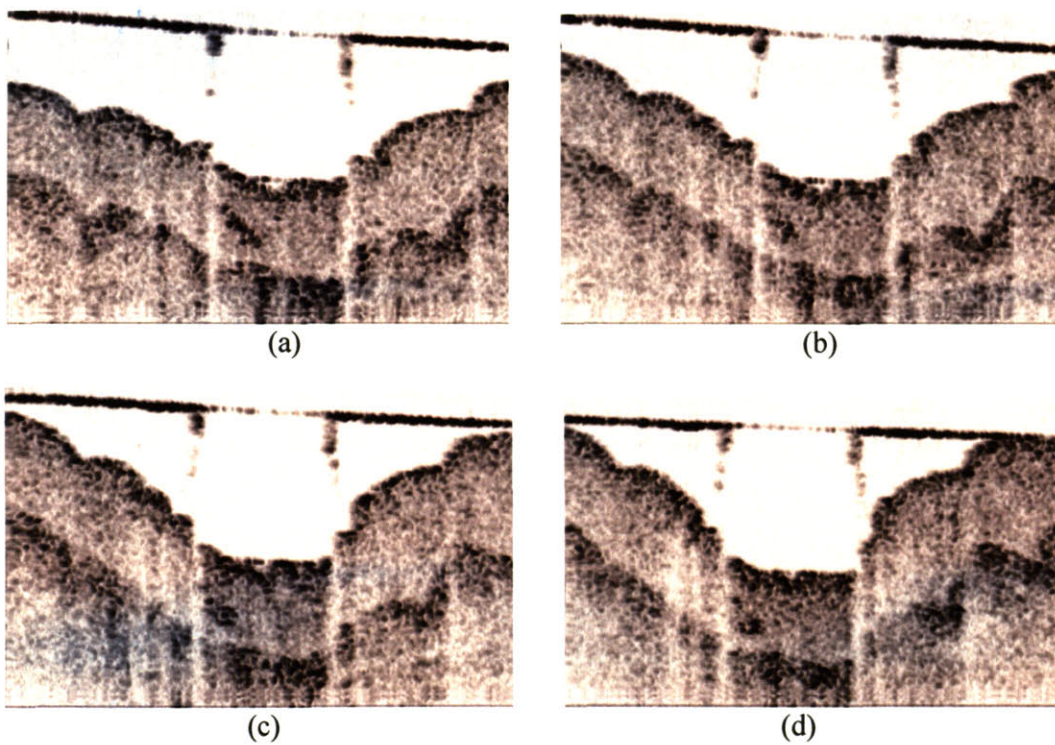
Figure 3-20. OCT images of the right index finger pad of an adult female subject when indented by a rectangular bar (h × w = 0.53 mm × 0.44 mm) on a flat plate. The real dimensions of each of the images are 1.05 mm (vertical) × 1.68 mm (horizontal). The finger pad was indented to a depth of (a) 1.0 mm, (b) 1.5 mm, (c) 2.0 mm, and (d) 2.5 mm.

(a)

(b)

(b)

(d)
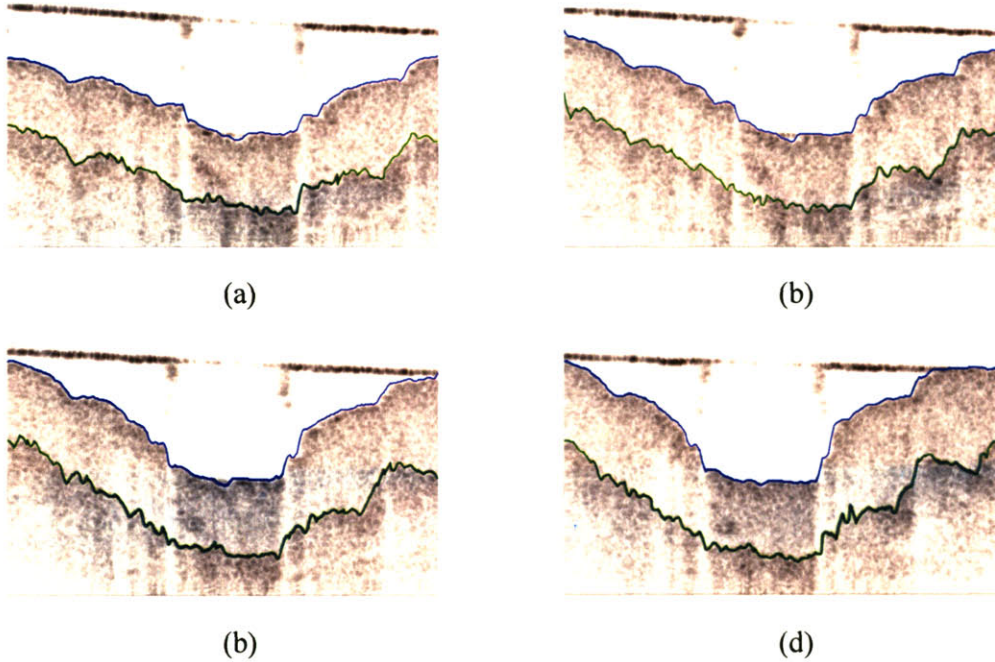
Figure 3-21. The profiles of the top skin surface and the inner boundary of the stratum corneum in the OCT images in Figure 3-20 were outlined. The real scale of the images is 1.05 mm (vertical) × 1.68 mm (horizontal). The finger pad was indented to a depth of (a) 1.0 mm, (b) 1.5 mm, (c) 2.0 mm, and (d) 2.5 mm.

(a)

(b)

(c)
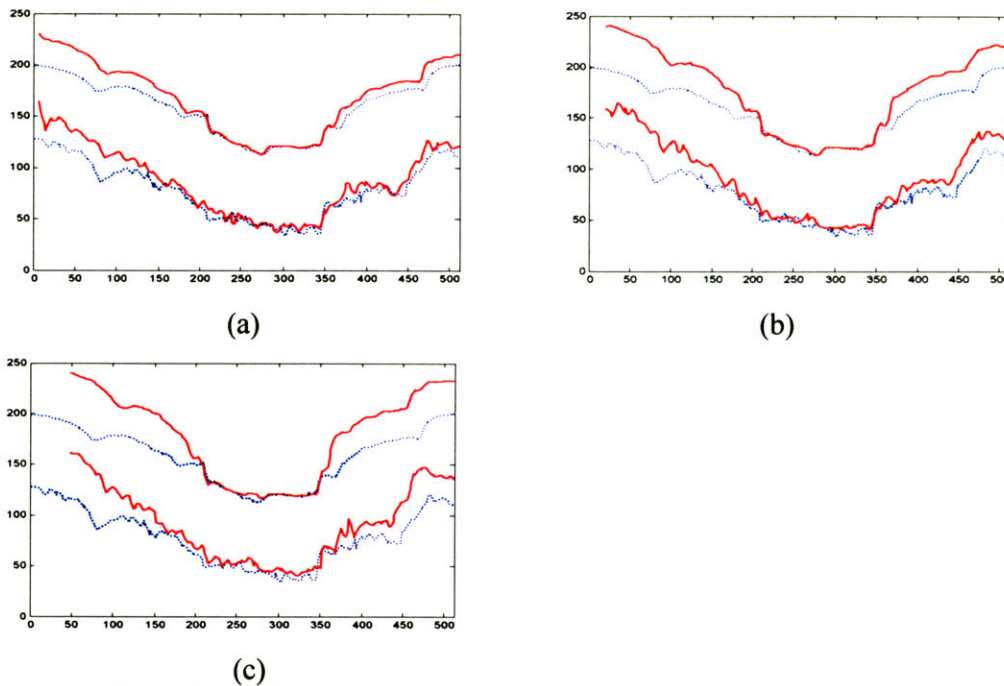
**Figure 3-22.** The profiles of the top skin surface and the inner boundary of the stratum corneum when the finger pad was indented by a rectangular bar at different levels: (a) 1.5 mm (solid line) v.s. 1.0 mm (dotted line) (b) 2.0 mm (solid line) v.s. 1.0 mm (dotted line) (c) 2.5 mm (solid line) v.s. 1.0 mm (dotted line). The values shown on the vertical and horizontal axes are pixel indices.

The experiments show that the OCT setup A was capable of imaging the stratum corneum, the eccrine glands in the stratum corneum, and part of the stratum malpighi beneath. The results have shown that when the human finger pad is indented by a flat or a smoothly curved surface, the skin surface can keep the contact region with the indentor fairly constant. Even at high loads, the grooves between the surface ridges were quite clear, which means that the ridges deform very little in bearing the load. And the stratum corneum (about 0.35 mm in thickness as measured from our images) is so stiff that even at this high resolution level (~10 micron), we could not observe variation in the deformation of that layer. More over the inner boundary of the stratum corneum remains approximately the same over increasing loads. This implies that most of the deformation must have occurred below the epidermis, that is, in the dermis and the subcutaneous fat. This high stiffness of this upper layer accounts for the protective function of the skin against mechanical loads. And in spite of the layer of high stiffness, skin as a whole is quite flexible when encountering smooth bump and/or sharp corner. Unfortunately in the experiment, the structure below the stratum corneum was obscured and we could not observe the location of the

mechanoreceptors. In order to see if we could image the mechanoreceptors when stratum corneum was removed, an experiment was conducted. Figure 3-23 showed the case, in which a female subject's right index finger was rubbed with coarse sandpaper (50 grit) for 3 minutes and then fine sandpaper (220 grit) for 4 minutes. The image showed that the thickness of the stratum corneum indeed decreased significantly after this sanding process. Unfortunately, however, the structure below it was still too unclear to be of value.

(a)   (b)
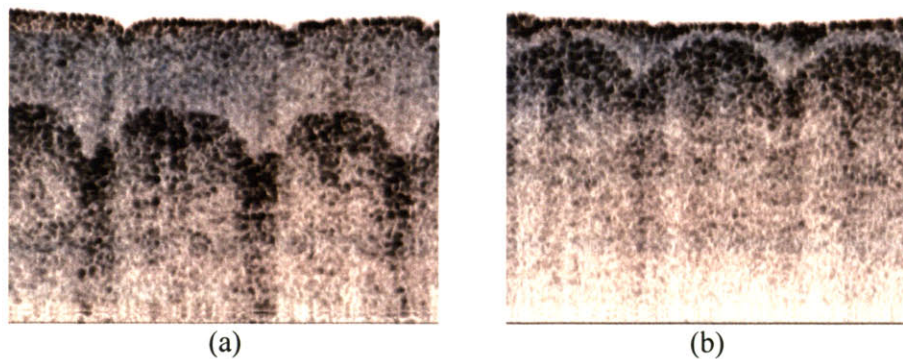
Figure 3-23. OCT image before ((a)) and after ((b)) rubbing the fingertip with sand paper (50 grit for 3 min and 220 grit for 4 min). The dimensions of each of the images are 1.04 mm (vertical) × 1.21 mm (horizontal).

To visualize the structure of layers below the stratum corneum better, OCT imaging setup B with higher resolution, as described in Section 3.1.1, was used. Figure 3-24 shows an OCT image of a female subject's index finger pad when pressed with a high force against the objective lens of this setup. As shown in this image, even though this setup limits the field of view to 0.9 mm (vertical) × 1.0 mm (horizontal), the image shows the structure below the stratum corneum significantly better than the previous OCT setup. And in the middle of the 0.9 mm vertical range in the image, several oval shaped structures can be seen. To identify and quantify the locations of these structures, boundary detection is necessary. And because this structure does not show up as a substantially horizontal layer, the method b mentioned in Section 3.3.2 was applied.
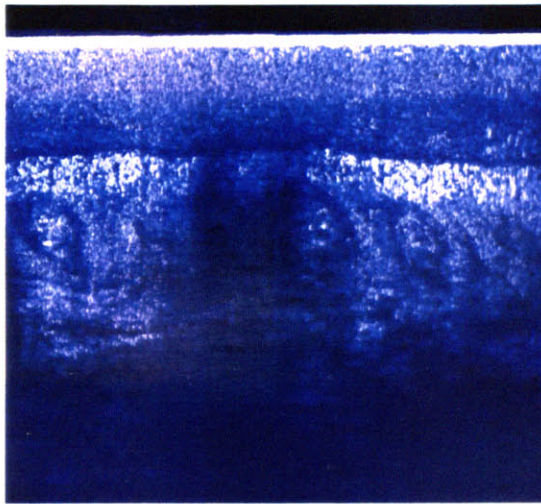
Figure 3-24. OCT image of the fingerpad of a female adult subject using SkinDex300. The real dimensions of the image are 0.9 mm (vertical) × 1.0 mm (horizontal).

Visual inspection of the image indicates that the three oval shaped structures in the image are visible due to the darker lines around them. To apply the snake model, the image force has to trap the contour to be locked onto the darker line, that is, to apply a constraint of minimum intensity. Therefore the term in the energy minimization equation (described in Section 3.3.2) to apply the image force is just the intensity $I(x,y)$. The term that gives rise to the external constraint forces was neglected. Instead, an algorithm was used so that the approximate position of the contour can be initially placed manually.

Using a similar algorithm as Voss and Srinivasan (1997), the code required the user to give as the input arguments the image file name, the total number of nodes on the boundary, the constant parameters α and β, which represent the flexibility and stiffness of the active contour respectively(as described in Section 3.3.2), a suggested step size for iteration, and the number of iteration for the contour to approach the boundary. Then the code displayed the image and prompted the user to pick by clicking the mouse the center and two points on the long the short axes of an ellipse to form the initial shape of the snake, and then the anchor spots for the snake to converge completely on the image. Figure 3-25 illustrates the process and the result using snake to outline the contour of the oval shaped structures. In this specific case, results were obtained from using a total of 40 nodes on the contour, an α value of 5.0, and a β value of 2. Two anchor points (shown as symbol *) were picked for each location and picked at the spots with the least smoothness (the top and bottom end of the oval). Using these two points as guides ensures that

61

the constraint to keep smoothness of contour in the internal energy term (the minimization of the first and second order differentials along the contour, as described previously) will not misdirect the iteration process. The contours shown in the Figure 3-25(b) fit pretty well with the expectation from direct visual observation and provide the outline of the oval shaped structures. Comparison with the microphotographs of the Meissner's corpuscles by Cauna (1954) reveals that these oval shaped structures are in the typical locations of the Meissner's corpuscles and that their size and shape are close to that of the Meissner's corpuscles. Therefore, we can conclude with a high degree of confidence that the observed oval structures are indeed Meissner's corpuscles which serve as the mechanoreceptive endings of rapidly adapting nerve fibers.
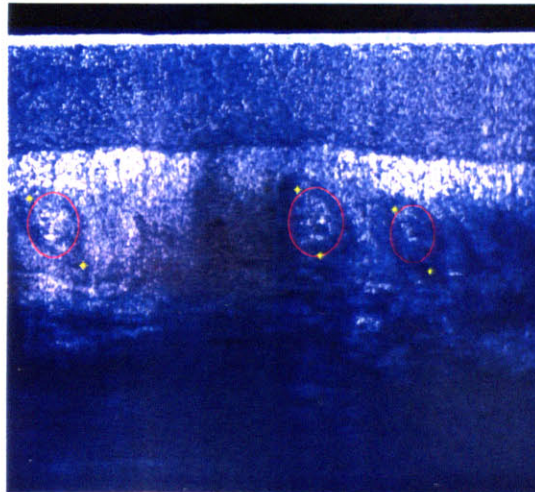
(a)
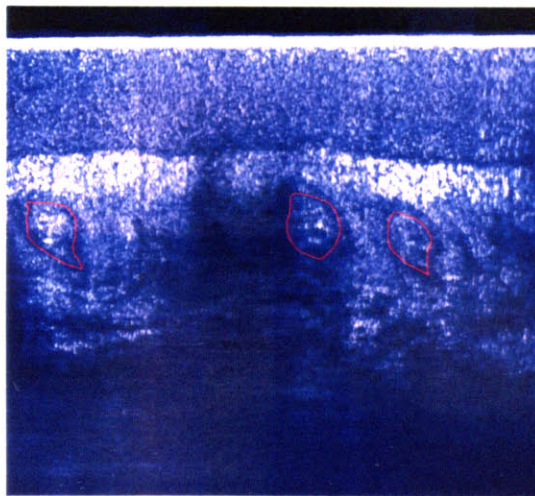
(b)

Figure 3-25. Ultrahigh resolution OCT image to show the potential locations of Meissner's corpuscles (shown in (a)) and the locations actually identified by using a snake program.

The images obtained show that OCT is a good tool to investigate the epidermis of the finger pad *in vivo* and shows quite clearly the surface ridges, sweat glands, and papillary dermal layer under the epidermis while most other imaging modality with lower resolution (eg. MRI, CT, and ultrasound) are unable to do so. In the experiments, the position of certain features, such as the

ridged layers, during indentation can be tracked using high resolution OCT images. And with our setup, maximum indentation depth and indentation load can be controlled or measured at the same time, so that these data can give insight into the mechanical properties of finger pad tissue. However, there are some imitations to the experiments. For example, the material composition of the indentors is limited to the ones with optical transparency, so that the laser light can pass through them without losing too much energy to form the needed interference pattern. Besides commercially available optical lenses, we have used microscope slides and glass wafers to make the indentors. The quality of the images with microscope slides and glass wafer as the indentor material has been pretty good. Another advantage of using microscope slides is because they are low priced, we can replace them very frequently to avoid any harm to the image quality due to possible scratches left on it after indentation. The penetration depth of a 1300 nm OCT setup to image fingertip skin is in the range of 1mm, so only a small "window" can be created to view the tissue, which covers only the epidermis and, at best, a small part of dermis. The surface feature on the indentor, such as the rectangular bar we used, is also limited to being smaller than 1mm in depth so as to cover both the indentor and the tissue in the same image. In spite of these limitations, the deformation information extracted from the tissue layers were used to improve the realism of the computational models, as described in Chapter 5.

Chapter 4
UBM Experiments

4.1 Equipment Setup

4.1.1 UBM Scan System

The fast-scan high-frequency ultrasound imaging system built by Raju and Srinivasan (1999, 2003) was used in experiments to determine the material properties of the superficial skin layers. Figure 4.1 shows a schematic of the setup and a picture of it. The system used in the following experiments consisted of a PVDF single element transducer (Model PI50, Panametrics Inc., Waltham, MA) which generates the acoustic waves and collects the backscattered echoes, a motorized scanning system (Compumotor/Parker-Hannifin, Cleveland, OH) to position the transducer or mechanically scan over the tissue to collect echo signals from various locations, a pulser/receiver (Panametrics, Model PR5900) to excite the transducer, a high-speed A2D board (Gage Applied Sciences, Montreal, Canada; Model CompuScope 8500) to collect the backscattered echoes, and a PC to control the various elements. With a diameter of 6.35 mm, the transducer has an f-number of 2 and a focal length of 12.7 mm. And at an energy setting of 32 μJ on the Panametrics pulser, the transducer pulse-echo spectrum has a center frequency of 28 MHz and a bandwidth (-6 dB) of 30 MHz, which can result in axial resolution of 25um, and lateral resolution of 107 μm.
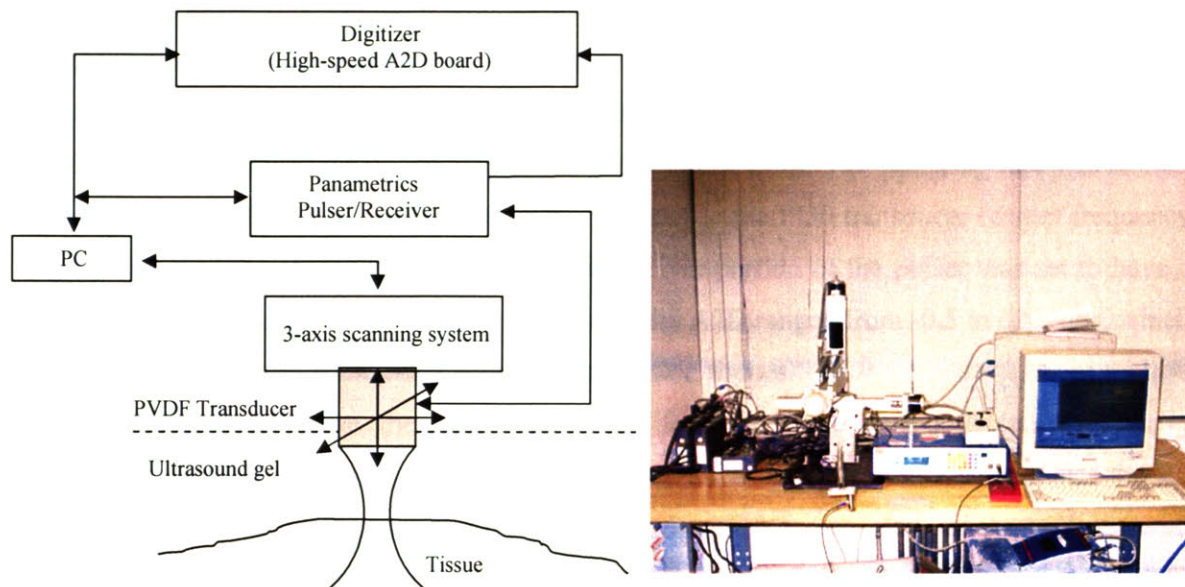
Figure 4-1. Schematic and a picture of the UBM system built in the Touch Lab, MIT.

The scanning system is a 3-axis stage that has precision grade slide assemblies for each of the axes (Parker Hannafin, model number 402006LNMP). The total travel length is 6 inches on each of the axes, and the positioning accuracy and repeatability are 12 μm and 2 μm over the total travel length. Motors (Model number Zeta 57-51) attached to the three axes were powered using micro-stepping drives (Model number Zeta4). The drivers were controlled by a 4-axis controller (Model AT6400), which received commands from the PC through an ISA interface card. Custom programs were developed in a Visual C++ environment to facilitate computer control. The transducer was attached to the scanning system using a custom machined bracket. A joystick was used to facilitate initial positioning of the transducer at the start of the experiment. In order to comply with the electrical safety requirements, medical grade isolation transformers (Dale Technology Inc., Thornwood; Model IT 1100) to reduce ground loop currents were added to the system.

When collecting the depth information data from the tissue, the ultrasonic waves are focused towards the tissue being investigated. The tissue is applied with a layer of ultrasound gel, as the acoustic impedance of the transducer matches that of gel, thus eliminating any unwanted reflections as the wave leaves the transducer. The waves are reflected from several depths from within the tissue. The same transducer converts the reflected echoes back to electrical signals, which are then sent to a receiver unit, which is also housed inside the pulser unit. The receiving

electronics consists of a bandpass filter whose upper and lower frequency cutoffs can be varied, an attenuator, and an amplifier whose gain ratios can be varied so as to fit the voltage range of the A2D board. The A2D board is capable of transferring data from its on-board memory to the PC's memory at rates of up to 100 Mbytes/sec using the PCI bus. The sampling rate was chosen to be 500 MHz, which was sufficient to record echoes for the PI50 transducer (center frequency ~ 28 MHz), and the analog filter setting on the receiver portion of the pulser was set to have a low pass cut off of 100 MHz. The vertical range on the A2D ranged from -0.5 to 0.5 volts, which was sufficient to record backscatter echoes from the skin tissues.

For creating a UBM image, the backscattered data from the tissue were collected periodically and transferred to the PC's memory while the transducer was in continuous motion. Once the RF data were collected, B-scan images were created by detecting the envelope of the backscattered echoes from different parts of the tissues using the Hilbert-transform approach (Bracewell, 2000) and mapping the envelope into gray levels for display. The attenuation along the depth is compensated assuming the wave decays exponentially with distance (Leeman, 1984). Custom-written programs in MATLAB (The MathWorks, Inc., Natick, MA) were used for generating and displaying the images.

4.1.2 Indentation Stage

An indentation system was added to the above UBM system for strain imaging. This indentation stage consisted of a manually controlled high precision vertical translation stage (Model M-MVN80, Newport Co., Irvine, CA) and a pair of custom indentor holders. The configuration is shown in Figure 4-2. The material to be tested (human finger or ultrasonic phantom) is placed on top of the translation stage with a piece of acrylic plate placed on top of it. With a dimension of 96 mm × 25 mm × 4.8 mm (Figure 4-3), this indentor has a vertical through slit. The width of the slit (2mm) was larger than the ultrasound beamwidth, while the length (10 mm) was larger than the translation range of the transducer during image scanning, thereby ensuring that the ultrasound beam would not be blocked by the indentor. A piece of transparency sheet (3M, St. Paul, MN) was glued to the bottom of the indentor to allow most of the acoustic power to pass though while keeping a flat surface in contact with the sample to control the amount of the indentation. Highly conductive ultrasound gel (Chattanooga Group, Hixson, TN) was applied between the indentor top surface and the transducer head and inside the slit of the indentor to

67

ensure a good coupling. When the finger or phantom is elevated by the stage, the indentor is pressed up against the two indentor holders through a pair of load cells (Model 31 and SC1000, Sensotec, Columbus, OH). This enables the load applied to the sample to be measured, which is transferred to the PC. The total load at any moment is the sum of the readings from both load cells and the weight of the indentor. The load due to the ultrasound gel was found to be negligible. Two small round dimples were made at the two ends of indentor corresponding to the two spots in contact with the load cells, so that the indentor would not slip away during the indentation process.
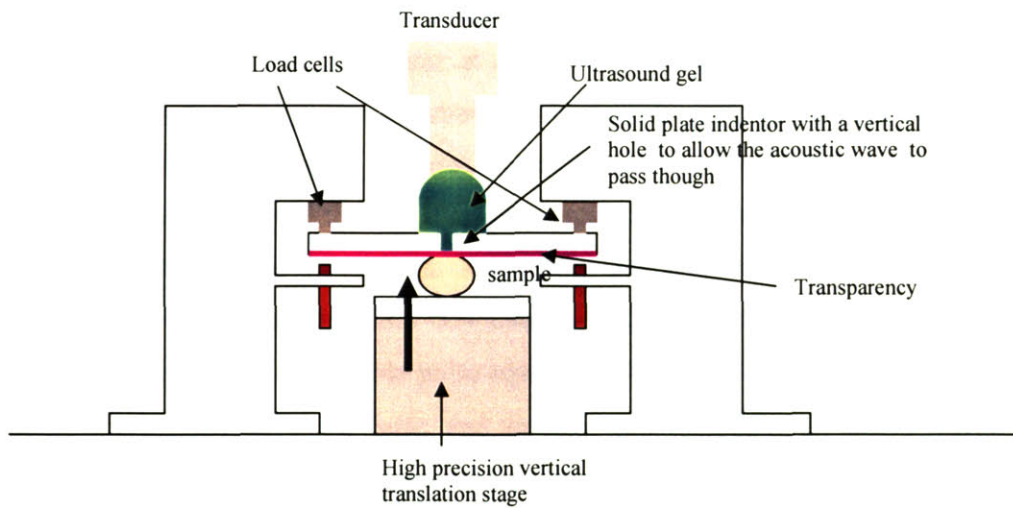
Figure 4-2. The configuration of the indentation stage used in UBM system.
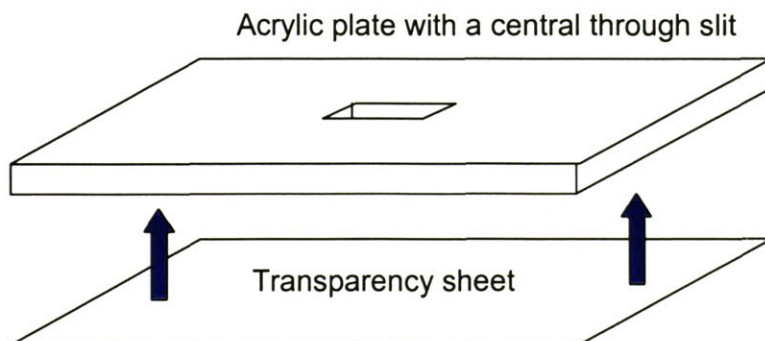
Figure 4-3. The indentor was made of acrylic, with a slit at the center and a piece of transparency attached to its bottom side.

4.2 Experimental Method and Procedure

The general principle of strain imaging is first to track the tissue deformation due to applied external force in order to determine the associated strain fields. Normally imaging data were taken before and after compression of the tissue, and then cross-correlation was calculated along individual A-lines to search in the time-domain, the corresponding spots in the images that result in the best correlation. To avoid the mismatch of the A-lines pre- and post-compression due to the motion error of the translation stage, and the unwanted movement of the human finger, it was assumed that the small region of interest on top of the fingerpad for investigating the stiffness variation could be viewed as a semi-infinite layered structure, where the distribution of stiffness through the skin thickness is about the same at any lateral location on the skin surface. This assumption, supported by the general structure of the human skin, essentially reduces this problem to a 1D one where only single A-line at the center of the region needs to be recorded for strain analysis. In order to improve the signal-to-noise ratio (SNR), a single A-line was taken to be the average of 50 repeated RF echoes. Averaging was done in software once all the independent waveforms were acquired and downloaded to the PC's memory. With the energy setting of 32 µJ, the maximum admissible pulse repetition frequency (PRF) of the pulser is 10 kHz, or 100 µs interval between pulse trains, and the total time to acquire all the 50 waveforms was 5 msec. Thus the duration of each experiment mainly depended on the time taken to apply the indentation, which was about 3 sec.

(Fixing the sample & focus adjustment)

Program starts

Acquisition of one A-line of
US signal (pre-compression)

A prompt to ask the experimenter to
indent the sample by raising the
vertical translation stage

Acquisition of load data
while increasing indentation

If multiple
compression

Acquisition of one A-line o
US signal (post-compression)

Image scanning for
5mm laterally

Program ends

Figure 4-4. PC controlled experimental process.

The experimental process (shown in Figure 4-4) was controlled by a Visual C++ program. The program was started after the human finger or phantom was fixed on top of the vertical translation stage, ultrasound gel was applied above the indentor plate, inside the slot, and below the indentor as the coupling medium between the transducer and the tissue to improve the passage of the ultrasound beam, and the position of the transducer was manually tuned with a joystick to focus on the desired depth of the sample. Initial set of RF data was first taken as "the pre-compression", then a beep sounded followed by a time delay of 3 sec to prompt the experimenter to manually elevate the stage so the sample was pressed up against the indentor, during which data from the load cells were recorded. The load data was later reviewed to confirm that load increased normally with indentation. Then another set of RF data was taken as "the post-compression". The experimenter specified the desired number of indentation steps at the start of the process if multiple indentation was desired, so that a technique of multi-compression with smaller indentation steps could be applied and the deformation of the sample at multiple steps was summed to improve SNR. Several preliminary studies showed that an

indentation step of 0.125 mm gave the best cross-correlation results for most human fingers, so single step indentations with this step size was used for the experiments.

A B-scan image was recorded after all the indentation steps. This image was viewed afterwards to confirm the sample was focused as expected and used to locate the top surface of the sample in the data analysis. In the image scanning, the lateral spacing between the echo lines was chosen to be 25 μm, which was less than half of the lateral resolution of the system of 107 μm. The scanning speed was chosen to be 2 mm/sec, and the number of echoes for averaging was chosen to be 50. During this time period of 5 msec to acquire the 50 waveforms, the transducer moved by a distance of 10 μm, which was 9.3% of the lateral resolution. Thus, the chosen set of system parameters ensured that all the 50 waveforms used in averaging were acquired from approximately the same lateral location of the tissue. For the above scanning speed, the system would be ready to collect the next echo line by the time the transducer moved to the next location 25 μm away. The field-of-view was 4.5mm in the axial direction, and 5 mm in the lateral direction. The total imaging time for the scan length of 5 mm was only about 2.5 seconds.

All the pre- and post- compression single A-line data, load data, and image data were post-processed with custom-written programs in MATLAB. The speed of sound within the tissue was assumed to be 1.5 mm/μs for calculating the depth information (Moran et al, 1995). The data at continuous indentation steps were cross-correlated to calculate the displacement at different spots along the depth. The de-correlation at certain regions was resolved by removing the data points with lower correlation coefficients, and curve fitting was applied to overcome the lack of resolution due to sampling.

4.2.1 Experiments on a phantom

A homogeneous phantom was made by mixing 25% by weight of gelatin powder (Type A, G-2625, Sigma-Aldrich Co., Louis, MO), 2% by weight of polymethacrylate beads (Polysciences, Inc., Warrington, PA) with a mean size of 200 μm as the scattering centers, and deionized water. The phantom was made into a disc shape using a suitable mold with a diameter of 22.5 mm and a thickness of 9 mm. The material added was a little bit more than the exact volume of the mold thus formed a dome shaped top surface. After stirring it to make it mix well, a flat plate was carefully put on top of the mold and squeeze out the extra material to keep a flat top surface without air bubbles inside. The solution was then quickly placed in a refrigerator to accelerate its

solidification to avoid settling of the scatterers. When conducting the experiment, the phantom was removed from the mold and placed within a shallow round pit with a diameter 22.5 mm (same as the phantom) and a depth of 1.6 mm on top of the vertical translation stage. This pit was to restrict the phantom from slipping during indentation. The experiment was conducted under room temperature.

4.2.2 Experiments on human fingers

Data for strain analysis were collected from the index finger of human volunteers. Efforts were undertaken to limit subject movements during the experiments. The dorsal side of the index finger was attached to the top surface of the manually controlled vertical translation stage using a double stick tape and multiple straps were used to keep the finger steady. All the experiments were conducted under room temperature. All the subjects who participated in the study signed informed consent documents approved by the Institutional Review Board of MIT.

4.3 Postprocessing

4.3.1 Image data

A code for locating the top surface of the sample displayed the UBM image collected at the final step of the experiment (see Section 4.2) and prompted the experimenter to manually click on the position of the top surface of the tissue along a vertical line drawn in the middle of the image. The vertical coordinate of the chosen point was then recorded and would be used in deciding the depth within the tissue. Any RF data obtained from locations above this position (or before this time spot in the time domain) was not from the tissue and would be removed from the final strain calculation.

4.3.2 Single A-line data

An average of 50 raw backscatter signals, with each containing 1200 sampling points, was used for analysis. Time domain cross-correlation was calculated with a kernel size of 21 data points between the pair of RF data pre- and post compression to search for the spots in the post-compression data showing the best correlation with the given spots on the pre-compression data. The distance (in sampling units) of the pair of corresponding spots provided an estimate of the axial displacement of individual region at sampling precision, and the cross-correlation

coefficients of the data points around the best-matched spots were obtained. This kernel search had a resolution of 1 sampling point, or 3.75 μm. The displacement data points lying too far away from the others and/or with lower maximum cross-correlation coefficients were removed. To overcome the resolution limit due to sampling, a cubic curve fitting was done on the 3 data points around the point with the maximum correlation coefficient and the peak position of the curve replaced the original best correlated data point at the sampling precision as the "refined" data point. Finally the data points obtained from outside the region of tissue (see 4.3.1) were removed and curve fitting was done to the rest of the data to model the displacement profile as a function of location depth. The slope of this curve was computed and taken to be the axial strain within that region. Custom-written programs in MATLAB were used for the above analysis.

4.4 Experimental Results

4.4.1 Results from experiments with the phantom

Figure 4-5 shows the UBM image of the phantom on the left and the raw data of the displacement distribution at sampling precision on the right. The UBM image has a field of view of 4.5 mm (axial) × 5 mm (lateral). The bright band at the top of the UBM image is the transparency sheet, which appears thicker than its real size because the difference in the speed of sound within the transparency material and within the phantom was not accounted for in generating the image. The axial displacement plot on the right is obtained from the analysis of the pair of averaged A-lines pre- and post-compression and the two vertical straight lines in the depth range of 0 - 1 mm indicate the top and bottom surfaces of the transparency. This plot shows some degradation of the data at the deeper region due to attenuation of the signal along the depth.

Figure 4-5(c) is a plot of the axial displacement distribution after the data points with correlation coefficients less than 0.89 and the outlaying points were removed, and cubic curve fitting of the three cross-correlation coefficients around the sampling point with the highest cross-correlation coefficient was done to estimate the sub-sample location with the best correlation. A straight line with a slope of 0.014 shown in the plot fitted this data quite well. The figure shows that for this homogeneous phantom, the axial strain is globally uniform with a value of 0.014 in the depth range of 0 - 3.5 mm. This value can be verified by dividing the indentation size of 0.125 mm by

the original phantom thickness of 9 mm. Notice the axial displacement plots all use "pixel", or the sampling unit, as the unit of displacement, with 1-pixel corresponding to 3.75 μm.

(a)   (b)

(c)
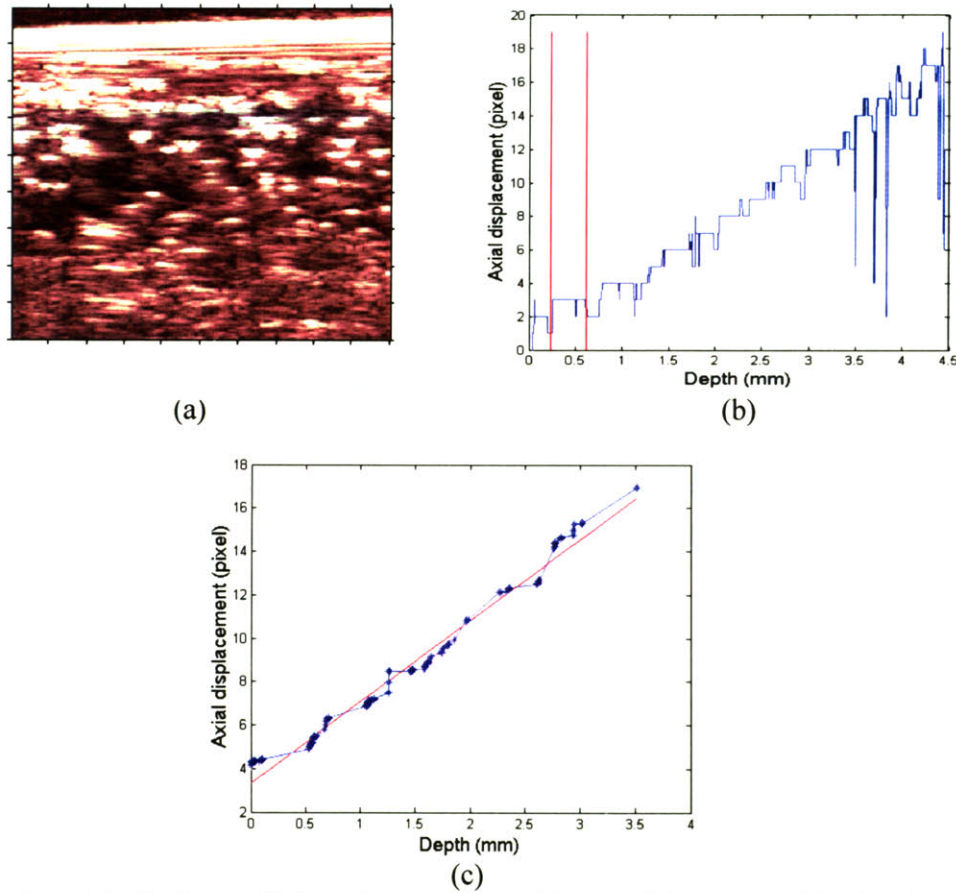
Figure 4-5. A UBM image ((a)) and a rough (sampling precision) plot of the displacement distribution along the depth of the phantom ((b)). The distance between the markers on the axes of the UBM image is 0.5 mm. (c) The axial displacement data from the phantom fitted with a straight line.

4.4.2 Results from experiments on human fingers

Imaging and analysis results from three subjects are shown in Figures 4-6, 4-7 and 4-8. Figure 4-6 shows a UBM image ((a)) of the fingerpad skin of a female subject aged 18 and axial displacement distribution along the depth at the center at the sampling precision ((b)). The indentation step was 0.125 mm. Beneath the transparency on the UBM image, which appears as a thick bright band, the echo rich region represented the strong reflection of ultrasound signal

from the fingerprints and stratum corneum. Since the primary tissue-wave interaction mechanism responsible for backscattered echoes is diffuse backscattering, the backscattered echoes depend on the size, shape, material properties, and number density of scatterers distributed in the tissue. These scatterers are basically discontinuities in the acoustical properties in the tissue and in the case of skin, they could be collagen fibers in the dermis, keratinocyte cells in the epidermis, groups of cells or fibers, sub-cellular components or sub-fibrous components.

It can be seen that the quality of this plot is worse than that from the phantom. This decorrelation can be due to: 1) movement of the fingertip during the process: for this high resolution data collection, even normal human breath or pulse can bring about enough movement to contribute to the decorrelation. 2) weaker scattering from the tissue within the skin: the scattering due to tissue/cell heterogeneity is weaker than the phantom with added scatterers, and the subcutaneous fat distributed below the epidermis is hypoechoic. 3) lower SNR at deeper region in the skin due to larger attenuation along the depth than the gelatin phantom. Figure 4-6(c) shows the processed data of axial displacement with two fitted straight lines. The axial strain, which is the spatial differential, or the slope of the displacement curves, is about 0.0042 till a depth of 1 mm and 0.0343 below that. That is a difference of more than eight times.
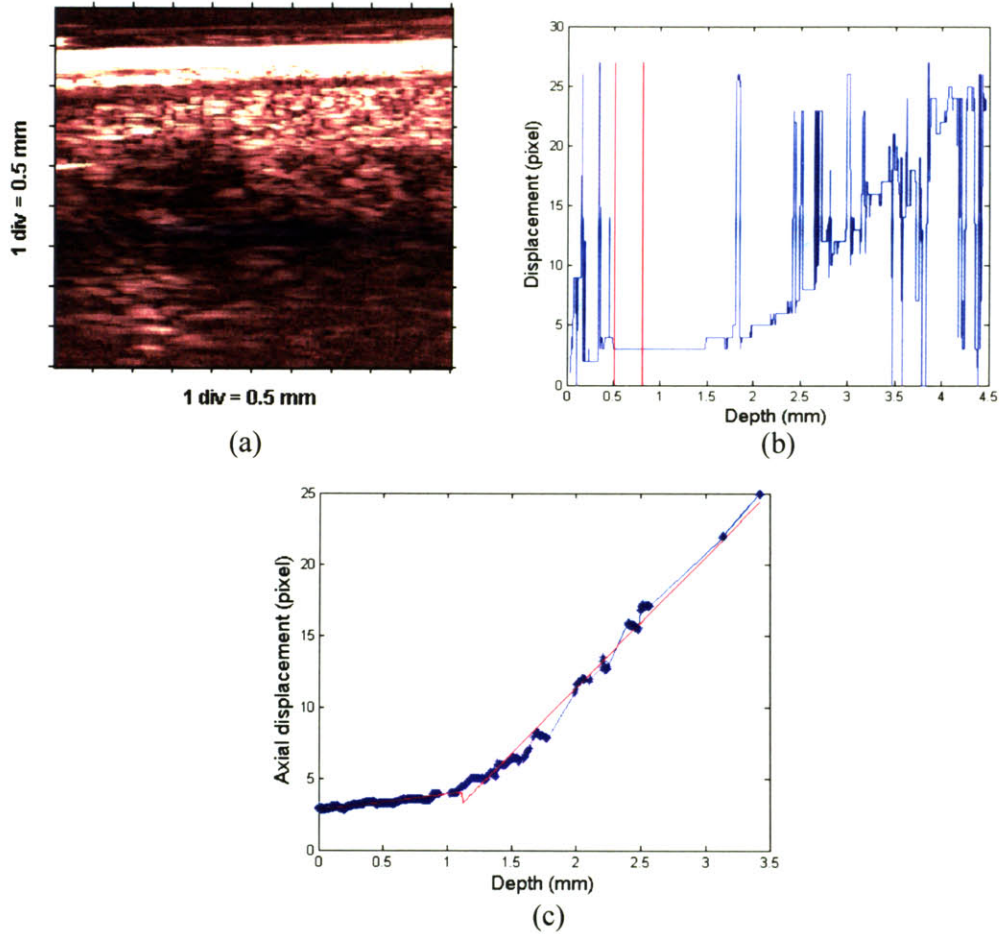
Figure 4-6. A UBM image ((a)) and a rough (sampling precision) plot of the displacement distribution along the depth of the finger pad of a female subject aged 18 ((b)). The distance between the markers on the axes of the UBM image is 0.5 mm. (c) The axial displacement data of the finger pad and its two fitted straight lines.

Figure 4-7(a) shows a UBM image of the fingerpad of a male subject aged 33 and Figure 4-7(b) is a plot of its axial displacement distribution at the sampling precision along the depth at an indentation step of 0.125 mm. Figure 4-7 (c) shows the processed axial displacement data, and two straight lines fitted to this distribution with slopes 0.0065 and 0.0262, implying that the strain changes to about one fourth in the deeper region. In the processing, the decorrelated data points, which were removed, were those with the sum of correlation coefficients less than 0.8.

(a)   (b)

(c)
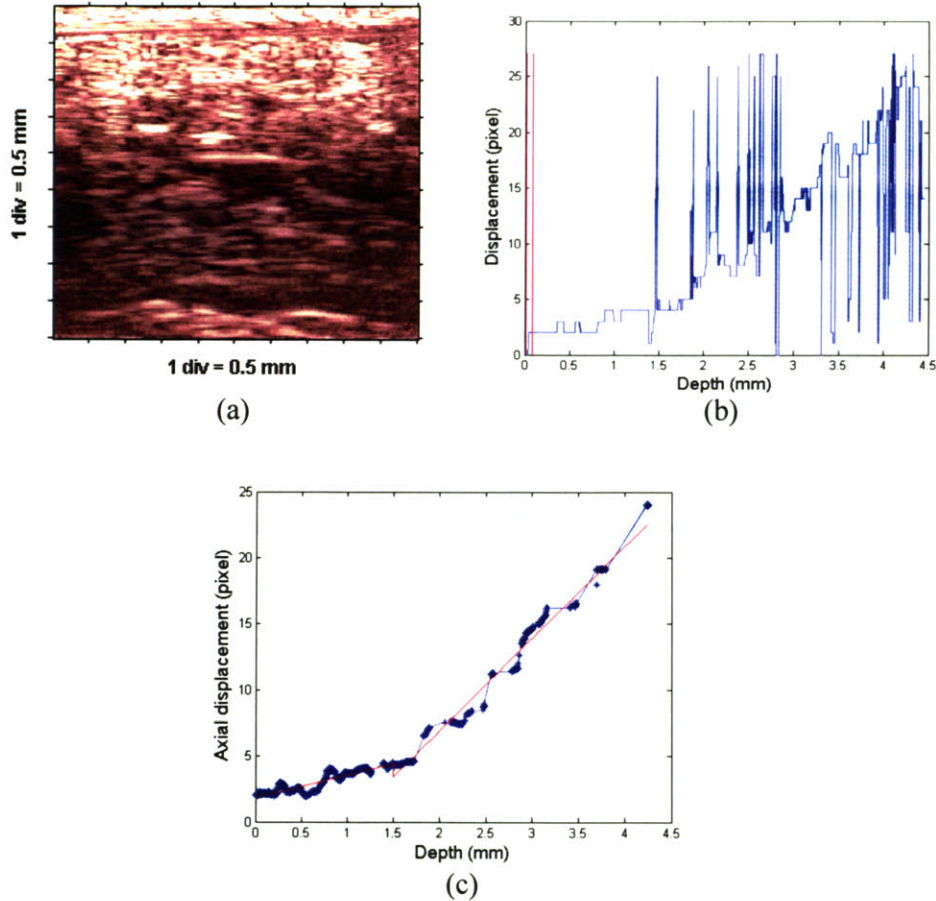
Figure 4-7. A UBM image ((a)) and a rough (sampling precision) plot of the displacement distribution along the depth of the finger pad of a male subject aged 33 ((b)). The distance between the markers on the axes of the UBM image is 0.5 mm. (c) The axial displacement data of the finger pad with two fitted straight lines.

Figure 4-8(a) shows a UBM image of the fingerpad of a female subject aged 45 and Figure 4-8(b) is a plot of its axial displacement distribution at sampling precision along the depth for an indentation step of 0.125 mm. Figure 4-8 (c) shows the processed axial displacement data, and two straight lines fitted to this distribution with slopes 0.0052 and 0.0347. The axial strain thus shows an increase of 6.7 times from epidermis to dermis which represents a stiffness difference between the dermis and epidermis. It can be seen from the UBM image that the signal is much weaker in the deeper tissue and from Figure 4-8(c) that lesser number data points were captured beyond the depth of 1 mm, which could be due to the hypoechoicity of the subcutaneous fat.

77

(a)

(b)

(c)
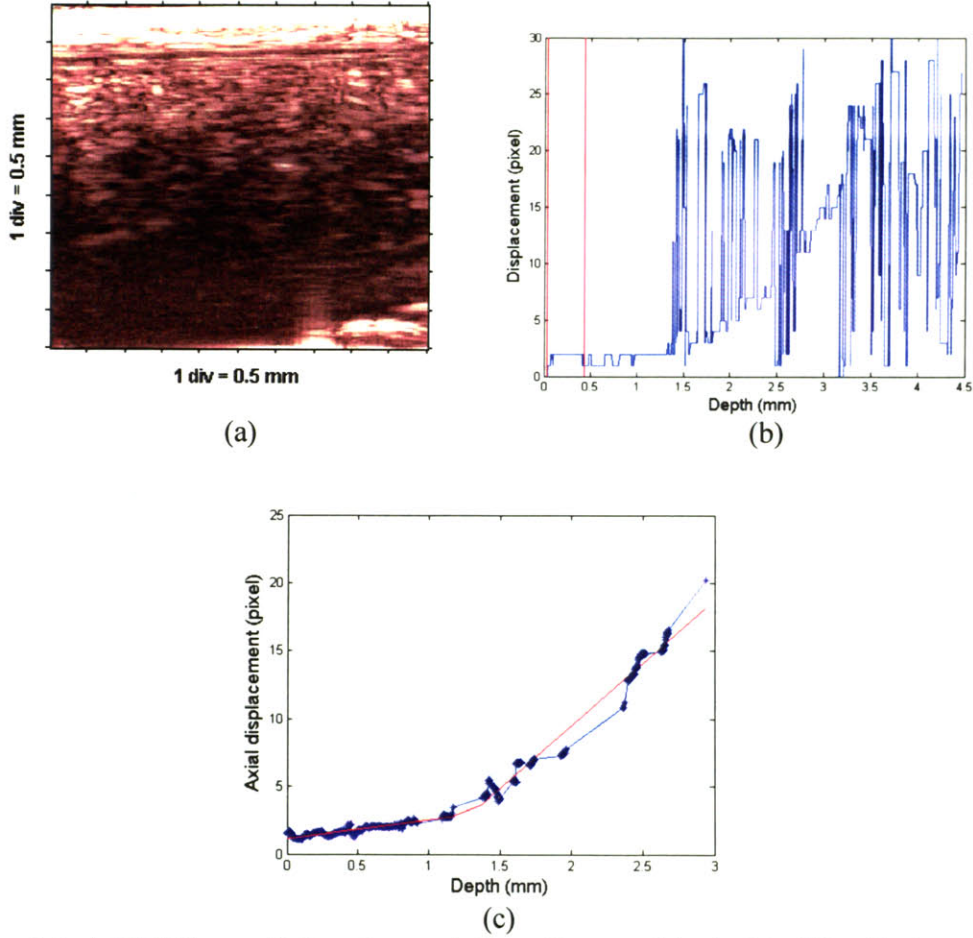
Figure 4-8. A UBM image ((a)) and a rough (sampling precision) plot of the displacement distribution along the depth of the finger pad of a female subject aged 45 ((b)). The distance between the markers on the axes of the UBM image is 0.5mm. (c) The axial displacement data of the finger pad with two fitted straight lines.

Compared to the results for the homogenous phantom, for which the axial deformation along the depth could be approximated by a single linear fit, the finger pad skin exhibited more salient variation of strain along the depth, with higher strain at deeper regions within the 3 - 4.5 mm depth that could be imaged. This matches the knowledge of skin structure well that the epidermis, extending to a depth about 0.5 - 1 mm of the palmar side of the finger, has higher stiffness than the dermis and fat below it. If this single "line" of tissue along the depth can be approximated as springs with different spring coefficients connected in series, the stress is the same everywhere along the depth, and then the strain variation can be viewed as the inverse of the axial stiffness variation.

Ten human subjects were tested for ten times each and their results of the axial strain ratio are listed in Table 4-1. The grand mean of all the data was 6.6, with a grand standard deviation of 2.2. The maximum standard deviation for a single subject is 3.1 and the minimum is 1.4. So it can be seen that there was large variation in the result, even within the subjects. And there was no clear correlation between the result and the individual subject or the compression load. The mean value of 6.6 will be used as the stiffness ratio of the dermis and epidermis in the model developed in Chapter 5.

Subject #	Axial strain ratio (dermis/epidermis) in10 trials	Mean	Standard Deviation
1	8.77 3.37 6.48 10.70 11.59 3.86 5.47 5.13 5.18 4.68	6.52	2.86
2	6.00 4.07 8.24 5.05 7.53 5.56 6.18 8.35 5.70 5.46	6.21	1.40
3	6.83 2.77 3.20 5.99 7.13 7.24 9.10 6.35 7.32 9.80	6.57	2.22
4	7.80 5.00 9.63 4.63 5.71 8.18 7.16 4.96 4.60 9.32	6.70	1.96
5	5.10 5.35 12.41 7.82 5.93 6.96 7.04 5.27 5.38 7.06	6.83	2.18
6	8.18 3.74 4.06 11.73 4.04 6.86 6.40 2.90 11.50 6.44	6.59	3.12
7	4.44 5.76 7.24 4.86 7.02 5.05 6.71 8.51 7.78 4.95	6.23	1.41
8	10.67 4.54 3.40 3.81 3.88 7.40 8.10 10.04 6.37 6.57	6.48	2.60
9	4.67 7.50 9.13 7.56 9.21 3.42 5.33 6.31 9.70 4.95	6.78	2.17
10	9.55 5.35 6.48 11.57 6.30 5.84 7.11 6.13 6.00 4.34	6.87	2.13

Table 4-1. The experimental results of the axial strain ratio from ten subjects.

Chapter 5
Finite Element Modeling and Simulation

Until now no techniques exist to directly observe the stress and strain state inside the finger or measure with high resolution the load distributions on the surface of the finger. Finite element simulations provide a way to obtain both the stress and strain state inside the finger and the pressure distribution on the surface of the finger when an object is indented onto the finger. The results of these simulations can be used to study the relationship between the surface traction distribution or tensorial stress-strain measures and the shape of the object that indents the finger. In order to accurately model the contact of the fingertip with objects that have high curvatures or sharp edges, sufficiently close nodes would be necessary on the finger pad in the contact region so that the finger pad would be able to conform to the steep curvature of the indenting rigid body. In addition, a high mesh density at subsurface depths is needed to compute the subsurface strain measures without aliasing effects. Also higher resolution of the model improves the accuracy of the finite element simulation results. However, as the resolution of the model increases, the computational effort increases. For 3D finite element problems, the computational time increases at least as the square of the number of nodes. Thus it becomes necessary to optimize the resolution of the finite element mesh by using varying mesh densities throughout the model, with higher mesh density only near the region of contact. The contact region (defined as the region having non-zero load) is governed by the deformation of the fingertip, which, in turn, depends on the load distribution within the contact region whose extent is unknown. Therefore, simulations involving contact interactions are generally nonlinear, and need to be done iteratively i.e. the indentation is simulated incrementally. In the simulations that were performed, the stimulus shapes were considered rigid and frictionless. This chapter describes the development of a three dimensional finite element model of the human fingertip with the outer epidermal ridges and the inner dermal papillae, its use in simulations of contact with shaped objects, and the verification of the model through comparison of prediction of simulation with the experimentally observed data.

5.1 Structural Geometry

Before the development of the finite element model, a solid model has to be built. A solid model is a model of the geometry of the object consisting of geometrical primitives such as curves (bounded by two points), surfaces (bounded by four curves) and solids (bounded by six surfaces). A finite element model on the other hand contains elements and nodes, which are usually created after the solid model is defined. The first step in the development of the solid model is to obtain the geometry of the fingertip. Previously, the global external geometry of the fingertip has been determined from an experiment imaging a real human finger with videomicroscopy and was specified in the form of coordinates of points on the surface of the finger (Dandekar and Srinivasan, 1996). The geometry of the finite element model developed purely based this measured data was asymmetric and the simulation results from the model often contained irregularities that were just inherent artifacts due to the asymmetry. In order to eliminate these unwanted artifacts, the geometry of the model was modified by Zhou and Srinivasan (2002) by fitting into symmetric and smooth parametric curves. The detailed internal geometry is not easily available and was idealized by assuming that the finger contains layers of tissues, with each layer being a homogeneous material. The shape of the internal bone was calculated from X-Ray images of the primate fingertips.

Having developed the solid model, the next step is to develop the finite element model by filling the solid with elements. In all the soft tissue layers, for sufficient spatial resolution, a high mesh density is needed. The existent model described above was divided into 48 axial cross sections, forming 47 slices in the axial direction, and at each cross-section, 577 nodes were specified to form 48 sections in the circumferential direction, and 12 layers in the radial direction. The same number of elements is followed throughout the slices along the axis of the finger. The mesh resolution was highest in the pulp region where the finger would be in contact with objects and was lower in the other half portion of the finger, close to the nail region. This made it possible to choose high mesh density in the portion of the fingertip that would contact objects, and at the same time limited the total number of elements in the model. All the elements in the model were either 8 noded isoparametric elements or 6 noded wedged elements. The outmost layer is the epidermis layer; the second layer is the dermis; the third layer is the subcutaneous fat layer; and the center is the bone, which is considered rigid. Figures 5-1 and 5-2 show the shape and dimension of this model.

(a)   (b)
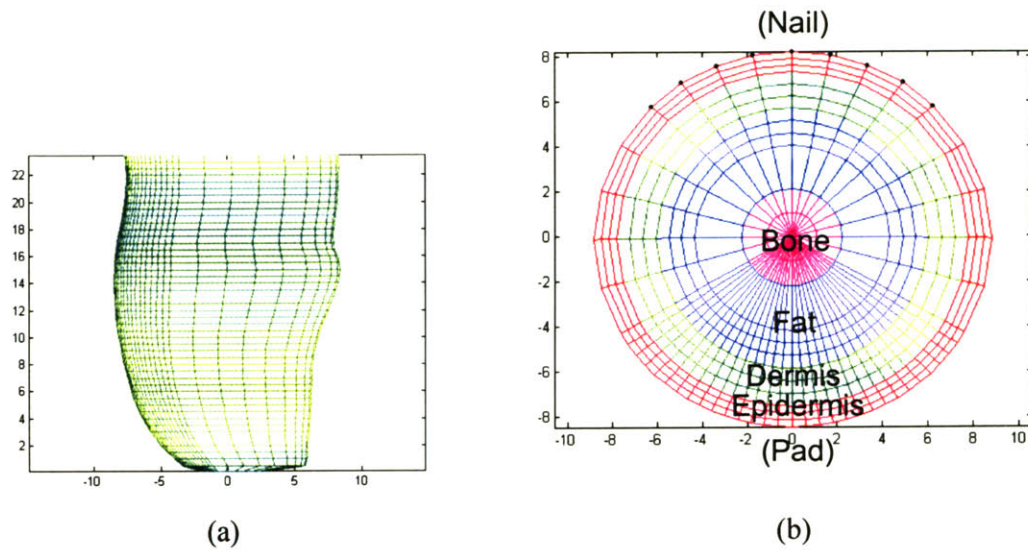
Figure 5-1. The 3D finite element fingertip model developed previously in the MIT Touch Lab. (a) the side view of the model with the finger pad facing left and the finger tip at the bottom. (b) the cross section perpendicular to the axis of the finger (cut at the vertical coordinate of 14 shown in (a)) showing different layers: the epidermis, the dermis, the subcutaneous fat, and the bone.

(a)   (b)

(c)   (d)
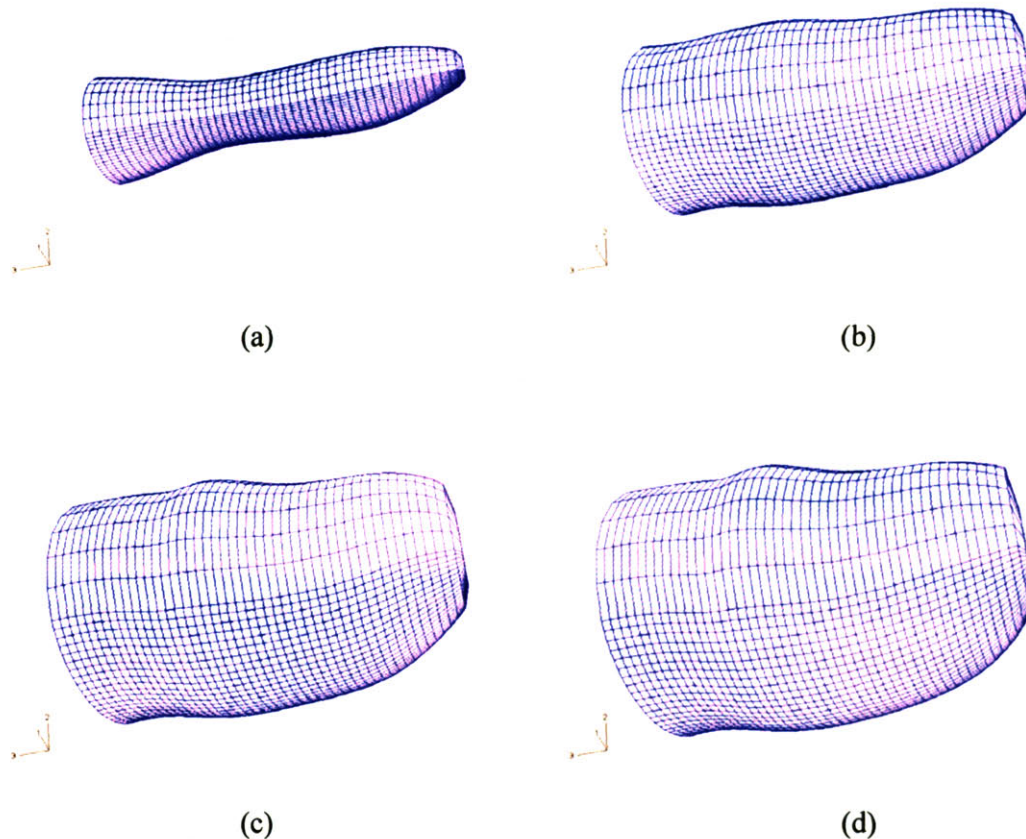
Figure 5-2. The 3D view of the human fingertip model developed previously in the MIT Touch
Lab showing the external shape of (a) the bone (b) the subcutaneous fat layer (c) the
dermis layer (d) the epidermis layer. The finger pad is facing down.

In the development of the new model, the general structure of this existent model described
above was kept, while the features within the skin tissue around the SA-I and RA
mechanoreceptors were added. It is known from earlier anatomical studies as well as from the
OCT images described earlier, that there exist a series of ridges between the stratum corneum
and the living epidermis as well as between the epidermis and dermis. The thickness of the
stratum corneum is around 350 μm, and the width of each epidermal ridge is about 400 μm. And
as Cauna described (1954), there are two types of mechanoreceptors structurally associated with
the papillary ridges – Meissner's corpuscles (RA) associated with the dermal papillae and
Merkel's discs (SA-I) associated with the intermediate ridges. The RAs are located inside the
dermal papillae immediately underneath the epidermis, while the SA-Is are at the end of the

intermediate ridges. In order to able to model these structures in detail, higher resolution than the existent model is needed. Higher resolution of the mesh on the surface will be useful not only in capturing steep curvatures, but also useful in preventing aliasing that could occur if insufficient sampling points are used in the contact region. For the subsurface mesh, higher resolution will also be useful in predicting the response from a population of mechanoreceptors without aliasing. However, if the entire model were meshed with a high mesh density, the simulation would be computationally too intensive. The region of interest is within millimeters below the skin surface, where these two receptors lie. Therefore, the region near the surface has the highest mesh density. Away from this the element size gradually increases until reaching the fingernail where there are only a few elements.

To develop this model, the previous model was subdivided in the central pad area so that it has a total of 112 axial cross sections, which forms 111 slices of element sets in the axial direction. And at each cross-section, 863 nodes on the surface of the finger were specified. As in the old model, the same number of elements is followed throughout the slices along the axis of the finger, however, from one slice to another, the thickness was varied so as to have larger elements near the ends, where contact with objects are unlikely to occur. And along the axis of the finger the mesh resolution is lower as we move toward the proximal ends. It was decided to keep 12 layers of elements in the radial direction but have varied number of sections in the circumferential direction. From the center to the rim, the number of elements increases from 48 to 128. All the above steps were done using the software MATLAB. The highest resolution is at the pulp region, with a minimum element size about 100 μm × 100 μm × 300 μm. The entire model has a total of 96656 nodes and 95682 elements. Figure 5-3 shows different views of this fingertip model after this re-meshing process.
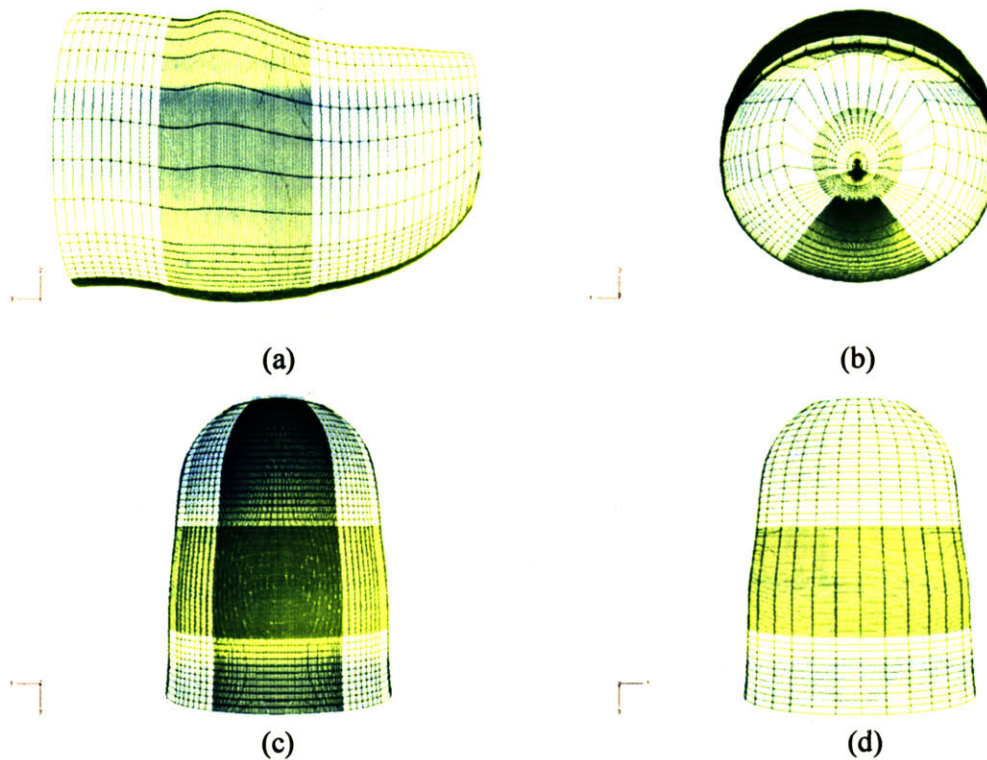
Figure 5-3. The new finite element human fingertip model viewed from different directions: (a) the side view with the pad facing down and the tip pointing to the right (b) the view from the tip with the pad facing down (c) the pad with the tip pointing to the top (d) the dorsal side with the tip pointing to the top.

The outer epidermal ridges were incorporated into the finger model based on the OCT images of the finger pad free of any load. As see in Figure 5-4, the dimension of the each ridge is approximately 0.4 mm horizontally and 0.1 mm vertically in the image. To model the individual ridge smoothly, a second order parametric curve was used to approximate it, as shown in 5-5(a). And to form the normal oval shaped whorl fingerprint pattern on the finger pad, the ridges have to be well distributed. The distribution applied is as shown in Figure 5-5(b), in which the lines represent the positions of the grooves. For all the elliptic shaped curves, the long axis is twice as long as the short axis.
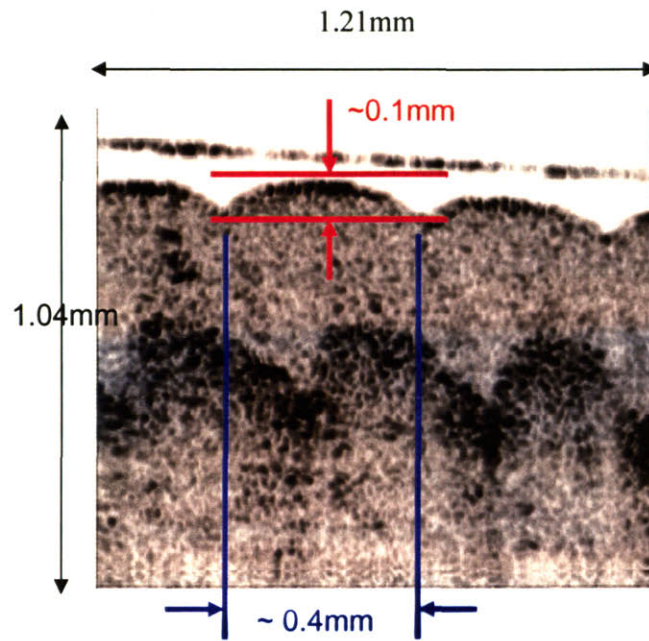
Figure 5-4. Typical dimensions of human fingertip skin structures from an *in vivo* OCT image.

(a)   (b)
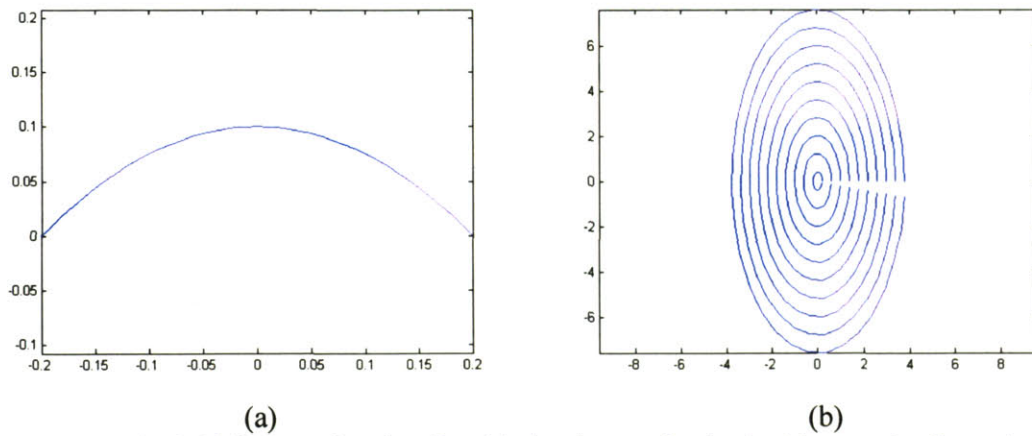
Figure 5-5. The initial approximation for: (a) the shape of a single ridge on the fingertip skin top surface and (b) the distribution of the outer ridges to form oval shaped fingerprints.

5.2 Material properties

The skin is non-linear, anisotropic, and visco-elastic in its mechanical response and exhibits variations in these properties in the same individual across several variables such as body site, temperature and orientation. For simplification, the skin is considered being composed of two layers and the sub-layers of the epidermis and dermis are ignored. Each of the layers is clearly

not homogenous because of its fibrous, cellular, vascular and granular components. In practical problems, we are interested in specimens which are orders of magnitude larger than any of the components of the skin and hence each layer of the skin can be considered as statistically homogeneous for a first analysis. To fully specify the fingertip model, Young's modulus for each layer must be estimated.

In the existent models, the bone was modeled as several orders of magnitude stiffer than the rest of the fingertip, in effect making it a rigid body, and the entire model was meshed so that various layers can be assigned unique stiffness, with each of the layers considered homogenous. The stress-strain relationship of the skin is nonlinear and anisotropic, but the skin was modeled as linear and isotropic for the first analysis. While this might seem to be a broad simplification, the attempt was to model the global characteristics of each skin layer, not the minute structures that are present such that the number of model parameters is kept to a minimum. The refinement of the material model was governed by the matches/mismatches between the model predictions and the experimental data. The parameters used in the specification of the material behavior in a linear isotropic model are the Young's modulus and the Poisson's ratio.

For stimuli prescribed as displacements in the analysis in a homogeneous finite element model, it was shown that the strains are independent of the Young's modulus (Dandekar and Srinivasan, 1996). Because the model was comprised of a series of homogeneous layers, only the ratio of the Young's modulus for the layers were determined. The stresses are related to the strains by a multiplicative constant, and therefore, for the purposes of determining the data trends, the exact value of Young's modulus was not needed. Based on numerical experiments with a variety of Young's modulus ratios and the corresponding matches with experimental data, Dandekar and Srinivasan (1996) proposed the ratio among the layers as 10^4: 10^3: 10^3: 10^8 for the epidermis, dermis, fat, and bone layers, respectively (referred to as 4:3:3:8 model).

In vivo measurements of changes in the human fingerpad volume under indentation stimuli show that the changes are at most 5% (Srinivasan et al., 1992), therefore, to a first approximation, the fingertip can be considered to be incompressible (i.e., Poisson's ratio v is close to 0.5). In this finite element simulation, numerical instabilities occurred as v approached 0.5. Therefore, the value of Poisson's ratio for the finite element analysis was chosen to be a value close to but less than 0.5. A value of 0.48 has been used in the models developed in the past (Dandekar and Srinivasan, 1996; Cysyk and Srinivasan, 1999; Raju and Srinivasan, 1999). Dandekar and

Srinivasan (1996), using a hybrid element formulation, were able to check their model using $v = 0.499$ in the finite element analysis. However, they found no significant difference in the results attained from either value. For the new model that was developed, a value of 0.48 was used. Although the value of the Young's modulus is not needed for stimuli prescribed in terms of displacements and response measured in terms of strains, to simulate the indentation experiments prescribed in terms of forces (loads), the value of the Young's modulus is needed. From the data in previous experiments (Gultai and Srinivasan, 1996) and 2D elastic finite element model simulation (Cysyk and Srinivasan, 1999), the elastic moduli of the four layers, the epidermis, dermis, fat, and bone, were estimated approximately 0.15, 0.015, 0.015, and 1500 MPa, respectively. Using Gultai and Srinivasan's experimental data (1996) to fit a 3D finite element model of the human fingertip, another set of values 0.18, 0.018, 0.018 and 1800 MPa were obtained for the Young's modulus of these four layers. (Dandekar et al., 2003)

In the new model, the ratio of Young's modulus between the epidermis and the dermis would be kept as 6.6, which is the value obtained from the axial strain imaging experiment described in Chapter 4. The ratio of the rest of the layers would be adjusted to match the OCT images. And the value of the Young's modulus would be estimated using the load data from the indentation experiment described earlier (see Chapter 4).

5.3 Boundary Conditions

In our indentation experiments in Chapter 3, the fingernail was glued to the stage to prevent any motion of the fingertip. This condition was simulated by suppressing all the degrees of freedom for the nodes defining the fingernail. Nine nodes were specified as belonging to the nail on each cross section of the model. The nine dots along the upper part of the circumference of the cross section shown in Figure 5-1(b) are the nodes representing the nail on that cross section. These nodes were constrained to simulate a concentric fingernail of anatomically correct dimension.

5.4 Results

The cross section of the new fingertip model cut through from the top of the fingerpad is shown in Figure 5-6. This cross sectional plane is located at 14 mm from the distal tip of the finger. As shown in the enlarged drawing on the right, this model includes the fine structure of the outer ridges in its central pad region and the intermediate and limiting ridges, which project into the

dermis region. As described by Cauna (1954), the intermediate ridges normally appear as midline folds with the sweat passages, which are under the peaks of the outer ridges, and the limiting ridges are the two folds corresponding to the surface grooves. Therefore, the distribution of these ridges in the model also followed this rule. And because the surface ridges and grooves were distributed so as to form the oval shaped pattern on the finger pad, the distribution of the intermediate and limiting ridges on each slice wouldn't be the same. The size of the elements forming these inner ridges is approximately 100 μm × 100 μm × 300 μm at the central pad, while the length of the elements lying immediately underneath the skin surface to form the stratum corneum ranges from 300 μm to 400 μm, depending on if it is near the grooves or the peaks. The SA-I receptors would be considered residing within the end section of the intermediate ridges, which is at the depth approximately 0.7 - 1.0 mm, while the RA receptors residing within the dermis region immediately underneath the stratum corneum, which is at a depth approximately 0.35 - 0.65 mm. Figure 5-7 shows the external shape of the model. The oval shaped pattern on the finger pad due to the surface ridges and grooves can be seen.

Figure 5-8 shows the OCT images from two adult female subjects with their index fingers free of load and the finite element model boundaries superimposed over the images. The top curve shown on each image was obtained from the top surface of the finite element fingertip model, while the lower smooth curve was the line in the model for approximating the inner boundary of the stratum corneum. As can be seen, the surface ridges matched quite well and the boundary for defining the range of stratum corneum also fits appropriately.
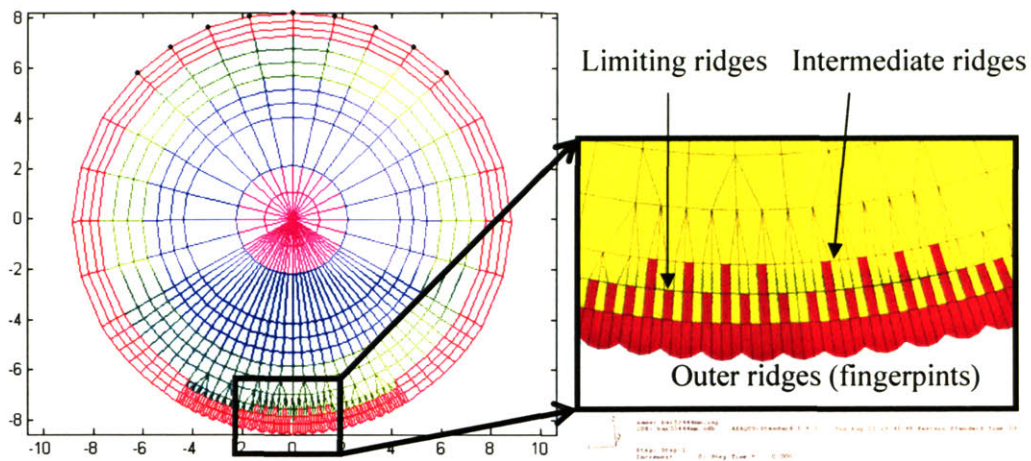
Figure 5-6. The cross section of the human fingertip model perpendicular to the axis of the finger, showing the outer and inner ridges added. The unit of the coordinates on the left plot is mm on both axes.
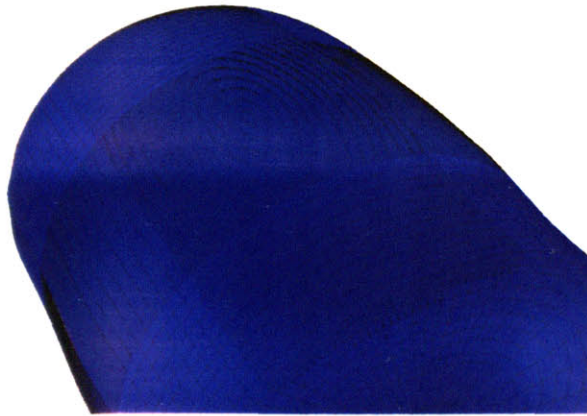
Figure 5-7. The fingertip model showing the fingerprints around the center of the finger pad.
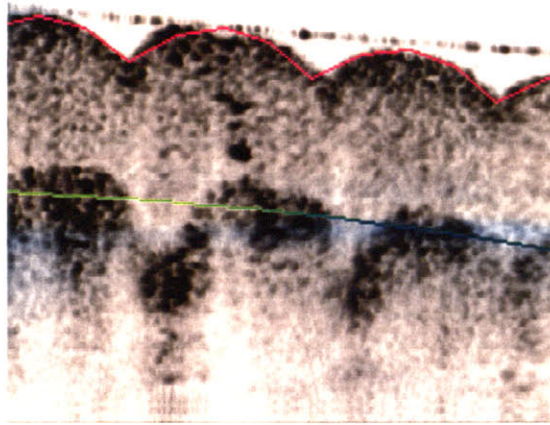
(a)
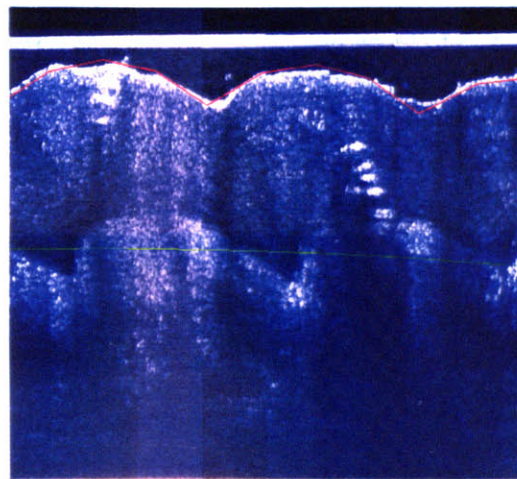
(b)

Figure 5-8. The finite element model's top ridged surface shape was verified by superimposing its boundaries on the OCT image of the finger pad under zero load. (a) and (b) are from two adult female subjects.

Given that the mechanoreceptors that are of interest to us are located close to the surface of the finger pad, it is important to verify that the experimentally observed surface deformations and those predicted by the model under similar mechanical loadings match. To pick the right ratio of Young modulus among the layers, different possible ratios were substituted into the model while keeping the ratio between the epidermis and the dermis as 6.6 (see Chapter 4) and the simulation

results for the rectangular bar case (as described in the OCT experiment, Chapter 3) were compared with the corresponding images obtained through OCT (see Figure 3-20). As shown in Figure 5-9, a ratio of $6.6 \times 10^3 : 10^3 : 10^3 : 10^8$ among the epidermis, the dermis, the subcutaneous fat, and the bone has shown a good match between the OCT images and the model predictions. This match validates the spatial response characteristics of the model using this Young's modulus ratio.

(a)

(b)

(c)

(d)

(e)
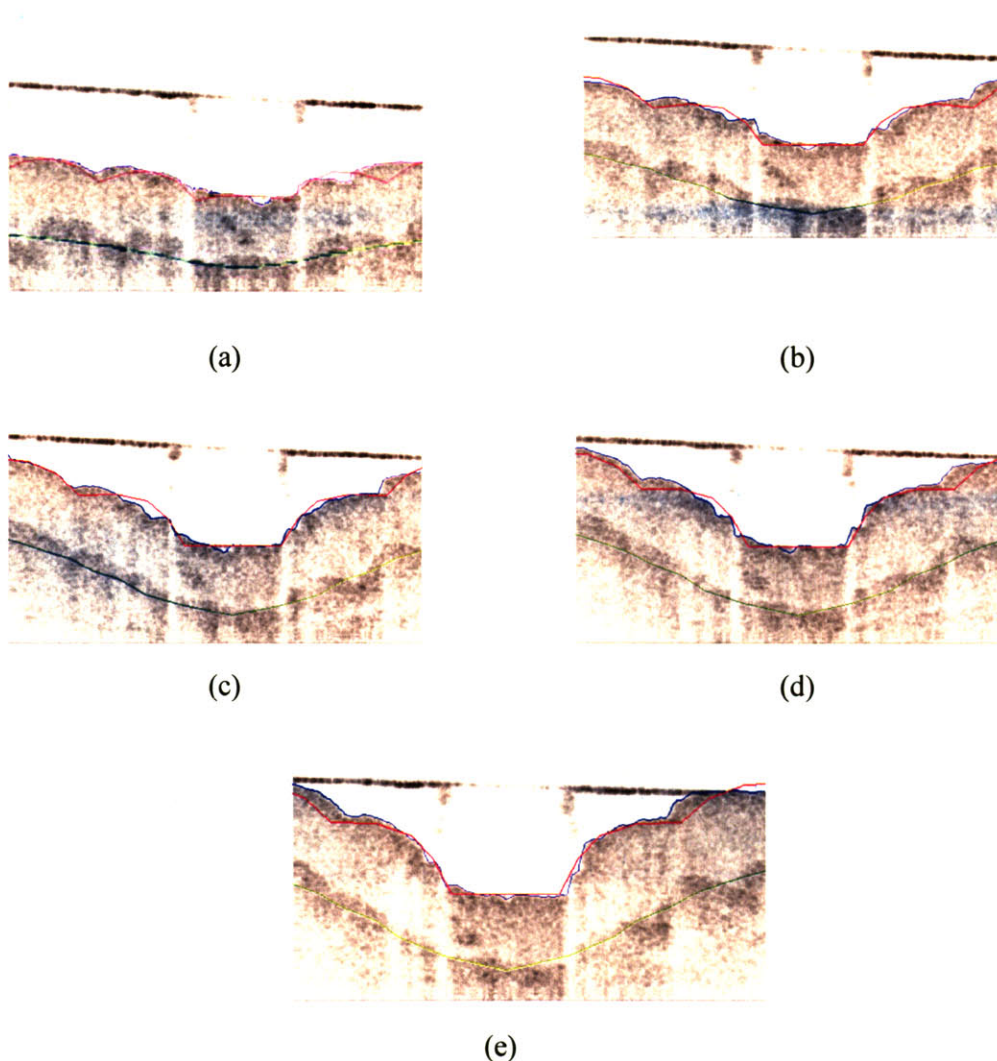
Figure 5-9. Biomechanical verification of the finite model by comparing its top surface under the loading of rectangular bar with the OCT image: Depths of indentations of (a) 0.5 mm (b) 1.0 mm (c) 1.5 mm (d) 2.0 mm (e) 2.5 mm. The dimensions of each of the images are 1.05 mm (vertical) × 1.68 mm (horizontal).

To estimate the exact Young's moduli for different layers, a multiplication constant was determined by matching the model predictions of the load at different indentation stages with the experimental data, which is an average of the loading data from three trials indenting the rectangular bar on a female adult subject's index finger. A multiplication constant of 19 brings about a good loading curve match as shown in Figure 5-10. This multiplication constant results in Young's moduli of 0.1254 MPa, 0.019 MPa, 0.019 MPa, and 1900 MPa for the epidermis, the dermis, the subcutaneous fat, and the bone, respectively. Table 5-1 shows Young's moduli of the epidermis and the dermis from different experimental and simulation results. As can be seen, the obtained Young's modulus for the epidermis is closer to the result from Maeno, Kobayash & Yamazaki (1997), while the obtained value for the dermis is closer the result from Dandekar, Raju, and Srinivasan (1998).
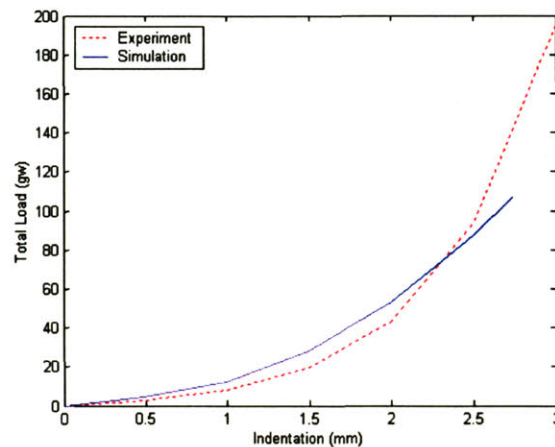
Figure 5-10. The absolute Young's modulus values were picked to match the experimental loading data. The experimental data (dotted line) is from an average of 3 trials one subject and the Young's moduli for the epidermis, dermis, fat, and bone are 1.254e5 Pa, 1.9e4 Pa, 1.9e4 Pa, and 1.9e9 Pa, respectively.

Reference	Method	Young's modulus of the epidermis	Young's modulus of the dermis
Maeno, Kobayashi, and Yamazaki (1998)	Human cadever finger matched 2D FE model with load-displacement data	0.136 MPa	0.08 MPa
Cysyk and Srinivasan (1999)	Human finger *in vivo* matched 2D FE model with load-displacement data	0.15 MPa	0.015 MPa
Dandekar, Raju, and Srinivasan (2003)	Human finger *in vivo* matched 3D FE model with load-displacement data	0.18 MPa	0.018 MPa
This study	Human finger *in vivo* axial strain Imaging and then matched 3D FE model with load-displacement data	0.125 MPa	0.019 MPa

Table 5-1. The comparison of Young's moduli of the epidermis and dermis of the human fingertip from different studies.

Chapter 6
Simulations Using the Fingertip Model

The finite element model of the fingertip described previously enables simulations of indenting the human fingertip with different shapes of objects to different depths and computation of various mechanical responses. Figure 6-1 shows the contour plots of the contact pressure distribution when indented by four different shapes of objects to a maximum indentation depth of 2 mm, which can show the contact regions on the finger pad. As can be seen from the figures, due to the fingerprint structure and the high stiffness of the epidermis, the grooves of the finger pad are not in contact with the objects at all in the cases with spherical and cylindrical indentors (Figure 6-1(a), (c) and (d)), thus have zero contact pressure at those locations. In the case of the rectangular bar (Figure 6-1(b), the axis of the bar is parallel to the long axis of the finger), even if the two sharp edges of the bar can touch the grooves when encountered, the long stripe of indented area is not in contact all the way through the bar, instead, there are areas with zero contact pressure due to the grooves. This contact phenomenon cannot be simulated in any of the previous models where skin surface ridges (fingerprints) were not incorporated. As is to be expected, when the fingertip model is indented by a cylindrical indentor (Figure 6-1(a), the axis of the cylinder is parallel to the long axis of the finger), the contact area is longer along the cylinder axis than the ones due to spherical indentor (Figure 6-1(c) and (d)). For spherical indentors (Figure 6-1(c) and (d)), as the curvature increases, the area of contact decreases. This makes intuitive sense considering that sharper objects can only come into contact with smaller area of the skin when pressed into the skin to a given depth.
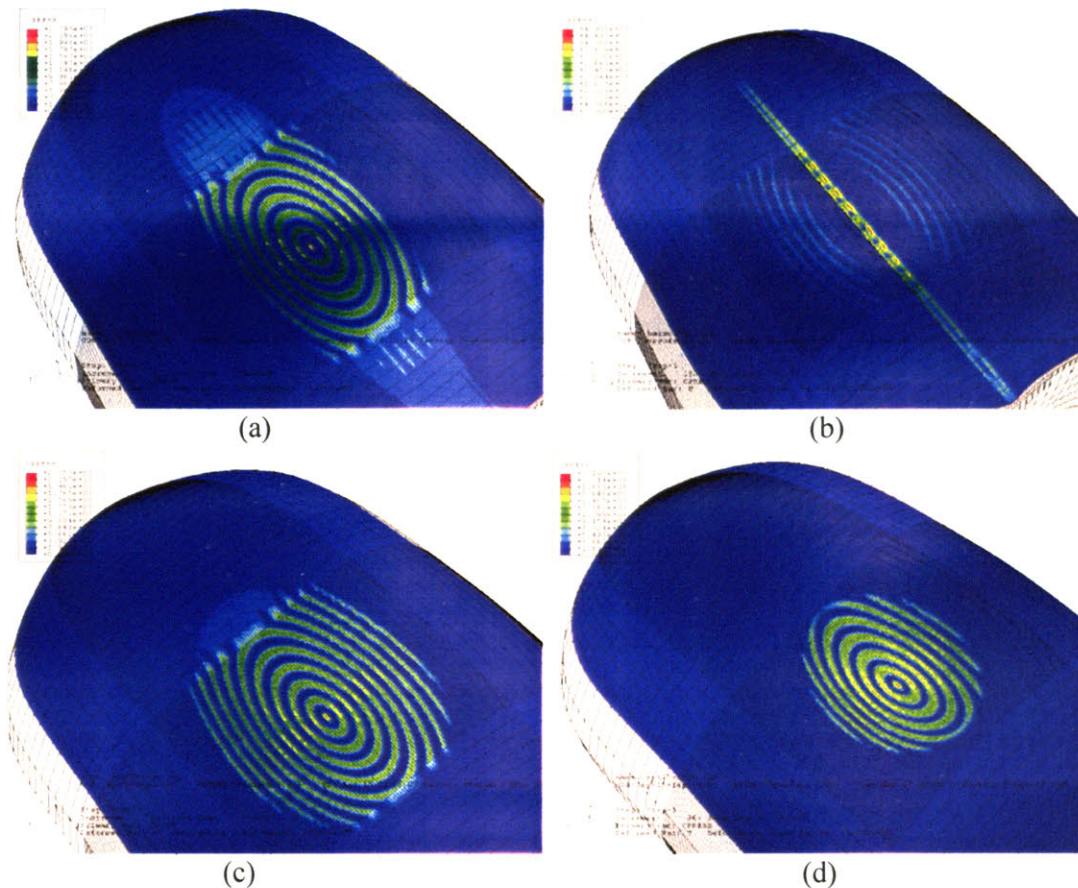
Figure 6-1. The contour plots of contact pressure distribution which can show the contact regions on the fingertip model due to the indentation by different shapes of objects. The finger model are indented to a maximum depth of 2 mm by (a) cylindrical indentor (R = 7.8 mm, the axis of the cylinder is parallel to the long axis of the finger) (b) rectangular bar (height × width = 0.53 mm × 0.44 mm, the axis of the bar is parallel to the long axis of the finger) (c) spherical indentor (R = 25.9 mm) (d) spherical indentor (R = 7.8 mm).

Previous research in MIT Touch Lab showed that strain energy density (SED) is a direct measure of the distortion of the Merkel receptors caused by contact with shaped objects (Dandekar and Srinivasan, 1995; Cysyk and Srinivasan, 1999; Raju and Srinivasan, 1999, Dandekar et al., 2003), and thus is hypothesized to be the relevant stimulus, that is, a strain/stress measure transduced by the neural receptor to convey the sense the touch. Figure 6-2 shows the evolution of SED of the elements at depth 0.65 - 0.95 mm within the model when indented by four different shapes of objects to a maximum indentation of 2.5 mm. As illustrated in Section 5.1 and also shown in the drawing at the top of Figure 6-2, this range of depth corresponds to the third layer of elements from the skin surface. Three different line types (dotted, dashed, and

96

solid) are used to represent three different types of locations at this depth. The dashed lines refer to the area below the limiting ridges, the solid lines refer to the area at the end of the intermediate ridges, and the dotted lines to the area between the limiting and the intermediate ridges, respectively. Near the center of the finger pad, a total of 36 elements along this path on a cross section perpendicular to the long axis of the finger were involved in this analysis. The plot shows that SED is higher at the locations of the intermediate ridges, where Merkel disks normally reside. The higher stiffness of the epidermis protruding into the dermis causes stress concentration, resulting in high SED. This is again a phenomenon that the previous models, which neglected the ridged interface between the epidermis and the dermis, can not display.

Figure 6-3 shows the distribution of SED from the simulation results of the old model (Zhou and Srinivasan, 2002) without the ridged structure on the skin surface and between the epidermis and the dermis, and the new model with both outer and inner ridges. These two models were indented by a spherical indentor (R = 7.8 mm) from 0 to 2.5 mm, and the SED distribution at different indentation stages were shown as multiple curves rising from the bottom to the top of the plot along a path of 54 elements in the middle plane along the long axis of the finger. As seen from Figure 6-3(a), the model without any ridged structures renders a smooth distribution of SED with its maximum appearing near the center, where the indentation reaches the maximum, while the distribution of SED obtained from the new model shows multiple sharp spikes. The locations of those spikes correspond to the locations of the intermediate ridges, where Merkel disks normally reside. From the above observation, at the locations of Merkel disks, SED is higher than the other locations at the same depth when indented by objects with smooth surface.

dashed   dotted   solid

(a)

(b)

(c)

(d)
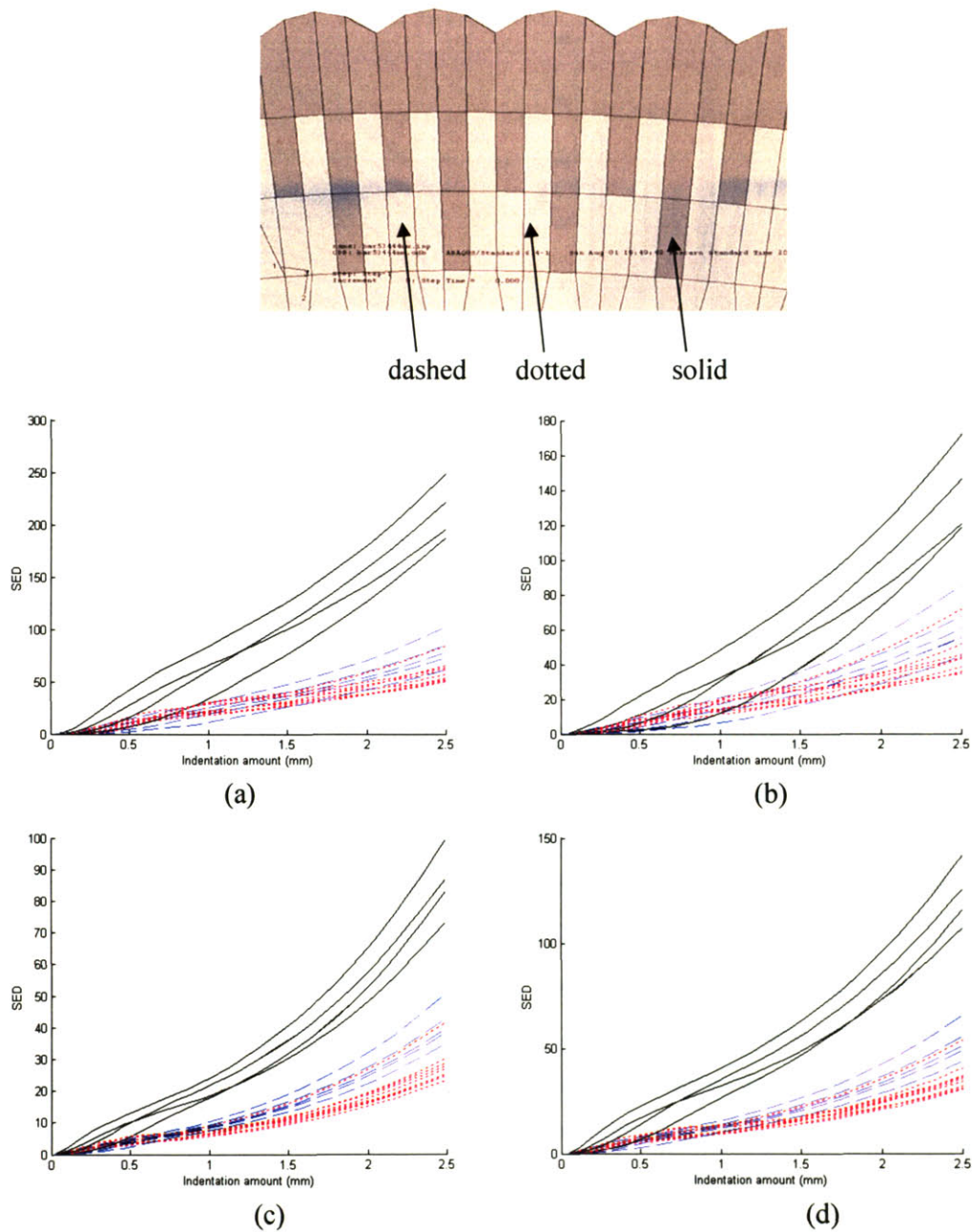
Figure 6-2. The evolution of the strain energy density (SED) at depth 0.65 - 0.95 mm when the fingertip model was indented from 0 to 2.5 mm. As illustrated in the schematic at the top, three different line types represent three different locations within this depth. The four plots were obtained from the finger model indented by (a) spherical indentor (R = 7.8 mm) (b) cylindrical indentor (R = 7.8 mm, the axis of the cylinder is parallel to the long axis of the finger) (c) flat surface (d) spherical indentor (R = 25.9 mm). The plots show that SED is higher at the location of the intermediate ridges (curves shown as solid lines), where Merkel disks normally reside.
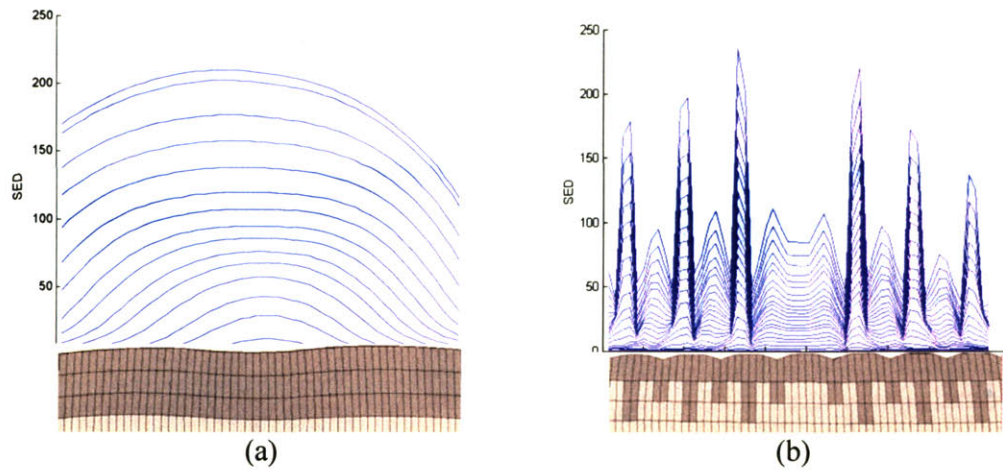
Figure 6-3. Comparison of SED distribution at depth 0.65 - 0.95 mm due to indentation by a spherical shaped indentor (R = 7.8 mm) in a model (a) with neither outer nor inner ridges (b) with the new model built with both inner and outer ridges. The multiple curves rising from the bottom of each plot to the top show the different stages of indentation (from bottom to top, the amount of indentation is from 0 to 2.5 mm). The horizontal axis is the numerical labels of 54 elements along the path in the middle plane of the finger pad parallel to the long axis of the finger.

To see how different shapes of objects can affect the SED distribution at these locations with Merkel disks, SED at these potential locations for Merkel disks is plotted in Figure 6-4. Figure 6-4(a) shows that along the path on the axial cross section of the finger at an indentation depth of 1 mm, the spherical indentor and the cylindrical indentor with the same radius of curvature of 7.8 mm result in a distribution with a dome shape. The drop on both sides is due to the reduced indentation away from the center of the pad. The flat surface and the spherical indentor with larger radius of curvature (R = 25.9 mm) cause a flatter distribution of SED because at this indentation stage of 1mm, the contact area is larger and the curve drops due to the loss of contact are outside this range. Viewed from the path in the middle plane along the long axis of the finger (figure 6-4(b)), at the indentation of 1mm, the cylindrical indentor and the flat surface cause a pretty flat distribution of SED in this range of elements. This is because that in this cross section, the cylindrical indentor has its side with zero curvature in contact with the finger pad. For spherical indentors, the one with larger curvature, or equivalently a smaller radius of curvature of 7.8 mm, shows a curve with sharper drops on both sides. Notice that at this indentation stage, the distribution of SED due to the spherical indentor with a radius of curvature of 7.8 mm shows the maximum value at the center. Without considering the case of the cylinder, the other three

99

indentors can represent spherical indentors with radii of curvature 7.8 mm, 25.9 mm, and infinity, or with curvatures 128.2 m^{-1}, 38.6 m^{-1}, and 0 m^{-1}, respectively. As shown in Figure 6-5 (a) and (b), at the center of the fingerpad, a higher curvature causes a higher SED value, which correlate with the trend of the spatial response profile recorded from an SA-I mechanoreceptor of a primate fingertip by Goodwin et al. in 1995 (Figure 6-5(c) and (d)).

(a)   (b)
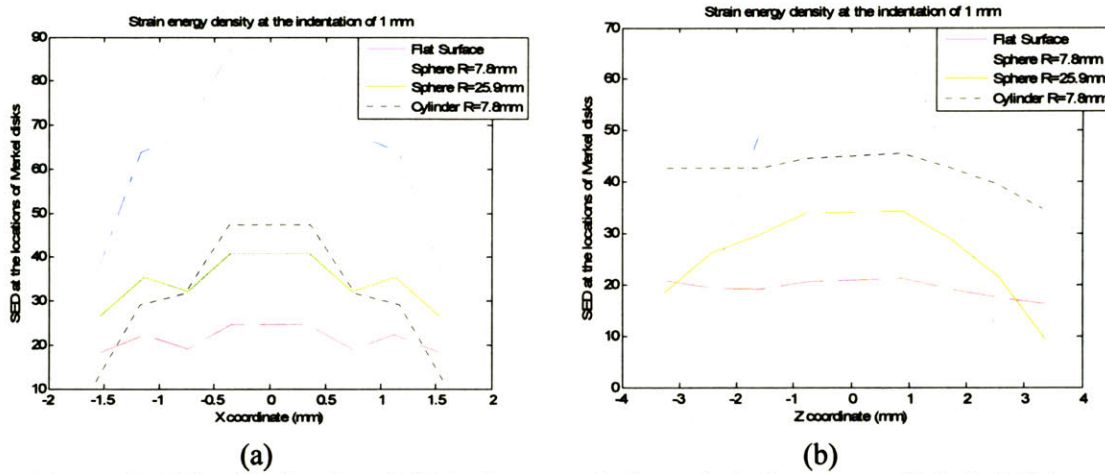
Figure 6-4. The distribution of SED along a path through the locations of Merkel disks. Different line types represent simulation results using different indentors: dashed: flat surface, dashdot: spherical indentor (R = 7.8 mm), solid: spherical indentor (R = 25.9 mm), dotted: cylindrical indentor (R = 7.8 mm, the axis is parallel to the long axis of the finger). (a) the path contains 8 elements on the axial cross section of the fingertip model (b) the path contains 8 locations in the middle plane along the long axis of the finger. The indentation is 1 mm from the top of the finger pad.

Besides the contact area and the strain energy density, the maximum compressive and tensile strains were also investigated. Figure 6-6 shows the distribution of the maximum compressive strain (MCS) at depth 0.35 - 0.65 mm within the fingertip model when indented by four different shapes of objects. As illustrated in Section 5.1, this range of depth corresponds to the second layer of elements in the model from the skin surface. Three different line types (solid, dashed, and dotted) were used to represent three different types of locations at this depth. The dashed lines refer to the area of the limiting ridges, the dotted lines refer to the area on the intermediate ridges, and the solid lines the area between the limiting and the intermediate ridges, respectively. The plot shows that MCS is high within certain indentation stages initially in the area between the limiting the intermediate ridges, where Meissner's corpuscles normally reside.
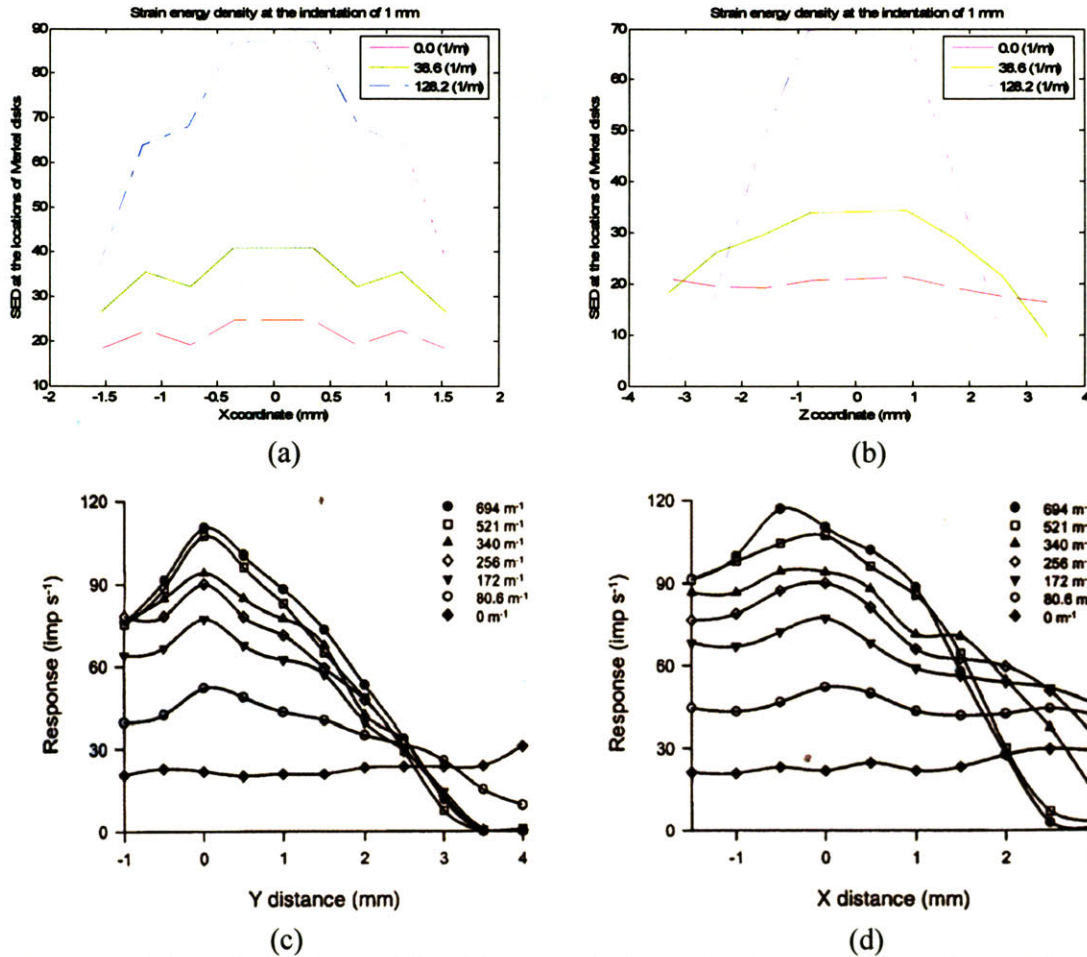
Figure 6-5. The distribution of SED (a) perpendicular to the long axis of the finger (b) along the long axis of the finger and the spatial response profile recorded from an SA-I mechanoreceptor of a primate fingertip (Goodwin et al., 1995) (c) perpendicular to the long axis of the finger and (d) along the long axis of the finger when a spherical indentor was indented.

Considering that Meissner's corpuscles belong to the rapidly adapting (RA) type of mechanoreceptors which are sensitive to dynamic changes in stimuli, this sensitivity to the indentation at these locations during certain low loading stages might imply the special characteristic of this location. And the indentation range of high MCS varies among these cases with different indentors. The range is shortest for the case of flat surface, second shortest for the spherical indentor with larger radius of curvature (R = 25.9 mm). Both spherical and cylindrical indentors with a small radius of curvature of 7.8 mm cause a longer range of this high MCS.

dotted   solid   dashed
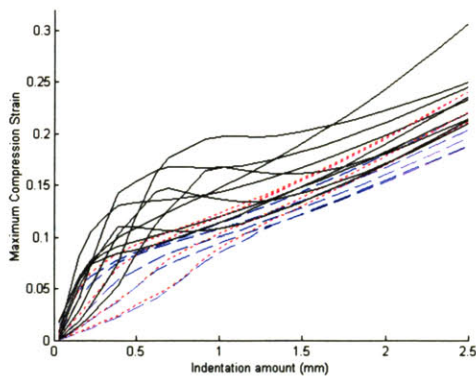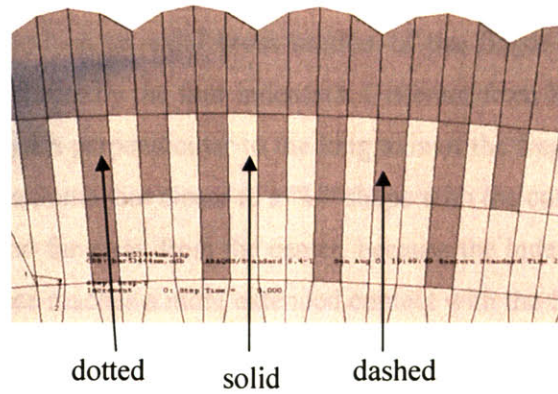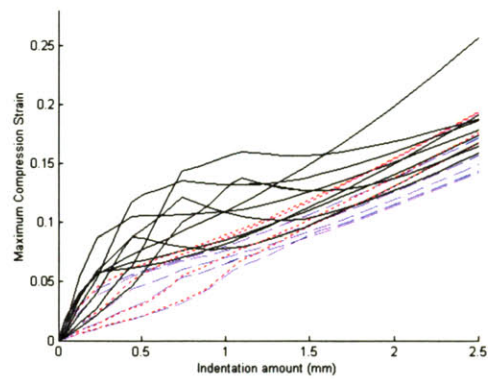
(a)   (b)
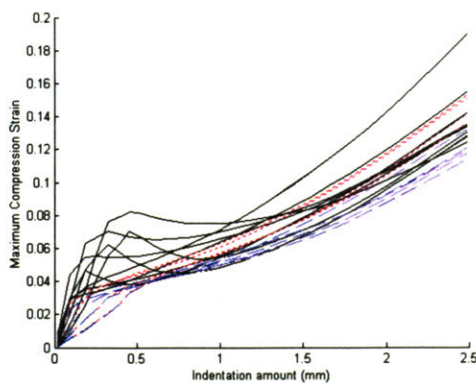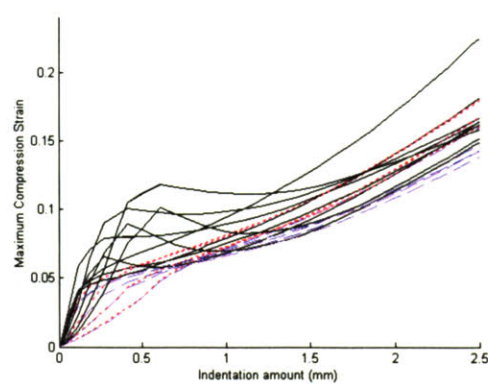
(c)   (d)

Figure 6-6. The distribution of the maximum compression strain (MCS) at depth 0.35 - 0.65 mm shows that MCS is higher at certain indentation range initially at the location between the intermediate ridges and the limiting ridges, where Meissner's corpuscles normally reside. (a) spherical indentor (R = 7.8 mm) (b) cylindrical indentor (R = 7.8 mm) (c) flat surface (d) spherical indentor (R = 25.9 mm)

Figure 6-7 shows the distribution of MCS at the locations of Meissner's corpuscles along a path on top of the fingerpad and on an axial cross section of the finger when the fingerpad was indented to 0.3 mm and 1.0 mm by the four indentors. Different from SED, the general shape of the distribution along the path perpendicular to the long axis of the finger at 0.3 mm indentation (Figure 6-7(a)) is not like a dome, but closer to a "U" shape with the curve appearing zigzag. But when it goes to the sites too far away from the center, because the indentation decreases to zero, MCS drops. The flat surface reaches a more extended contact with the finger pad, so the shape is closer to a "U". For the other 3 cases clear drops occur at the two sides.

Figure 6-7. The distribution of maximum compression strain (MCS) along a path of the locations of Meissner's corpuscles at indentation of (a) 0.3 mm (b) 1.0 mm. This path contains 16 elements perpendicular to the long axis of the finger.

When the indentation is increased to 1 mm (Figure 6-7(b)), which means more skin surface is in contact with the indentor, it can be seen that along the path perpendicular to the long axis of the finger, the spherical and cylindrical indentors with the same radius of curvature of 7.8 mm show pretty similar "U" shaped distribution of MCS, while the spherical indentor with larger radius of curvature (R = 25.2 mm) and the flat surface show a much flatter distribution due to this further indentation. The curve still displays the zigzag characteristic as before. Noticeable is the spherical indentor with R = 7.8 mm reaches the highest MCS among these four cases.

Figure 6-8 shows the distribution of the maximum tensile strain (MTS) of the fingertip model at depth 0.35 - 0.65 mm when indented by the same four shapes of objects, corresponding to the second layer of elements in the model from the skin surface. Three different line types (solid, dashed, and dotted) are used to represent three different types of locations within this layer. Dashed lines refer to the area of the limiting ridges, dotted lines refer to the area on the

intermediate ridges, and solid lines the area between the limiting and the intermediate ridges, respectively. Like MCS, the figure shows that the MTS is higher initially within certain indentation range within the area between the limiting the intermediate ridges, where the Meissner's corpuscles normally reside. And the result also shows that the spherical and cylindrical indentors with R = 7.8 mm cause the longest range of high MTS at these locations while the flat surface indentor causes the shortest.

Again, to investigate the effect of the shapes of the objects on the distribution of MTS at the locations of Meissner's corpuscles, plots of MTS at these locations along a path in the middle plan along the long axis of the finger were made. Figure 6-9 shows the distribution of MTS at the locations with Meissner's corpuscles at a maximum indentation of 0.3 mm and 1 mm, respectively. The general shape of MTS is pretty close to MCS, but different from MCS, and the case of cylindrical indentor shows a higher value compared to the other cases. It can be imagined that in the indentation process, the compressive strain is the very direct mechanical response and the tensile strain appears because the tissue is forced to move more or less in the perpendicular direction when compressed to preserve volume as required by incompressibility of skin. Intuitively, in the case of spherical indentor, under the compression, the tissues have more directions to stretch, so it is not easy to cause a large tensile strain in single direction. But in the case of cylindrical shaped indentor, more skin surface is in contact with the indentor (compare figure 6-1 (a) and (d)), which results in more restriction on the available directions for the tissue to stretch, and therefore larger tensile strain in a single direction can be caused.

Figure 6-10 shows the distribution of SED at the locations of the Merkel disks along a path on an axial cross section of the finger near the center of the finger pad when the fingertip model was indented by a rectangular bar to a depth of 1 mm. The 8 circles are the data points at these locations and the two vertical dashed lines represent the position and size of the thin bar (at the center horizontally, bar width = 0.44 mm). The general pattern showed there is a peak at the center due to the bar.

104

dotted   solid   dashed

(a)

(b)

(c)

(d)
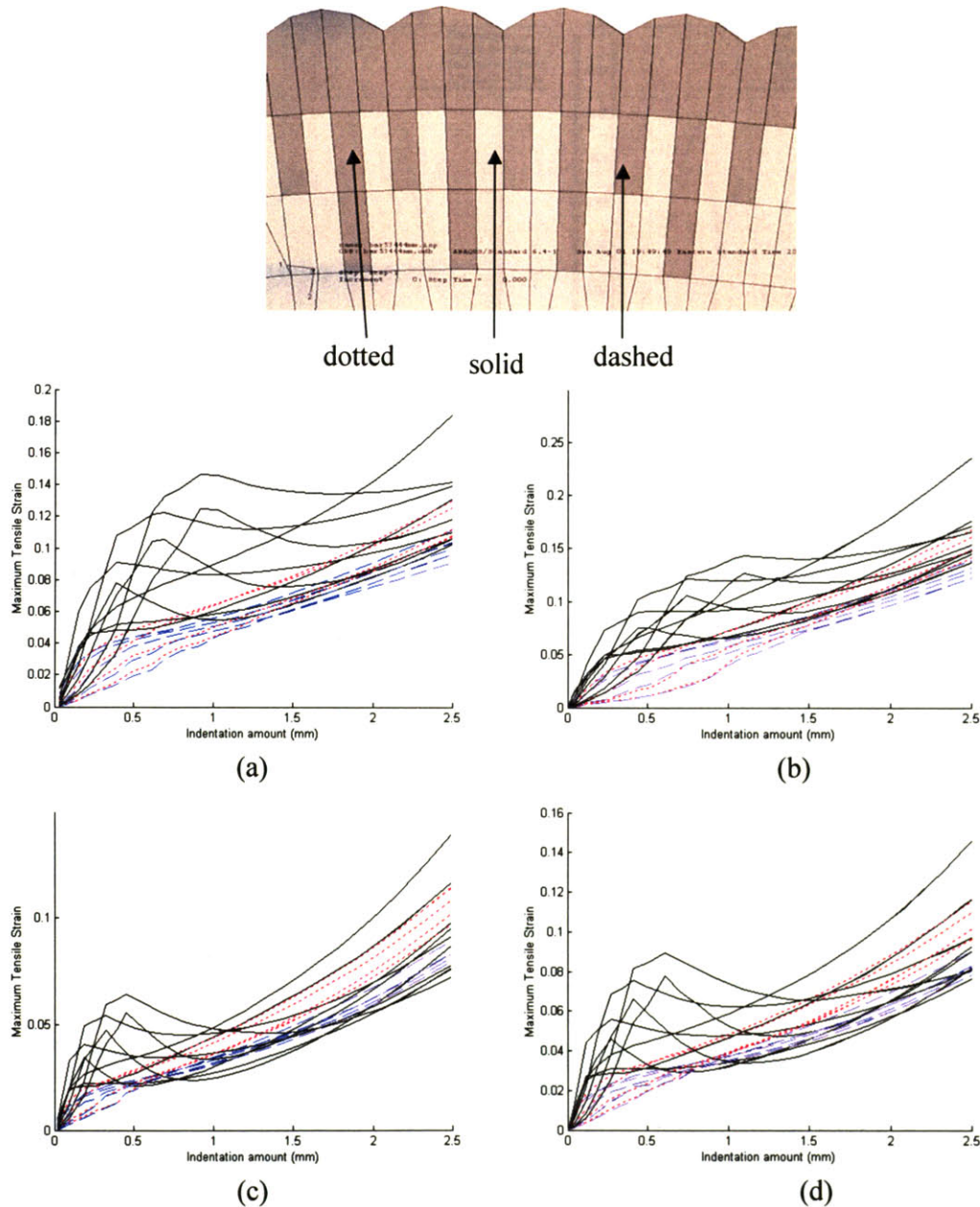
Figure 6-8. The analysis of the maximum tensile strain (MTS) at depth 0.35 - 0.65 mm. As shown in the schematic, three different line types represent three different locations within this depth range. The four plots were obtained from the finger model indented by (a) spherical indentor (R = 7.8 mm) (b) cylindrical indentor (R = 7.8 mm, the axis of the cylinder is parallel to the long axis of the finger) (c) flat surface (d) spherical indentor (R = 25.9 mm). The plots show that MTS is higher within certain indentation stages initially at the locations between the intermediate and limiting ridges, where Meissner's corpuscles normally reside.
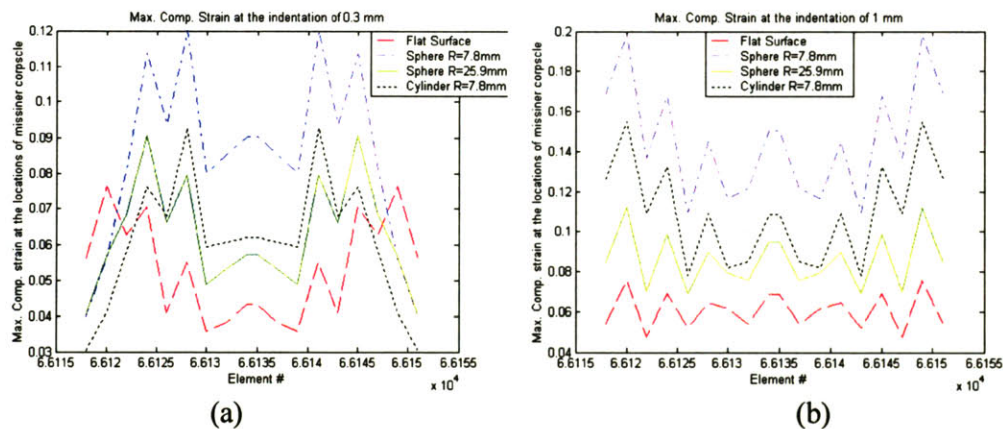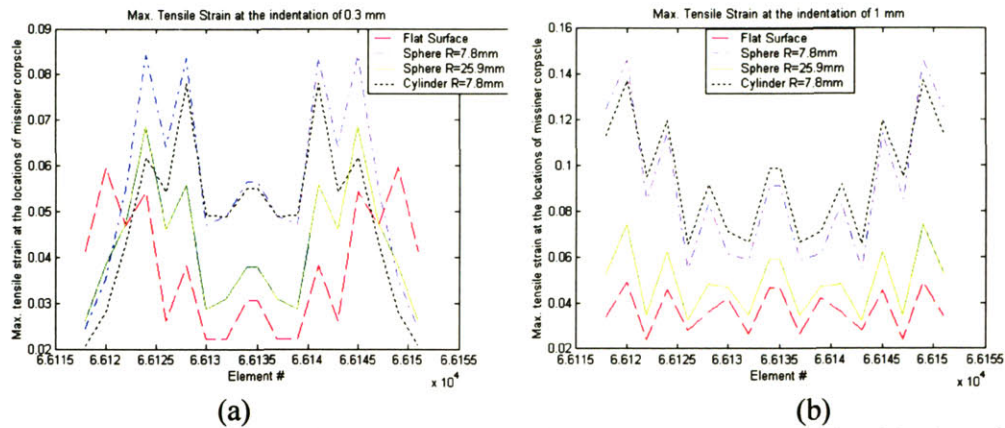
Figure 6-9. The distribution of maximum tensile strain (MTS) along a path of the locations of the Meissner's corpuscles at indentation of (a) 0.3 mm (b) 1.0 mm. This path contains 18 elements perpendicular to the long axis of the finger.

Figure 6-10. The distribution of SED at the locations of the Merkel disks along a path on the axial cross section of the fingertip model when it was indented by a rectangular bar (the bar is along the axis of the long axis) to a depth of 1 mm. The 8 circles are the data points at these locations of Merkel disks and the two vertical dashed lines represent the position (at the center) and size of the bar (width = 0.44 mm).

Figure 6-11 shows the distribution of MCS and MTS at the locations of Meissner's corpuscles along a path on an axial cross section of the finger near the center of the fingerpad when the fingertip model was indented by the rectangular bar to a depth of 1mm.

Figure 6-11. The distribution of MCS ((a)) and MTS ((b)) at the locations of the Meissner's corpuscles along a path on an axial cross section of the finger near the center of the finger pad when the fingertip model was indented by the rectangular bar (the bar is along the long axis of the finger) to a depth of 1mm. The 18 circles are the data points at these locations of Meissner's corpuscles and the two vertical dashed lines on each plot represent the position and size of the thin bar (width = 0.44 mm).

Like the plot of SED, the plots also showed a highest value of MCS and MTS at the center due to the bar. And because the density of Meissner's corpuscles is higher than Merkel's disks (approximately 2:1), the MCS and MTS plots were based on more data points and thus can show the more detailed shape of the distribution.

For a bar shaped indentor with larger width, say 3 mm, the SED distribution at the locations of Merkel disks along a path on an axial cross section of the finger near the center of the fingerpad (Figure 6-12(a)) shows two peaks near the edges of the bar, and then drops on two sides. This phenomenon correlates with the general trend of the spatial response profile obtained from an SA-I mechanoreceptor of a primate fingertip by Phillips and Johnson (1981), as shown in Figure 6-12(b).
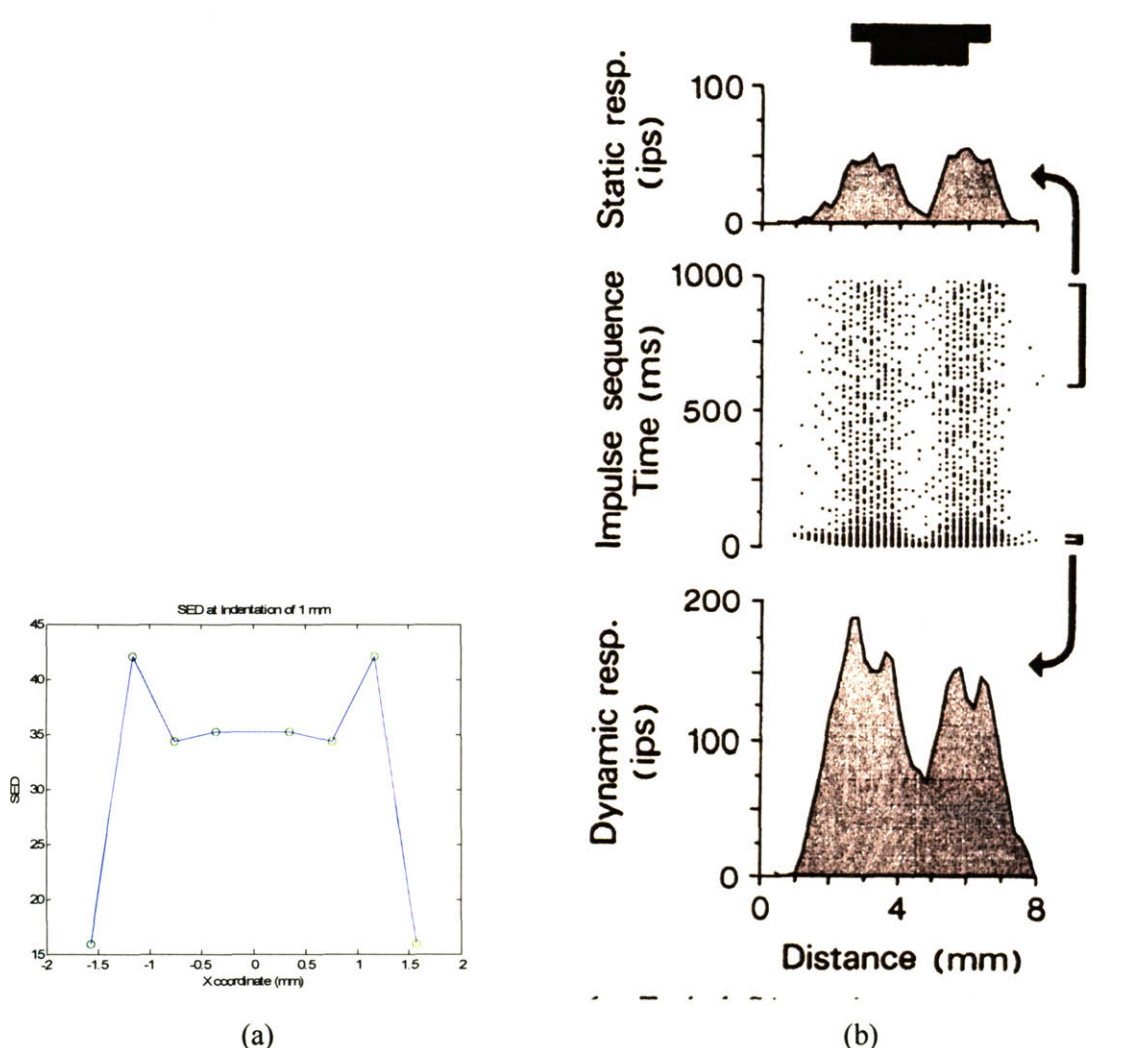
Figure 6-12. (a) The distribution of SED at the locations of the Merkel disks along a path on an axial cross section of the fingertip model near the center of the finger pad when it was indented by a 3mm bar (along the long axis of the finger) to a depth of 1 mm. (b) The spatial response profile obtained by Phillips and Johnson in 1981, which was recorded from a single SA-I mechanoreceptor in the primate fingertip when indented by a 3 mm bar.

Simulation of an indentor with a step shape was also conducted. Figure 6-13 illustrates the shape of the indentor. The step size is 0.53 mm vertically at the central position horizontally, and the same shape extends along the long axis of the finger. Figure 6-14(a) shows the distribution of SED at the locations of Merkel's disks along a path on the axial cross section of the fingertip model near the center of the fingerpad when an indentation of 1 mm was applied. There are a total 18 data points within this range marked as the circles and the vertical dashed line locates the

position of the step. From the plot, the indentor moved a little bit to the left, where the indentor surface is closer to the skin surface from the start and indented the skin more. As expected, the highest SED value occurred around the location of the step change in the stimulus, and due to the asymmetry of this indentor, the distribution of SED is also asymmetric. The left side of the plot, corresponding to the skin indented more due to the step, shows higher SED than the left side. Figure 6-14(b) shows the spatial response profiles recorded from an SA-I mechanoreceptor of a primate fingertip when it was indented by steps with minor shape difference (Srinivasan and LaMotte, 1987). The general trend of the profiles matches the distribution of SED shown in Figure 6-14(a).
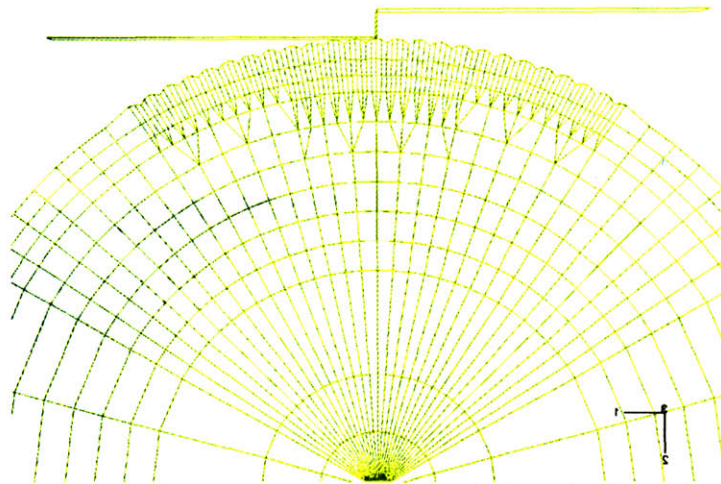
Figure 6-13. An indentor with a step shape was used to indent the fingertip model. For ease of understanding, the figure shows at one of the axial cross sections of the fingertip model. The size of the step is 0.53 mm, and the shape of the indentor is the same along the long axis of the finger (perpendicular to the paper).

Figure 6-15 shows the distribution of MCS and MTS at the locations of Meissner's corpuscles in this case. The highest values also occurred around the step change, where the vertical dashed line shows the position of the step, which moved to the right a little bit during the indentation. Like the plot of SED, the right side of the step change shows slower drop of the value than the left hand side, thus forms an asymmetric curve.
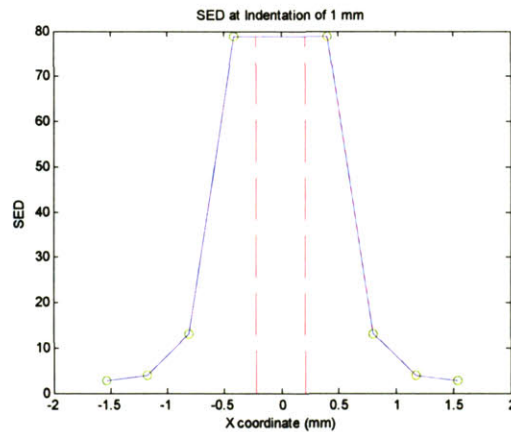
(a)

(b)
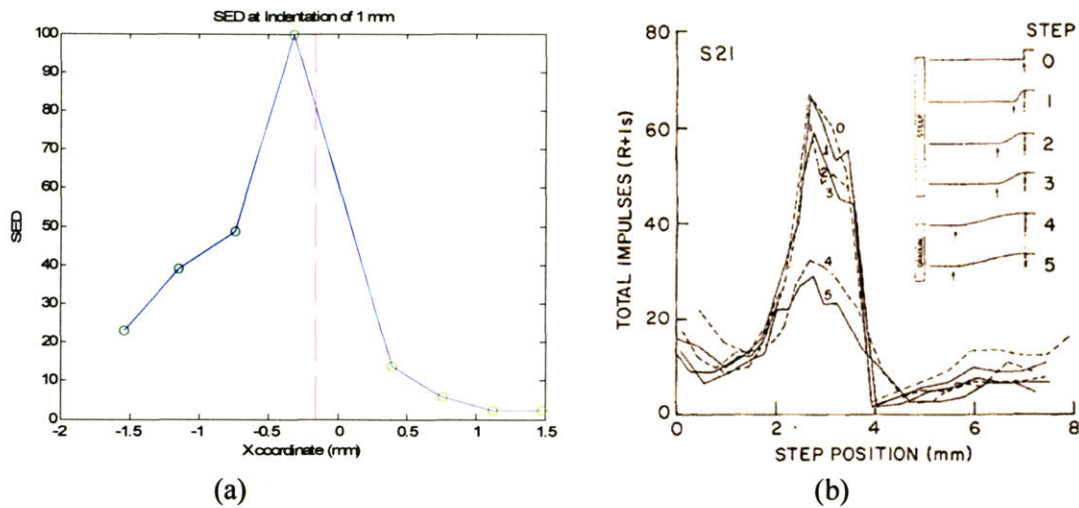
Figure 6-14. (a) The distribution of SED at the locations of Merkel's disks along a path on the axial cross section of the finger near the center of the finger pad when the fingertip model was indented by a step shaped indentor, as shown in Figure 6-13, to a depth of 1 mm. The 8 circles are the data points. The vertical dashed line shows the position of the step, which was originally at the center with an x coordinate of zero and moved a little to the left at this indentation stage. (b) the spatial response profiles recorded from an SA-I mechanoreceptor of a primate fingertip when it was indented by steps (Srinivasan and LaMotte, 1987).
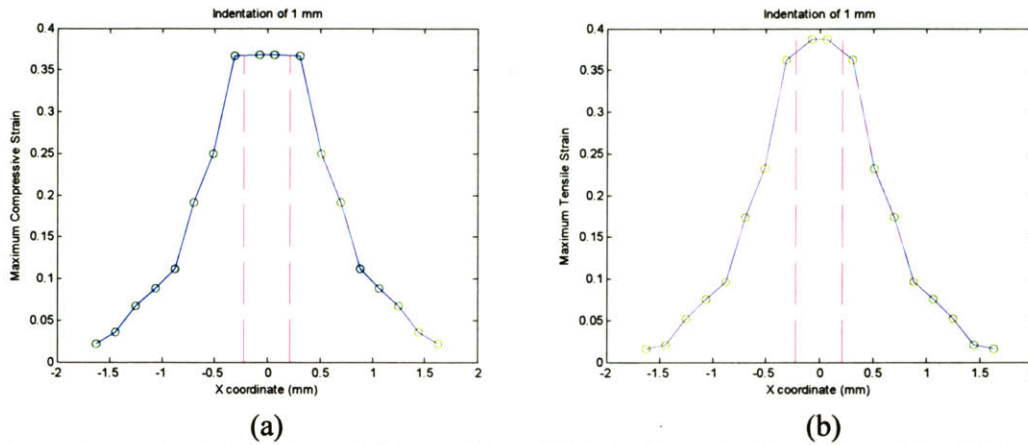

(a)

(b)
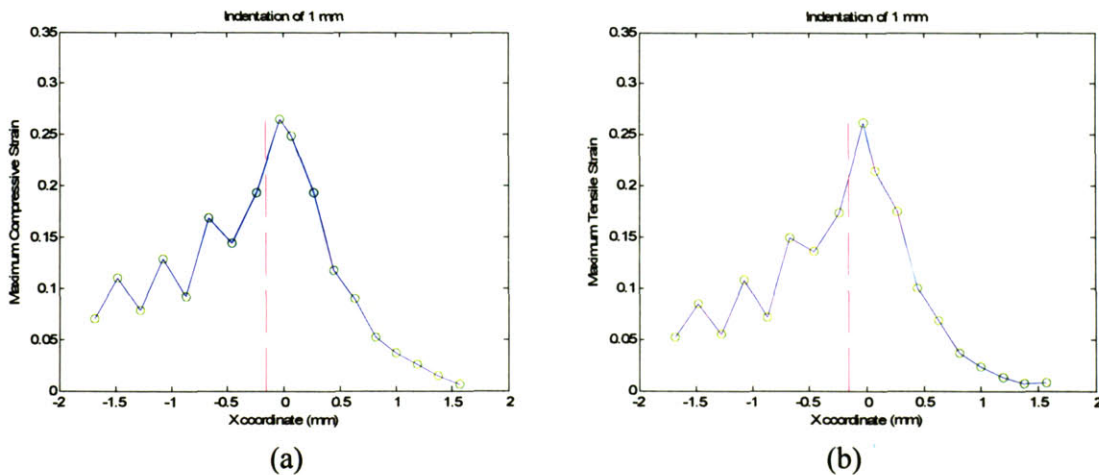
Figure 6-15. The distribution of (a) MCS and (b) MTS at the locations of Meissner's corpuscles along a path on an axial cross section of the finger near the center of the fingerpad when the fingertip model was indented by a step shaped indentor, as shown in Figure 6-11, to a depth of 1 mm. The 18 circles are the data points. The vertical dashed line shows the position of the step, which was originally at the center with an x coordinate of zero and moved a little to the left at this indentation depth.

110

It can be seen from the above plots that when encountering a smooth contact surface, MCS and MTS appear zigzag (Figure 6-7, Figure 6-9, and the right side of the indentor in Figures 6-15). The phenomenon was found to be mainly due to the inner ridges and the outer ridged surface. Figure 6-16 shows the simulation results using a model in which all the epidermal ridges protrude equally into the dermis. Figure 6-16(a) illustrates this model, in which the dark shade represents the epidermis while the light shade represents the dermal area. 6-16(b) and 6-16(c) are the distributions of MCS and MTS, respectively, at the same locations as the simulation results shown in Figure 6-9 when indented by a spherical indentor (R = 7.8 mm) to a maximum of 1 mm. As can been seen, the curve formed by connecting the 18 data points is smoother than the case with the same indentor in Figure 6-9(b).

6-16(d) and 6-16(e) are the distributions of MCS and MTS, respectively, at the same locations as the simulation results shown in Figure 6-15 when indented by a step shaped indentor (shown in Figure 6-13) to a maximum of 1 mm. As can been seen, the curve formed by connecting the 18 data points is smoother than the results in Figure 6-15.

Figure 6-17 shows the simulation from a model without outer ridges (that is, with smooth skin surface) and with all the epidermal ridges protruding equally into the dermis. Figure 6-17(a) illustrates this model in which the dark shade represents the epidermis while the light shade represents the dermal area. In Figure 6-17, (b) and (c) are the distributions of MCS and MTS, respectively, along a path through the same locations as case shown in Figure 6-8 when indented by a spherical indentor (R = 7.8 mm) to a maximum of 1mm. As can been seen, the curve formed by connecting the 18 data points is much smoother than the case with the same indentor in figure 6-9(b) except that at the center of the finger pad, the strain rises. This high strain at the center can be mainly due to the larger indentation at the top of the finger pad. Figure 6-17(d) and 6-17(e) are the distributions of MCS and MTS, respectively, along a path through the same locations as the case shown in Figure 6-15 when indented by a step shaped indentor (shown in Figure 6-13) to a maximum of 1mm. As can been seen, the curve formed by connecting the 18 data points is also much smoother than the results in Figure 6-15.
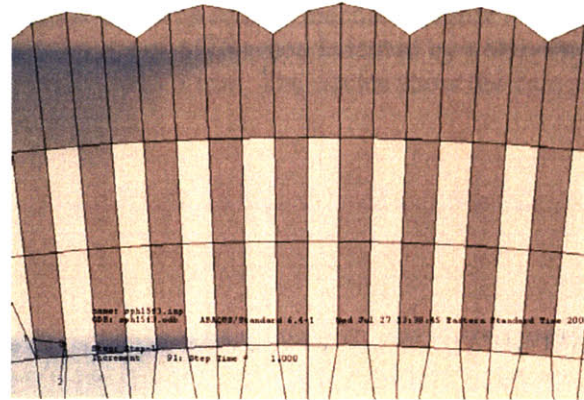
(a)
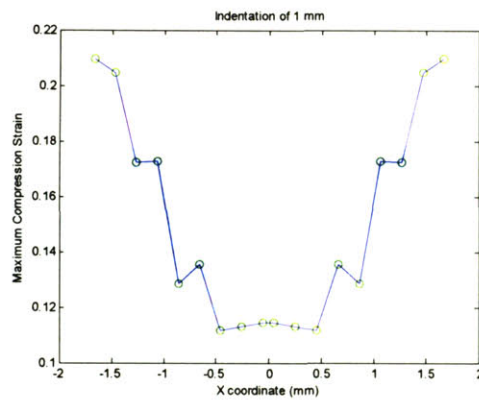
(b)
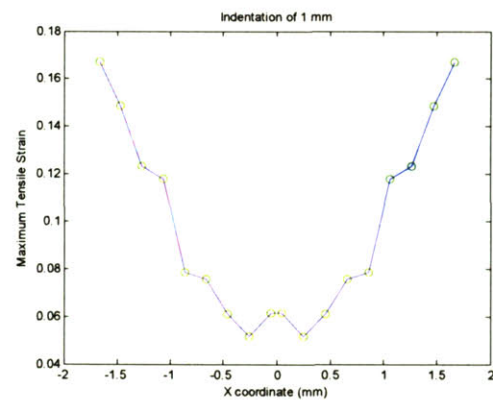
(c)
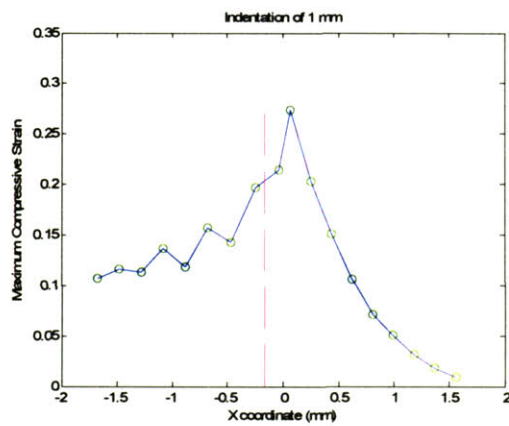
(d)
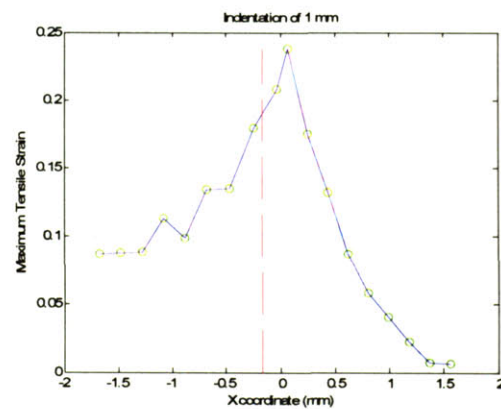
(e)

Figure 6-16. (a) Schematic showing part of a cross section of a fingertip model in which the limiting and intermediate ridges protrude equally into the dermis. (b) The distribution of MCS when indented by a spherical indentor (R = 7.8 mm) to a

112

maximum of 1 mm. (c) The distribution of MTS when indented by a spherical indentor (R = 7.8 mm) to a maximum of 1 mm. (d) The distribution of MCS when indented by a step shaped indentor (Figure 6-11) to a maximum of 1 mm (e) the distribution of MTS when indented by a step shaped indentor (Figure 6-11) to a maximum of 1 mm. The circles show the data points.

(a)

(b)

(c)

(d)

(e)
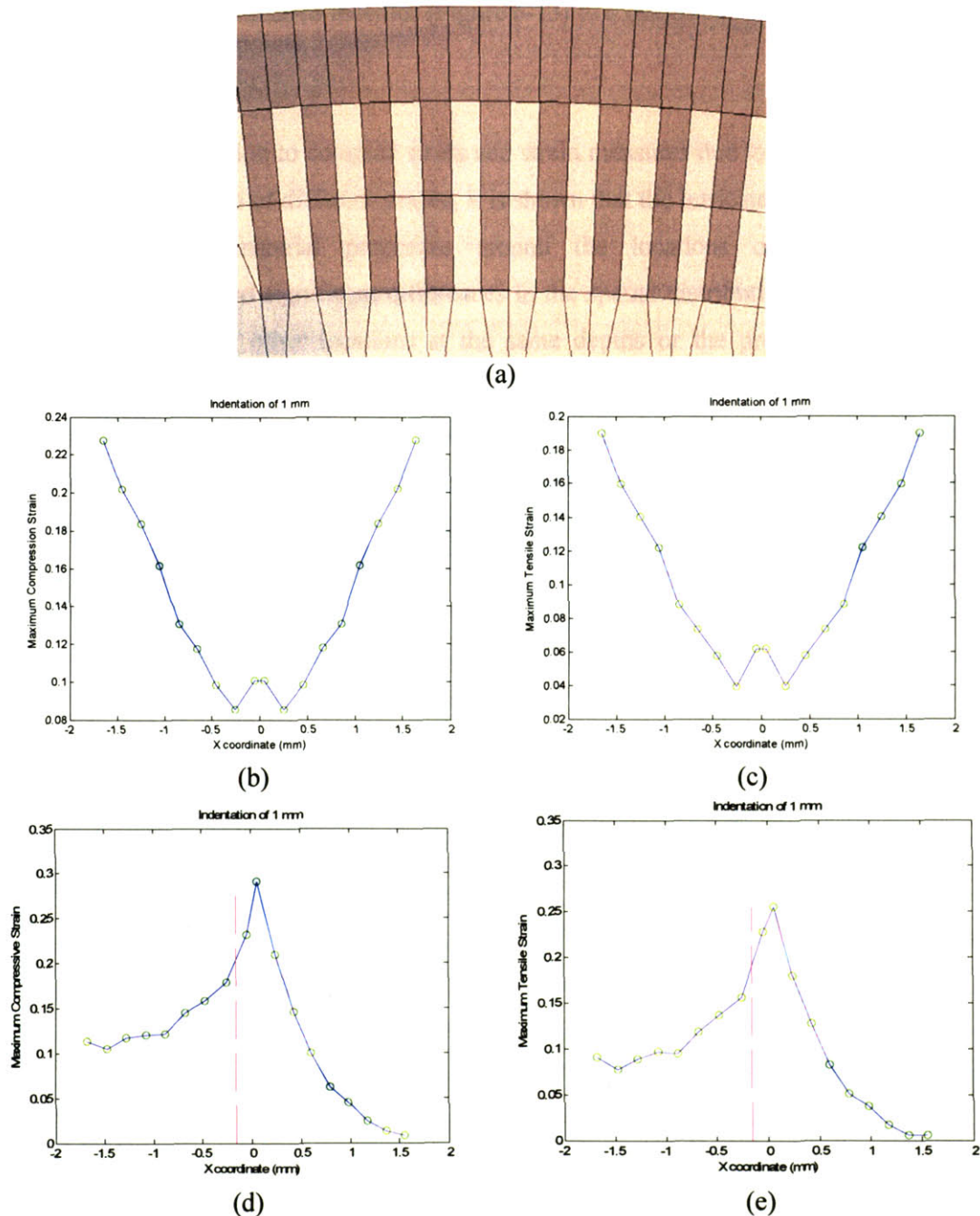
Figure 6-17. (a) Schematic showing part of a cross section of a fingertip model in which skin surface is smooth without ridges and the limiting and intermediate ridges protrude equally into the dermis. (b) The distribution of MCS when indented by a spherical indentor (R = 7.8 mm) to a maximum of 1 mm. (c) The distribution of MTS when indented by a spherical indentor (R = 7.8 mm) to a maximum of 1

114

mm . (d) The distribution of MCS when indented by a step shaped indentor (Figure 6-13) to a maximum of 1 mm (e) the distribution of MTS when indented by a step shaped indentor (Figure 6-13) to a maximum of 1mm. The circles show the data points.

From the above simulation to compute stress and strain measures due to static indentation of the fingertip by rigid objects of different shapes, it is shown that the intricate geometry of skin layers and inhomogeneous material properties around the locations of the SA-I and RA mechanoreceptors caused significant differences in the spatial distribution of candidate relevant stimuli, compared with other locations at the same depths or the predictions from previous homogeneous models of the fingertip. The distribution of the SED at the locations of SA-I mechanoreceptors and the distribution of MCS/MTS at the locations of RA mechanoreceptors under indentation of different object shapes were obtained and can serve as predictions to be tested in future biomechanical and neurophysiological experiments.

Summary and Future Work

7.1 Summary

Based on a previously developed multilayered 3D finite element model of the human fingertip, an improved 3D finite element model of the human fingertip was developed in order to investigate skin mechanics resulting from contact with different shapes of objects. This model incorporated more realistic geometry of the ridged skin both on the surface of the finger pad and the corresponding papillary interface between the epidermis and the dermis, based on *in vivo* OCT images of the human fingertip skin. The ratio of the elastic modulus of the epidermis versus the dermis was estimated from *in vivo* ultrasound strain imaging, in which a previously developed high frequency ultrasound backscatter microscope was combined with a custom designed indentation stage to image the human fingertip before and after load was applied, and the strain within the skin in the direction of the loading was analyzed. With appropriately adjusted ratios and values of the elastic modulus in the multiple layers of the model, predictions of the model matched very well the empirically obtained displaced skin surface recorded in the OCT images and the force response data, thereby validating the biomechanical behavior of the model.

Using this validated fingertip model, finite element simulations were conducted to study the mechanical response of fingertip skin to contact with shaped objects. In the simulations, different shapes were indented into the finger pad skin and the spatial distribution of the contact area, strain energy density (SED), maximum compression strain (MCS), and maximum tensile strain (MTS) were investigated. The model was able to show that the grooves on the ridged skin surface restrain the finger pad from being fully in contact with the objects with smooth surfaces (Figure 6-1). Due to stress concentrations at the ridges, SED is clearly higher at the end of the intermediate ridges (Figure 6-2), which might imply the importance of these locations for the SA-I mechanoreceptors. For spherical indenters, higher curvature causes higher SED value at the locations of the SA-I receptors near the center of the finger pad but it drops faster away from the center due to the smaller contact area (Figure 6-4). The cylindrical indenter, owing to its two different curvatures along its two principal axes, shows significantly different SED distributions in the corresponding two directions. Due to the dermal papillae structure and the nonlinear process of deformation, MCS and MTS are higher at the locations of the RA mechanoreceptors

116

than the other locations at the same depth only in an initial range of indentation (Figure 6-6 and Figure 6-8). Different from SED at the locations of the SA-I mechanoreceptors, the distribution of MCS and MTS at the locations of RA mechanoreceptors can reach higher values away from the finger pad center when indented by flat or smooth convex objects during indentation (Figure 6-6 and Figure 6-8). For spherical indenters, MCS and MTS are also higher for higher curvatures. For the rectangular bar and step shaped indenters, SED, MCS, and MTS all show the highest values around the bar and step, with an asymmetric shape corresponding to the step indenter due to its inherently asymmetric geometry (Figure 6-9, 6-10, 6-12, 6-13 and 6-14). And due to the ridged outer surface and interface between the dermis and epidermis, the distributions of MCS and MTS at the locations of RA mechanoreceptor appear zigzag (Figure 6-15).

7.2. Contributions

Quantitative understanding of the mechanisms underlying the human sense of touch is important from both basic scientific points of view as well as for applications such as robotics, virtual reality, rehabilitation, and development of tactile displays. Given the experimental limitations in directly observing the associated tissue deformations and stresses at sufficient resolution, mechanistic models of the skin and tissues underneath are needed. An ideal model of mechano-transduction has to predict the empirical data in both its mechanical behavior and neural response.

Phillips and Johnson's mechanistic model of skin (1981) based on standard continuum mechanics theory successfully predicted the spatial response of the neural afferent under indentation by edges, bars and gratings and only three parameters (receptor depth, sensitivity, and threshold) in this model were adjusted to give the best fit between model and data profiles without any adjustment on skin parameters. This model is based on the following three assumptions: (1) infinitesimally small deformations; (2) plane strain; (3) the mechanical properties of skin can be approximated by those of a semi-infinite medium that is homogeneous, isotropic and linear-elastic. With these assumptions, any rigid, spatially complex stimulus can be redefined as equivalent load (force) profile that is superposable and would produce the specified displacement profiles in the ideal medium. Further, the assumption of a uniformly distributed identical mechanoreceptors located at a constant depth from the skin surface would imply that

the spatial response profile is the same as population response profile. However, actual skin deformations during touch are not small compared to the size of the fingertip and due to the assumption of plane strain, the model can only be applied to 2D cases (i.e. shapes that do not vary along one of their dimensions, such as a cylinder or a grating). For example, the case with spherical indenter can not be investigated using this model. And even for 2D conditions, it has been shown (Srinivasan and Dandekar, 1996) that the shape of the skin model has profound effect on load distribution on the skin, thus the stress and strain distribution within it, and based on the dimension of the indenter (grating used by Philips and Johnson (1981): 25 mm × 15 mm × 10 mm) compared to the normal size of fingerpad, this simplification to a semi-infinite space can not be justified from a mechanistic perspective.

As for the assumption of homogeneity within the entire skin, it is well known that significant differences exist in the stiffness of epidermis and dermis. Since SA-I and RA mechanoreceptors are both located around this interface between the epidermis and dermis, failing to model this difference in stiffness is again not justified from a mechanistic perspective.

It is also quite questionable if the principle of superposition can be applied because linearity of the system is no longer satisfied due to large deformations that require the use of nonlinear strain-displacement relations and nonlinear contact mechanics that arises whenever an object comes in contact with the skin. And in spite of all the simplifications made compared to realistic skin properties, this model was not verified with any empirical data on skin biomechanical behavior, although a good correlation was shown between the stress/strain calculated from this model and the neural response data.

In the previous neurophysiological research (Phillips and Johnson, 1981; Srinivasan and LaMotte, 1989), the frequency of neural impulses of single nerve fibers to gratings or step shapes indented into the monkey finger pad were recorded for a sequence of indentations by moving the indenter laterally between the indentations such that the monkey fingerpad came in contact with successive spatial locations on the indenter shape. The responses were then plotted as a function of spatial location on the indenter to obtain the "spatial response profile" of the fiber, which has been used as a measure of the population response profile, which is the response from multiple individual receptors for a single indentation. However, due to the curved shape of skin surface and the complex material composition in the finger pad, the spatial response profile is not exactly the same as the population response profile.

The waterbed model developed by Srinivasan (1989) matched well the skin surface deflection data of primate finger pads under line loads, but it failed to correlate the neural response data due to the uniform tension in the membrane and uniform pressure field within the fluid. The subsequent FE model developed by Dandekar and Srinivasan (1997) considered the skin stiffness variation among different layers (epidermis, dermis, fat, and bone) and was validated against the skin surface deformation data under line load, thus was based on more solid biomechanical data. The direct FE simulation under specified indenter geometry is also more natural than defining force profile within an ideal medium. Based on this FE model, the model developed by Raju and Srinivasan (1999) improved its resolution for simulating the contact with objects that have high curvatures such as the edges of bars. The FE models were also verified to be able to predict neural response using the strain energy density as the relevant stimulus. These models can be directly used to simulate any shape of indenters and enable calculation of the stress/strain measures without transforming the indenter geometry into any kind of approximate force profile. They can also take into account variation in the human finger size, for example, by inserting a proportional constant into the geometry of the model. However all these models did not take into account the effect of ridges and grooves in the fingerpad skin.

In this thesis, a more sophisticated model was developed which incorporated the ridged skin surface and the papillary interface between the epidermis and dermis and considered the *in vivo* stiffness variation between the epidermis and dermis, where two important mechanoreceptors (SAI and RA) are located. Since most of the available skin material data in the literature are from tension tests on excised specimens, the properties of which are known to be different from that of *in vivo* tissues due to the loss of natural tension, absence of blood flow, and specimen preparation effects, in this thesis, *in vivo* experiments were conducted to examine the stiffness ratio between the epidermis and dermis. Different from the previous fingertip models, the one described in this thesis considers the discrete distribution of the mechanoreceptors, which is more realistic, and the effect of the papillary interface between the epidermis and dermis was found to cause stress concentrations, implying the special characteristic of the locations of RA and SA-I mechanoreceptors. Unfortunately, due to the high computational complexity and consequently the computational time needed for the improved model developed as a part of this thesis, simulated spatial response profiles for each of the shaped stimuli considered here could not be obtained. As mentioned before, primarily due to the curvature and finiteness of the fingertip, the

spatial response profile is not exactly the same as the simulated population response obtained here. Nevertheless, the spatial distribution of strain energy density of this model at the locations of the SAI mechanoreceptors qualitatively correlates with the general trend of the spatial response profile from the data recorded for SAI receptors when a fingertip was indented by spherical indenter (Goodwin et. al., 1995), 3mm bar (Phillips and Johnson, 1981), and steps (Srinivasan and LaMotte, 1987). However, to determine if the improved mechanistic model leads to better correlation between the simulated responses and empirically obtained neuronal data than that obtained from previous models, spatial response profiles for each candidate relevant stimulus for each of the shaped stimuli indenting the fingerpad needs to be obtained. At present, this effort seems to be too computationally intensive in relation to the computational resources available.

Alternatively, to more directly determine the relationship between the relevant stimulus in terms of stresses/strains that trigger response from a particular mechanoreceptor and the corresponding neural data, experiments should be done on humans with simultaneous recording of multiple nerve fibers, so that a true population response profile can be obtained by plotting the neural response as a function of the absolute lateral position on the fingertip surface and a measure of the linear or nonlinear relationship between the stress/strain value and the neural data can be calculated for a number of receptors. A more complete experiment should also include psychophysical experiments to relate the human detection of object shapes to the population response. Then using this model, one can easily define different 3D shapes of indenters and the finite element calculation will do the rest to figure out the force response of the skin and thus the strain and stress distribution within the skin. And with the known quantitative relationship between the stress/strain within the skin and the mechanoreceptor response, population response can be predicted, thus relating neural response to the perception of object shapes.

7.3 Future Work

Since the ultrasound strain imaging described in chapter 4 was in its initial stage of development at the Touch Lab and the purpose was merely to get an estimate of the stiffness ratio between the epidermis and the dermis to be incorporated into the finite element model, the device and experimental procedure were kept simple and at low cost. There is a need for improvement in several aspects to achieve a strain imaging system with better performance. For example, one

difficulty that has been encountered that is inherent to *in vivo* experiments is to keep the subject's finger stationary with respect to the ultrasound transducer during the indentation when the finger was moved up by the stage, which often caused serious decorrelation of the data. Hence a better fixture or different experimental procedure (e.g. perhaps the application of local anesthesia) is needed in this experiment. To perform dynamic experiments, PC controlled motorized indentation stage should be built to be able to control the indentation precisely without manual intervention. Besides, the procedure assumed the skin as a semi-infinite layered structure and only considered a single spot on the finger pad to investigate its axial strain along the depth within the skin. For more realism, or to expand the range of skin surface under investigation, a two-dimensional strain map is needed to be developed, that is, multiple A-lines at different lateral locations need to be recorded for deformation and strain analysis. As mentioned earlier, one concern is the unwanted movement of the finger due to the extended time taken by the experimental procedure, which implies that better fixtures should be designed to improve the steadiness of the finger during the imaging procedure. Another concern is the potential motion error of the transducer when it scans over the skin, which can also cause decorrelation. Possible solutions are to change to a motion control loop with higher precision, or collect data from a large number of A-lines along a given lateral range, and then several A-lines around the possible corresponding one in the post-compression data are considered in the cross-correlation calculation to find the best match with a given A-line in the pre-compression data.

Although skin exhibits viscous properties such as rate-dependent stress-strain relations and hysteresis, after a few cycles of loading it settles down to a steady state response and is therefore termed "pseudoelastic" (Fung, 1981). In our experiments, the OCT images were taken after the transients settled down, thus satisfying "pseudostatic" behavior. The mechanistic problems to simulate the pseudostatic loading are, hence, static in nature. It is thus not necessary to model the viscosity of the finger pad. The future model could consider the incorporation of viscoelastic properties for simulations of dynamic loads and real time imaging is necessary to obtain the corresponding data for validation.

If high performance computing facility becomes available, higher resolution finite element model could be developed, so some effects due to the low resolution at the fine structures can be avoided. It was found (Cauna, 1954) that the stratum corneum of the hairless digital epidermis is made of two types of keratin. The harder keratin of the grooves provides a supporting framework

or skeleton for the epidermis and the softer and plastic keratin of the projecting ridges covers the underlying touch receptors (RA). In the model derived in this thesis, this possible difference in stiffness within the stratum corneum was not considered. It can possibly be considered in the future.

While the finite element simulation can calculate the contact pressure distribution across the finger pad, it would be very beneficial to have a device able to measure directly the pressure distribution during touch. The technology for building such a device is potentially in the fields of microelectromechanical systems (MEMS) or even nanotechnology. When such a device is developed, the results from the finite element simulation could be validated with experimental measurement of contact pressure distribution within the areas of contact with shaped objects.

References

Alam S. K., Ophir, J., and Konofagou, E. E., "An adaptive strain estimator for elastography," *IEEE Trans. Ultra. Ferro. Freq. Contr.*, 45(2), pp. 461-472, 1998.

Bertrand, M., Meunier, J., Doucet, M., and Ferland, G.., "Ultrasonic biomechanical strain gauge based on speckle tracking," *IEEE Ultrason. Symp.*, pp. 859-863, 1989.

Bohs, L. N., and Trahey, G. E., "A novel method for angle independent ultrasonic imaging of blood flow and tissue motion," *IEEE Trans. Biomedical Engineering*, Vol. 38, 3, 280-286, 1991.

Bracewell, R., *The Fourier transform and its applications*, McGraw Hill, 2000.

Cantrell, J. H., Goans, R. E., and Roswell, R. L., "Acoustic impedance variations at burn-nonburn interfaces in porcine skin," *Journal of the Acoustical Society of America*, vol. 64, pp. 731-735, 1978.

Cauna, N., "Nature and functions of the papillary ridges of the digital skin," *Anat. Rec*, vol. 119, pp. 449-468, 1954.

Cysyk, J. P. and Srinivasan, M. A., "Skin dynamics in the tactile sensing of shape," Touch Lab Report, *RLE Technical Report* - , MIT, 1999.

Dandekar, K. and Srinivasan, M.A., "The role of mechanics in tactile sensing of shape," Touch Lab Report 2, *RLE Technical Report* No. 604, MIT, 1997.

Dandekar, K, Raju, B. I., and Srinivasan, M. A., "3-D finite-element models of human and monkey fingertips to investigate the mechanics of tactile sense," *Journal of Biomechanical Engineering*, Vol. 125, pp. 682-691, ASME Press, 2003.

Darian-Smith, I., "The sense of touch: performance and peripheral neural processes," *Handbook of Physiology – The nervous system – III*, pp. 739-788, 1984.

de Boer, J. F., Milner, T. E., van Gemert, M. J. C., and Nelson, J. S., "Two-dimensional birefringence imaging in biological tissue by polarization-sensitive optical coherence tomography," *Optical Letters*, Vol. 22, No. 12, pp. 934-936, 1997.

Doyley, M. M., Meaney, P. M., and Bamber, J. C., "Evaluation of an iterative reconstruction method for quantitative elastography," *Phys. Med. Biol.* 45, pp. 1521-1540, 2000.

Drexler W., Morgner, U., Kartner, F. X., Pitris, C., Boppart, S. A., Li, X. D., Ippen, E. P., and Fujimoto, J. G., "*In vivo* ultrahigh-resolution optical coherence tomography," *Optics Letters*, Vol. 24, No. 17, 1221-1223, 1999.

de Rigal, J., Escoffier, C., Querleux, B., Faivre, B., Agache, P., and Leveque, J.-L., "Assessment of aging of the human skin by *in vivo* ultrasonic imaging," *Journal of Investigative Dermatology*, vol. 93, pp. 621-625, 1989.

Edwards, C., Al-Aboosi, M. M., and Marks, R., "The use of A-scan ultrasound in the assessment of small skin tumours," *British Journal of Dermatology*, vol. 121, pp. 297-304, 1989.

El Gammal, S., El Gammal, C., Kasper, K., Pieck, C., Altmeyer, P., Vogt, M., and Ermert, H., "Sonography of the skin at 1000 MHz enables in vivo visualization of stratum corneum and viable epidermis in palmar skin and psoriatic plaques," *Journal of Investigative Dermatology*, vol. 113, pp. 821-829, 1999.

Fornage, B. D., McGavran, M. H., Duvic, M., and Waldron, C. A., "Imaging of the skin with 20-MHz US," *Radiology*, vol. 189, pp. 69-76, 1993.

Fortin M., Buschmann, M. D., Bertrand, M. J., Foster, F. S., and Ophir, J., "Cross-correlation of ultrasound A-lines to obtain dynamic displacement profiles within poroelastic materials undergoing stress-relaxation," *Proceedings of SPIE 3982*, pp. 286-294, 2000.

Fortin, M., Buschmann, M. D., Bertrand, M. J., Foster, F. S., and Ophir, J., "Dynamic measurement of internal solid displacement in articular cartilage using ultrasound backscatter," *Journal of Biomechanics* 36, pp. 443-447, 2003.

Foster, F. S., Lockwood, G. R., Ryan, L. K., Harasiewicz, K. A., Berube, L., and Rauth, A. M., "Principles and applications of ultrasound backscatter microscopy," *IEEE Transactions on Ultrasonics, Ferroelectrics, and Frequency Control*, vol. 40, pp. 608-617, 1993.

Freeman, A. W. and Johnson, K. O., "Cutaneous mechanoreceptors in macaque monkey: Temporal discharge patterns evoked by vibration, and a receptor model," *Journal of Physiology*, vol.323, pp. 21-41, 1982a.

Fruhstorfer, H., Abel, U., Garthe, C.-D., Knuttel, A., "Thickness of the stratum corneum of the volar fingertips," *Clinical Anatomy*, 13, pp. 429-433, 2000.

Fujimoto, J. G., Drexler, W., Morgner, U., Kartner, F., and Ippen, E., "Optical coherence tomography: high resolution imaging using echoes of light," *Optics & Photonics News*, pp. 24-31, 2004.

Fung, Y. C., *Biomechanics*, Springer, New York, 1981.

Gibson, T. and Kenedi, R. M., "The structural components of the dermis and their mechanical characteristics," in the Dermis. Advances in Biology of Skin (Montagna, W., Bentley, J. P., and Dobson, R. L., eds.), vol. 10, pp. 19-38, *Proc. Symp. on Biology of Skin*, 1968.

Gniadecka, M., and Jemec, G. B. E., "Quantitative evaluation of chronological ageing and photoageing *in vivo*: studies on skin echogenicity and thickness," *British Journal of Dermatology*, vol. 139, pp. 815-821, 1998.

Goodwin, A. W., John, K. T., and Marceglia, A. H., "Tactile discrimination of curvature by humans using only cutaneous information from the fingerpads," *Experimental Brain Research*, vol. 86, pp. 663-672, 1991.

Goodwin, A. W., Browning, a. S., and Wheat, H. E., "Representation of curved surfaces in responses of mechanoreceptive afferent fibers innervating the monkey's fingerpad," *Journal of Neuroscience*, vol. 15, no. 1, pp. 798-810, 1995.

Goodwin, A. W. and Morley, J. W., "Sinusoidal movement of a grating across the monkey's fingerpad: Representation of grating and movement features in afferent fiber responses," *Journal of Neuroscience*, vol. 7, no. 7, pp. 2168-2180, 1987a.

Goodwin, A. W. and Morley, J. W., "Sinusoidal movement of a grating across the monkey's fingerpad: Temporal patterns of afferent fiber responses," *Journal of Neuroscience*, vol. 7, no. 7, pp. 2181-2191, 1987b.

Goodwin, A. W. and Wheat, H. E., "Human tactile discrimination of curvature when contact area with the skin remains constant," *Experimental Brain Research*, vol. 88, pp. 447-450, 1992.

Gottlober, P., Kerscher, M. J., Korting, H. C., and Peter, R. U., "Sonographic determination of cutaneous and subcutaneous fibrosis after accidental exposure to ionising radiation in the course of the Chernobyl nuclear power plant accident," *Ultrasound in Medicine and Biology*, vol. 23, pp. 9-13, 1997.

Gulati, R. J. and Srinivasan, M. A., "Human fingerpad under indentation I: Static and dynamic force response," *ASMA Summer Annual Meeting*, 1995.

Gupta A. K., Turnbull, D. H., Harasiewicz, K. A., Shun, D. T., Watteel, G. N., Foster, F. S., and Sauder, D. N., "The use of high-frequency ultrasound as a method of assessing the severity of a plaque of psoriasis," *Archives of Dermatology*, vol. 132, pp. 658-662, 1996.

Harland, C. C., Bamber, J. C., Gusterson, B. A., and Mortimer, P. S., "High frequency, high resolution B-scan ultrasound in the assessment of skin tumours," *British Journal of Dermatology*, vol. 128, pp. 525-532, 1993.

Ho, C., and Srinivasan, M. A., "Human haptic discrimination of thickness," Touch Lab Report 6, *RLE Technical Report* - 608, MIT, 1996.

Hoffmann, K., Jung, J., El Gammal, S., and Altmeyer, P., "Malignant melanoma in 20 MHz Bscan sonography," *Dermatology*, vol. 185, pp. 49-55, 1992.

Huang, D., Swanson, E. A., Lin C. P., Schuman, J. S., Stinson, W. G., Chang, W., Hee, M. R., Flotte, T., Gregory, K., Puliafito, C. A., and Fujimoto, J. G., "Optical Coherence Tomography," *Science*, vol. 254, pp. 1178-1181, 1991.

Ihn, H., Shimozuma, M., Fujimoto, M., Sato, S., Kikuchi, K., Igarashi, A., Soma, Y., Tamaki, K., and Takehara, K., "Ultrasound measurement of skin thickness in systemic sclerosis," *British Journal of Rheumatology*, vol. 34, pp. 535-538, 1995.

John, K. T., Goodwin, A. W., and Darian-smith, I., "Tactile discrimination of thickness," *Experimental Brain Research*, vol. 78, no. 1, pp. 62-68, 1989.

Kallel, F. and Bertrand, M., "Tissue elasticity reconstruction using linear perturbation method," *IEEE Trans. Med. Imag,*, 15(3), pp. 299-313, 1996.

Konofagou, E. E., Varghese, T., Ophir, J., and Alam, S. K., "Power spectral strain estimator in elastography," *Ultrasound Med. Biol.* 25, 1115-1129, 1999.

Knuttel A. and Boehlau-Godau, "Spatially confined and temporally resolved refractive index and scattering evaluation in human skin performed with optical coherence tomography," *Journal of Biomedical Optics*, Vol. 5, No. 1, 2000.

Lamb, G. D., "Tactile discrimination of textured surfaces: Psychophysical performance measurements in humans," *Journal of Physiology* (London), vol. 338, pp. 551-565, 1983.

LaMotte, R. H. and Srinivasan, M. A., "Responses of cutaneous mechanoreceptors to the shape of objects applied to the primate fingerpad", *Acta Psychologica*, vol. 84, pp. 41-51, 1993.

LaMotte, R. H. and Srinivasan, M. A., "Neural encoding of shape: Response of cutaneous mechanoreceptors to a wavy surface stroked across the monkey fingerpad," *Journal of Neurophysiology*, vol. 76, no. 6, pp. 3787-3797, 1996.

Lanir, Y., "Skin mechanics," in *Handbook of Bioengineering*, ch. 11, pp. 11.1-11.25, McGraw-Hill, 1987.

Lanir, Y., Dikstein, S., Hartzshtark, A., and Manny, V., "*In vivo* indentation of human skin," *Journal of Biomechanics*, vol. 112, pp. 63-69, 1990.

Lederman, S. J. and Taylor, M. M., "Fingertip force, surface geometry, and the perception of roughness by active touch," *Perception & Psychophysics*, vol. 12, pp. 401-408, 1972.

Leeman, S., Ferrari, L., Jones, J. P., and Fink, M., "Perspective on attenuation estimation from pulse-echo signals," *IEEE Transactions on Sonics and Ultrasonics*, vol. 31, pp. 352-360, 1980.

Levy, J., Gassmuller, J., Schroder, G., Audring, H., and Sonnichsen, N., "Comparison of the effects of calcipotrol, predicarbate, and clobetasol 17-propioate on normal skin assessed by ultrasound measurement of skin thickness," *Skin Pharmacology*, vol. 7, pp. 231-236, 1994.

Liao, J. C. and Srinivasan, M. A., "Experimental investigation of frictional properties of the human finger pad," Touch Lab Report 11, *RLE Technical Report* - 629, MIT, 1999.

126

Lockhart, R. D., Hamilton, G. F., and Fyfe, F. W., "The Skin," *Anatomy of the Human Body*, J P Lippincott Co., Philadelphia, pp. 3-6, 1965.

Loomis, J. M., "An investigation of tactile hyperacuity," *Sensory Processes*, vol. 3, pp. 289-302, 1979.

Maeno, Takashi, Kobayashi, Kazumi, and Yamazaki, Nobutoshi, "Relationship between the structure of human finger tissue and the location of tactile receptors," *JSME International Journal*, vol. 41, no. 1, pp. 94-100, 1998.

Miga, M. I., "A new approach to elastography using mutual information and finite elements," *Physics in Med. & Biol.*, 48, pp. 467-480, 2003.

Moran, C. M., Bush, N. L., and Bamber, J. C., "Ultrasonic propagation properties of excised human skin," *Ultrasound in Medicine and Biology*, vol. 21, pp. 1177-1190, 1995.

Morgner, U., Drexler, W., Krtner, F. X., Li, X. D., Pitris, C., Ippen, E. P., Fujimoto, J. G., "Spectroscopic optical coherence tomography," *Optics Letters*, Vol. 25, no. 2, 111-113, 2000.

O'Donnell, M., Skovoroda, A. R., and Shapo, B. M., "Measurement of arterial wall motion using Fourier based speckle tracking algorithms," *IEEE Ultras. Symp.*, pp. 1101-1104, 1991.

Ophir, J., Cespedes, I., Ponnekanti, H., Yazdi, Y., and Zi, Z., "Elastography: a quantitative method for imaging the elasticity of biological tissues," *Ultrasound Imaging*, vol. 13, pp. 111-134, 1991.

O'Rahilly, R., "Skin, hair, and nail," in *Anatomy: A Regional Study of the Human Structure* (Gardner, E. and O'Rahilly, D. G. R., eds.), w. B. Saunders and Co., 1969.

Pagnoni A., Knuttel, A., Welker, P., Rist, M., Stoudemayer, T., Kolbe, L., Sadiq, I., and Kligman, A. M., "Optical coherence tomography in dermatology," *Skin Research and Technology*, 5, pp. 83-87, 1999.

Pan, Y., Lankenau, E., Welzel, J., Bimgruber, R., and Engelhardt, R., "Optical coherence-gated imaging of biological tissues," *IEEE Journal of Selected Topics in Quantum Electronics*, Vol. 2, No. 4, 1029-1034, 1996.

Park, B. H., Pierce, M. D., Cense, B., and de Boer, J. F., "Real-time multi-functional optical coherence tomography," *Optics Express*, vol.11, No. 7, 782-793, 2003.

Passmann, C. and Ermert, H., "A 100-MHz ultrasound imaging system for dermatologic and ophthalmologic diagnostics," *IEEE Transactions on Ultrasonics, Ferroelectrics, and Frequency Control*, vol. 43, pp. 545-552, 1996.

Phillips, J. R. and Johnson, K. O., "Tactile spatial resolution - II. Neural representation of bars, edges, and gratings in monkey afferents," *J. Neurophysiol.*, vol. 46, no. 6, pp. 1192-1203, 1981a.

Phillips, J. R. and Johnson, K. O., "Tactile spatial resolution - III. A continuum mechanics model of skin predicting mechanoreceptor responses to bars, edges and gratings," *J. Neurophysiol.*, vol. 46, no. 6, pp. 1204-1225, 1981b.

Pierce, M. D., Park, B. H., Cense, B., and de Boer, J. F., "Simultaneous intensity, birefringence, and flow measurements with high-speed fiber-based optical coherence tomography," *Optics Letters*, Vol. 27, No. 17, 1534-1536, 2002.

Povazay, B., "Visible light optical coherence tomography," *SPIE 4619*, pp. 90-94, 2002.

Quiiliam, T. A., "The structure of fingertip skin," in *Active touch - The mechanism of Recognition of Objects by Manipulation: A Multidisciplinary Approach* (Gordon, G., ed.), Oxford: Pergamaon, 1978.

Raghavan K. R. and Yagle A. E., "Forward and inverse problems in elasticity imaging of soft tissues," *IEEE Trans. Nuclear Science*, 41(4), pp. 1639-1648, 1994.

Raghetti, R., Ophir, J., and Ktonas, P., "Axial resolution in elastography," *Ultrasound in Med. & Biol.*, 28(1), pp. 101-113, 2002.

Rajadhyaksha, M., Grossman, M., Esteroxitz, R., Webb R. H., and Anderson, R. R., "*In vivo* confocal scanning laser microscopy of human skin: melanin provides strong contrast," *Journal of Investigative Dermatology*, vol. 104, pp. 946-952, 1995.

Rajadhyaksha, M., S. Gonzalez, S., Zavislan, J. M., Anderson, R. R., and Webb, R. H., "*In vivo* confocal scanning laser microscopy of human skin II: Advances in instrumentation and comparison with histology," *Journal of Investigative Dermatology*", vol. 113, pp.293-303, 1999.

Raju B. I. and Srinivasan, M. A., "Encoding and Decoding of Shape in Tactile Sensing," Touch Lab Report, *RLE Technical Report No. 630*, 1999a.

Raju, B. I. and Srinivasan, M. A., "Ultrasound Backscatter Microscope for *in vivo* Imaging of Human Fingertip," Touch Lab Report, *RLE Technical Report No. 631*, 1999b.

Raju, B. I. and Srinivasan, M.A., "High frequency ultrasonic attenuation and backscatter coefficients of in vivo normal human dermis and subcutaneous fat," *Ultrasound in Medicine and Biology*, vol. 27, pp. 1543-1556, 2001.

Raju, B. I. and Srinivasan, M. A., "Statistics of envelope of high-frequency ultrasonic backscatter from human skin *in vivo*," *IEEE Trans. Ultra. Ferr. Freq. Contr.* 49(7), 2002.

Raju, B. I. and Srinivasan, M. A., "High frequency ultrasonic characterization of human skin *in vivo*," Touch Lab Report, *RLE Technical Report*, MIT 2003.

Raju, B. I., Swindells, K. J., Gonzalez, S., and Srinivasan, M. A., "Quantitative ultrasonic methods for characterization of skin lesions *in vivo*," *Ultrasound in Med. & Biol.*, 29(6), 825-838, 2003.

Rollins, A. M., Kulkarni, M. D., Yazdanfar, S., Ung-arunyawee, R., and Izatt, J. A., "*In vivo* video rate optical coherence tomography," *Optics Express*, Vol.3, No.6, pp. 219-229, 1998.

Saxer, C. E., de Boer, J. F., Park, B. H., Zhao, Y., Chen, Z., and Nelson, J. S., "High-speed fiber-based polarization-sensitive optical coherence tomography of *in vivo* human skin," *Optics Letters*, Vol. 25, No. 18, 1355-1357, 2000.

Schmitt J. M., Knuttel, A., Yadlowsky, M., and Eckhaus, M. A., "Optical-coherence tomography of a dense tissue: statistics of attenuation and backscattering," *Phys. Med. Biol.* 39, pp. 1705-1720, 1994.

Schimitt J. M., "OCT elastography: imaging microscopic deformation and strain of tissue," *Optics Express*, vol. 3, No. 6, 1998.

Schimitt J. M., Bao, X., and Xiao, S., "Micro-electography of tissue with OCT," *SPIE* vol. 3598, pp. 47-55, 1999.

Seidenari, S. and Belletti, B., "The quantification of patch test responses: A comparison between echographic and calorimetric methods," Acta *Dermato-Venereaologica*, vol. 78, pp. 364-366, 1998.

Skovoroda, A. R., Emelianov, S. Y., and O'Donnell, M., "Tissue elasticity reconstruction based on ultrasonic displacement and strain images," *IEEE Trans. Ultra. Ferr. Freq. Contr.*, 42(4), 1995.

Soualmi, L., Bertrand M., Mongrain, R., and Tardif J.-C., "Forward and inverse problem in endovascular elastography," *Acoustical Imaging*, 23, pp. 203-209, 1997.

Srinivasan, M. A., "Surface deflection of primate fingertip under line load," *J. Biomechanics*, vol. 22, no.4, pp. 343-349, 1989.

Srinivasan, M. A., "Haptic interfaces," *Virtual Reality, Scientific and Technological Challenges* (Durlach, N. I. and Mavor, A. S., eds.), National Academy Press, Washington, D.C., 1994.

Srinivasan, M. A. and LaMotte, R. H., "Tactile discrimination of shape: Responses of slowly adapting mechanoreceptive afferents to a step stroked across the monkey fingerpad," *Journal of Neuroscience*, vol. 7, no. 6, pp. 1655-1671, 1987a.

Srinivasan, M. A. and LaMotte, R. H., "Tactile discrimination of shape: Responses of rapidly adapting mechanoreceptive afferents to a step stroked across the monkey fingerpad," *Journal of Neuroscience*, vol. 7, no. 6, pp.1672-1681,1987b.

Srinivasan, M. A. and LaMotte, R. H., "Tactile discrimination of shape: Responses of slowly and rapidly adapting mechanoreceptive afferents to a step indented into the monkey fingerpad," *Journal of Neuroscience*, vol. 7, no.6, pp. 1682-1697, 1987c.

Srinivasan, M. A. and LaMotte, R. H., "Tactile discrimination of softness," *J. Neurophsiol.*, vol. 73, no. 1, pp. 88-101, 1995.

Srinivasan, M. A., and Dandekar, K., "An investigation of the mechanics of tactile sense using two-dimensional models of the primate fingertip," *Journal of Biomechanical Engineering*, vol. 118, 48-55, 1996.

Srinivasan, M. A., Whitehouse, J. M., and LaMotte, R. H., "Tactile detection of slip: Surface microgeometry and peripheral neural codes," *Journal of Neurophysiology*, vol. 63, no. 6, pp. 1323-1332, 1990.

Sumi, C., Suzuki, A., and Nakayama, K., "Estimation of shear modulus distribution in soft tissue from strain distribution," *IEEE Trans. Biomed. Eng.*, 42(2), 1995.

Tearney, G. J., Brezinski, M. E., Southern, J. F., Bouma, B. E., Hee, M. R., and Fujimoto, J. G., "Determination of the refractive index of highly scattering human tissue by optical coherence tomography," *Optics Letters*, vol. 20, no. 21, 2258-2260, 1995.

Tearney, G. J., Bouma, B. E., Boppart, S. A., Golubovic, B., Swanson, E. A., and Fujimoto, J. G., "Rapid acquisition of *in vivo* biological images by use of optical coherence tomography," *Optics Letters*, Vol. 21, No. 17, pp. 1408-1410, 1996.

Turnbull, D. H., Starkoski, B. G., Harasiewicz, K. A., Semple, J., From, L., Gupta, A. K., Sauder, D. N., and Foster, F. S., "A 40-100 B-scan ultrasound backscatter microscope for skin imaging," *Ultrasound in Medicine and Biology*, vol. 21, pp. 79-88, 1995.

Vabre L., Dubois, A., and Boccara, A. C., "Thermal-light full-field optical coherence tomography," *Optics Letters*, Vol. 27, No. 7, pp. 530-532, 2002.

Vaillant, L., Berson, M., Machet, L., Callens, A., Pourcelot, L., and Lorette, G., "Ultrasound imaging of psoriatic skin: A noninvasive technique to evaluate treatment of psoriasis," *International Journal of Dermatology*, vol. 33, pp. 786-790, 1994.

Van Doren, C. L., "Measurement and modeling of spatiotemporal tactile sensitivity," *PhD Thesis*, Syracuse University, 1987.

Varghese, T. and Ophir, J., "Performance optimization in elastography: multi-compression with temporal stretching," *Ultrasonic Imaging* 18, pp. 193-214, 1996.

Varghese T., Ophir, J., and Cespedes, I., "Noise reduction in elastograms using temporal stretching with multi-compression averaging," *Ultrasound in Med. & Biol.*, 22(8), pp. 1043-1052, 1996.

Varghese T. and Ophir J., "A theoretical framework for performance characterization of elastography: the strain filter," *IEEE Trans. Ultra. Ferr. Freq. Contr.*, 44(1), pp. 164-172, 1997.

Varghese T., "Enhancement of echo-signal correlation in elastography using temporal stretching," *IEEE Trans. Ultra. Ferr. Freq. Contr.*, 44(1), pp. 173-180, 1997.

Vogt, M., Scharenberg, R., Hoffmann, K., Altmeyer, P., and Ermert, H., "*In vivo* evaluation and imaging of skin elasticity applying high frequency (22 MHz) ultrasound," *IEEE Ultrasonics Symposium*, pp. 1863-1866, 2002.

Wan, S., Raju, B. I., and Srinivasan, M. A., "Robust deconvolution of high-frequency ultrasound images using higher order spectral analysis and wavelets," *IEEE Trans. Ultra. Ferroelec. Freq.Contr.*, 2003.

Zhao, Y., Chen, Z., Ding, Z., Ren, H., and Nelson, J. S., "Real-time phase-resolved functional optical coherence tomography by use of optical Hilbert transformation," *Optics Letters*, Vol. 27, No. 2, pp. 98-100, 2002.

Zhou L. and Srinivasan, M.A., "3D finite element model of human fingertip," unpublished data and simulation results, 2002.